UNIVERSITÀ DEGLI STUDI DI PADOVA

DOTTORATO DI RICERCA IN:
INGEGNERIA DELL'INFORMAZIONE

CICLO XX

Generation, characterization and applications of optical entangled states

Coordinatore: Ch.mo Prof. Silvano Pupolin
Supervisore: Prof. Paolo Villoresi
Correlatore: Prof. Alexander V. Sergienko

Dottorando: Cristian Bonato

31 gennaio 2008

UNIVERSITÀ DI PADOVA  FACOLTÀ DI INGEGNERIA

Generation, charaterization and applications of optical entangled states

borsa a tema vincolato CARIPARO
"Ottica per la Comunicazione Quantistica"

Ph.D. THESIS

Author: Cristian Bonato

Coordinator: Ch.mo Prof. Silvano Pupolin
Supervisor: Prof. Paolo Villoresi
Co-Supervisor: Prof. Alexander V. Sergienko (Boston University)

31 gennaio 2008

DEPARTMENT OF INFORMATION ENGINEERING
UNIVERSITY OF PADOVA

CORSO DI DOTTORATO IN
INGEGNERIA ELETTRONICA E DELLE
TELECOMUNICAZIONI – XX CICLO

Contents

Sommario

Questo lavoro di tesi é incentrato sullo studio di stati entangled multiparametrici generati per mezzo della fluorescenza parametrica (o *spontaneous parametric downconversion*, SPDC), un processo ottico nonlineare in cui un fotone di pompa si annichila generando due fotoni con caratteristiche spettrali, spaziali e di polarizzazione peculiari. Tali stati sono stati utilizzati negli ultimi vent'anni in esperimenti sui fondamenti della meccanica quantistica o in applicazioni nel settore della Quantum Information, come la crittografia quantistica, il teletrasporto quantistico o la computazione quantistica.
La prima sezione di questa tesi riguarda la manipolazione delle proprietá spaziali dei fotoni generati mediante SPDC per mezzo di uno specchio deformabile, e l'influenza di tali manipolazioni sull'interferogramma quantistico risolto in tempo. Questo é importante dal punto di vista scientifico in quanto strumento per creare stati quantistici ad hoc, e per dimostrare un effetto analogo alla cancellazione della dispersione, nel dominio dei vettori d'onda.
La seconda sezione riguarda la caratterizzazione di stati ottici entangled in frequenza e polarizzazione: introduciamo il concetto di matrice di coerenza spettrale per coppie di fotoni come estensione della matrice di coerenza spettrale classica, suggerendo una tecnica sperimentale per misurare tale quantitá. Questo concetto é importante per caratterizzare le proprietá di polarizzazione di stati entangled non monocromatici, in applicazioni come l'ellissometria quantistica o in protocolli di crittografia quantistica in cui la frequenza giochi un ruolo importante.
Come ultimo aspetto discuteremo un paio di applicazioni dell'entanglement quantistico. Prima di tutto analizzeremo l'utilizzo di fotoni anticorrelati in frequenza (prodotti mediante SPDC) per aumentare l'accuratezza della misura dei termini di dispersione di ordine dispari. In particolre mostremo, mediante simulazioni numeriche, che tale tecnica puó dare benefici in situazioni in cui il rapporto segnale-rumore sia basso.
Ci concentreremo poi sulla comunicazione quantistica, dimostrando per la prima volta la fattibilitá di un link a singolo fotone tra un satellite LEO e una stazione ottica a Terra. Nel contesto della Quantum Information, l'entanglement

é una risorsa preziosa, che puo' essere utilizzata in protocolli di comunicazione che non hanno analogo classico, per esempio per condividere una chiave segreta rivelando la presenza di spie nel canale (crittografia quantistica) o per aumentare la capacitá del canale (codifica superdensa).
La tecnologia spaziale offre la possibiltá di condividere fotoni entangled su scala globale, ma d'altra parte le difficoltá tecniche da superare per ricevere correttamente singoli fotoni da una sorgente in movimento veloce, in presenza di un forte rumore di background, sono molto grosse. Nel nostro esperimento abbiamo simulato una sorgente di singolo fotone su satellite usando la retroriflessione di un debole impulso laser da un cornercube del satellite, dimostrando che la corretta identificazione dei fotoni "buoni" é realmente possibile. Questa dimostrazione é un passo tecnologico fondamentale, che apre la pista a tutta una serie di esperimenti scientifici ed applicazioni tecnologiche della Quantum Information in campo spaziale.

Abstract

This work concerns the study of multiparametric entangled states generated by means of parametric downconversion, a nonlinear optical process through which a pump photon in two photons with peculiar spectral, spatial and polarization properties. These states have been employed for the last twenty years in experiments on the foundations of quantum mechanics as well as in quanum information applications, like quantum cryptography, quantum teleportation and quantum computing.
The first section of this thesis regards the manipulation of the spatial properties of the downconverted photons by means of a deformable mirror, and the study of the effectd in the temporal quantum interferogram. This is scientifically important as a tool to engineer entangled states and as a way to demonstrate a spatial counterpart of the well-known effect of dispersion cancellation (in the spectral domain). The second section concerns the characterization of optical states entangled in frequency and polarization: we introduce the concept of two-photon spectral coherence matrix as an extension of the classical spectral coherence matrix, suggesting an experimental technique to measure it. This would be important to characterize the polarization properties of broadband entangled states, in applications like spectroscopic quantum ellipsometry or quantum cryptography protocols which include the frequency degree of freedom.
Finally we will discuss a couple of applications of quantum entanglement.
First of all we will use the frequency anticorrelated states generated by SPDC, exploting the dispersion-cancellation effect, to enhance the accuracy of even-order dispersion terms. Particularly we show benefits of this technique in situations where the signal-to-noise ratio is low.
Second, we concentrate on quantum commnication, demostrating for the first time the feasibility of a single photon link between a LEO satellite and an Earth-based optical station. In quantum information contexts, quantum entanglement is a valuable resource, which can be exploited to design new protocols with no classical counterpart, for example to share a secret key detecting the presence of eavesdroppers on the channel (quantum cryptography) or to

enhance the channel capacity beyond Shannon limits (quantum dense coding). Satellite technology offers the possibility to share entangled photons globally, but, on the other hand, several technical issues must be overcome in order to correctly receive single photons from a fast moving source against a strong backgrund noise. Here we simulate a single photon source on a satellite using the retroreflection of a faint laser pulse by a satellite cornercube and we show that correct detection of the photons is indeed possible, opening the way to quantum information experiments on worlwide scales.

Chapter 1

Parametric downconversion and multiparameter optical entanglement

In this introductory Chapter we will review some quantum mechanics and we will introduce the concept of quantum entanglement. Then we will describe in details spontaneous parametric downconversion, a nonlinear optical process at the heart of most current sources of entangled photons. We will then review a few examples of quantum interferometric schemes.

1.1 Review of quantum mechanics

Each state of a quantum system is associated to a vector $|\psi>$ in a Hilbert space. For multiparticle systems the global Hilbert space is the tensor product of the single-particle Hilbert spaces.
Any observable quantity, on the other hand, is associated to a self-adjoint linear operator A, which has eigenvectors $|a_i>$ and real eigenvalues α_i:

$$A|a_i>=\alpha_i|a_i> \tag{1.1}$$

Every quantum state $|\psi>$ can be expanded as a linear combination of the eigenstates of A (superposition principle):

$$|\psi>=\sum_i \chi_i|a_i> \tag{1.2}$$

where $\chi_i =<\psi|a_i>$. The probability of getting the value α_k is:

$$P_k = |<\alpha_k|\psi>|^2 \tag{1.3}$$

while the mean value of the results for a measurement of A is given by:

$$< A >=< \psi|A|\psi > \tag{1.4}$$

If the quantity A is measured, the state will randomly collapse onto one of the states in the superposition, for example $|a_k >$ (and therefore giving the result α_k), with a probability proportional to the square of the amplitude of that eigenstate in the linear combination ($|\chi_k|^2$). Since the superposition is coherent, i.e. there is a fixed phase relationship between the eigenstates in the superposition, interference effects between probability amplitudes can be observed.
In 1927 Werner Heisemberg introduced the famous indeterminacy principle. According to this principle it is impossible to measure simultaneously the position and the momentum of a particle, since the measurement of one of these necessarily introduces a perturbation on the other. Mathematically, given two operators A and B:

$$< (\Delta A)^2 >< (\Delta B)^2 >\geq \frac{| < [A, B] > |^2}{4} \tag{1.5}$$

that is, if A and B do not commute, the product of there indeterminacies must be greater than a certain constant: reducing the uncertainty on the measurement of A will increase the indeterminacy on B.

1.1.1 Quantum Entanglement and EPR paradox

Let's consider two quantum systems, described in the Hilbert space H, which is the tensor product of the spaces H_A and H_B where the two subsystems are described. A pure state on $H_A \otimes H_B$ is entangled when it cannot be written as a product state. An example of entangled state is the two-particle singlet state:

$$|\psi >= \frac{1}{2} [|0_A 1_B > -|1_A 0_B >] \tag{1.6}$$

The necessary ingredients to have an entangled states are two:

- correlation: the result for measurements performed on particle A and on particle B are correlated. For example using the $\{|0 >, |1 >\}$ basis, if a measurement on particle A gives 0 then a measurement on particle B will give 1, and viceversa
- superposition: there is a linear combination of possibilities, which gives rise to interference effects

In 1935 Einstein, Podolsky and Rosen [1] proposed a thought experiment to formalize what they felt as an inconsistency of quantum theory (which later became famous as "EPR paradox"). They argued that physical quantities which can be predicted with certainty must be "elements of reality" and for that theory to be "complete" these values must therefore be incorporated into the description of the system. So, if quantum mechanics is complete, non-commuting observables A and B can never be simultaneously elements of reality, since if the outcome of a measurement of A can be predicted with certainty, the outcome of a measurement of B cannot. This was suggested as a proof that quantum theory is not complete and it is therefore an unsatisfactory theory.
Consider a two-particle state described by Eq. 1.6. If one performs a measurement on particle A, he will get half of the times the result 0 and half of the times the result 1, but there is no way to predict the result of a single specific measurement. But on the other hand, once a measurement is performed on particle A giving a certain value, the complementary value will be retrieved with unity probability from a measurement on particle B.
Einstein was bothered by the fact that a measurement on the first particle seemed to instantaneously affect the result of the measurement on the second particle (nonlocality), since it seemed to contradict the theory of relativity, according to which nothing can travel faster than light. He called this effect "spooky action at a distance" and claimed that this necessarily showed the incompleteness of the quantum description of the world. If quantum mechanics was not complete then there was some kind of "hidden variables" that had not been taken into account which could solve the paradox.

1.1.2 Bell inequalities

In 1964 John Bell introduced a clear mathematical formulation for the problem [2], showing that the implicit assumption behind EPR argument is that physics should be characterized by:

- realism: every measurable quantity should have a definite value regardless whether the measurement is made or not

- locality: no property can be instantaneously shared by two spatially separated systems

Consider the singlet state in Eq. 1.6. Suppose to let the photons fly apart and measure polarization on photon A in the basis rotated of an angle α with respect to the $\{H, V\}$ basis, and on photon B in the basis rotated of an angle

β. Let's define the correlation coefficient:

$$E(\alpha,\beta) = P_{++}(\alpha,\beta) + P_{--}(\alpha,\beta) - P_{+-}(\alpha,\beta) - P_{-+}(\alpha,\beta) \tag{1.7}$$

Performing the calculations according to the rules of quantum mechanics one finds:

$$E(\alpha,\beta) = -\cos(\beta-\alpha) \tag{1.8}$$

For pairs of analyzers with the same orientation ($\beta = \alpha$) quantum mechanics predicts perfect anticorrelation: $E = -1$.
If we define then the quantity:

$$S(\alpha,\alpha',\beta,\beta') = E(\alpha,\beta) - E(\alpha,\beta') + E(\alpha',\beta) + E(\alpha',\beta') \tag{1.9}$$

it can be shown (see next paragraph) that, for any realist local theory (comprising local hidden variables) the Clauser-Horne-Shimony-Holt (CHSH) inequality holds [3]:

$$|S(\alpha,\alpha',\beta,\beta')| \leqslant 2 \tag{1.10}$$

while quantum mechanics predicts:

$$S = 2\sqrt{2} \tag{1.11}$$

This way we have a way to test quantum mechanics against classical hidden-variable theories. Many successful experiments to violate Bell inequalities have been performed since the first one in 1982 by A. Aspect and coworkers [4].

Derivation of CHSH inequality

Let's consider a hidden variable λ whose value is distributed with a probability density $\rho(\lambda)$. Suppose to have a source of linearly-polarized pairs of photons: each photon is measured by a polarization-analyzer which gives the result $+1$ if the photon is transmitted or -1 if the photon is absorbed. The analyzer I is set at an angle α and the analyzer II at an angle β. The possible measurement results are described by the functions $A(\lambda,\alpha)$ in I and $B(\lambda,\beta)$ in II which have, as possible outcomes, $+1$ and -1.
Let's define the functions:

$$\frac{1}{2}[1 + A(\lambda,\alpha)] = \begin{cases} 1 & A = +1 \\ 0 & A = -1 \end{cases} \tag{1.12}$$

$$\frac{1}{2}[1 - B(\lambda,\alpha)] = \begin{cases} 1 & B = -1 \\ 0 & B = 0 \end{cases} \tag{1.13}$$

So, the probability of having a photon through the analizer I at angle α and not having a photon through the analyzer II at angle β is:

$$P_{+-}(\alpha,\beta) = \int d\lambda\rho(\lambda)\frac{[1+A(\lambda,\alpha)]}{2}\frac{[1-B(\lambda,\beta)]}{2} \tag{1.14}$$

Using similar expressions for P_{++}, P_{+-} and P_{--} in Eq. 1.7 one can find for the correlation function:

$$E(\alpha,\beta) = \int d\lambda\rho(\lambda)A(\lambda,\alpha)B(\lambda,\beta) \tag{1.15}$$

Now, if we consider:

$$\begin{aligned} s(\lambda;\alpha,\alpha',\beta,\beta') = A(\lambda,\alpha)B(\lambda,\beta) - A(\lambda,\alpha)B(\lambda,\beta')+ \\ A(\lambda,\alpha')B(\lambda,\beta) + A(\lambda,\alpha')B(\lambda,\beta') \end{aligned} \tag{1.16}$$

then $s(\lambda;\alpha,\alpha',\beta,\beta')$ can only assume the values $+2$ or -2. Therefore if we take its mean value:

$$S(\lambda;\alpha,\alpha',\beta,\beta') = \int d\lambda\rho(\lambda)s(\lambda;\alpha,\alpha',\beta,\beta') \tag{1.17}$$

then Eq. 1.10 must hold.

1.2 Spontaneous parametric downconversion

Spontaneous parametric down-conversion (SPDC) is an optical process in which a pump photon, due to nonlinear interactions in a $\chi^{(2)}$ material, is split in two photons concurrently entangled in wave-vector, frequency and polarization. The effect was predicted by D. N. Klyshko [5] and observed indipendently by three groups in 1967: Harris and Byer [6] at Stanford, Magde and Mahr [7] at Cornell, and a group of people at Moscow State University.
The phenomenon started to be studied intensively as a tunable source of radiation, or as the main source of noise in low-gain optical parametric amplifiers and frequency converters and more sophisticated theoretical quantum models were introduced ([8, 9]). In 1970 Burnham and Weinberg [10] verified the simultaneity of emission of the product photons, by means of coincidence observation: they recorded a drop of the coincidence rate to the calculated accidental value unless the two detectors were arranged to satisfy energy and momentum conservation and had equal time delays. In their measurement they found that the value of the correlation time T_C between the down-converted photons was limited by the time resolution of the electronics (of the order of 4 ns) and

speculated that it might have been related to the coherence time of the pump beam (which was far below the instrumental resolution limit). A successive analysis by Hong and Mandel [11] showed that T_C had nothing to do with the bandwidth of the pump field, but was ultimately limited by the acceptance bandwidth of the downconverted light: in particular T_C can be shorter than the propagation time through the nonlinear medium. The process was then recognized as capable of providing with a couple of highly correlated photons with extremely small time separation.
A major breakthrough in the field was the measurement of T_C by means of fourth-order interference performed in 1987 by Hong, Ou and Mandel [12]. This kind of setup, capable of accurately measuring subpicosecond delay times between single photons is called HOM interferometer and will be examined in details in Section 1.3.1.
We will now present a derivation of the optical state at the output of the nonlinear crystal and we will then discuss a few more interesting properties of downconverted light.

1.2.1 Quantum theory of parametric downconversion

In a medium with a $\chi^{(2)}$ nonlinearity an incident electric field $\mathbf{E}$ will induce a polarization $\mathbf{P}$ with bilinear terms in $\mathbf{E}$. The classical interaction energy is:

$$\begin{aligned} W_I &= \frac{1}{2}\sum_i \int_V P_i(\mathbf{r},t)E_i(\mathbf{r},t)d\mathbf{r} \\ &= \frac{1}{2}\sum_{ijk} \int_V \chi_{ijk}E_i(\mathbf{r},t)E_j(\mathbf{r},t)E_k(\mathbf{r},t)d\mathbf{r} \end{aligned}$$

When the electric field is quantized $\mathbf{E}(\mathbf{r},t)$ becomes an operator on the Hilbert space, which can be decomposed in a positive-frequency part $\hat{\mathbf{E}}^{(+)}(\mathbf{r},t)$ and a negative-frequency part $\hat{\mathbf{E}}^{(-)}(\mathbf{r},t)$:

$$\hat{\mathbf{E}}(\mathbf{r},t) = \hat{\mathbf{E}}^{(+)}(\mathbf{r},t) + \hat{\mathbf{E}}^{(-)}(\mathbf{r},t) \qquad \hat{\mathbf{E}}^{(-)}(\mathbf{r},t) = [\hat{\mathbf{E}}^{(-)}(\mathbf{r},t)]^\dagger \tag{1.18}$$

$$\hat{\mathbf{E}}^{(+)}(\mathbf{r},t) = i\sum_{\mathbf{k},\lambda} \sqrt{\frac{\hbar\omega_k}{2\epsilon_0 V}}\mathbf{e}_{\mathbf{k},\lambda}\hat{a}_{\mathbf{k},\lambda}e^{i(\mathbf{k}\cdot\mathbf{r}-\omega t)} \tag{1.19}$$

The quantum interaction hamiltonian is therefore:

$$H_I = \frac{1}{V}\sum_{ijk} \int_V \chi_{ijk}E_i^{(+)}(\mathbf{r},t)E_j^{(+)}(\mathbf{r},t)E_k^{(-)}(\mathbf{r},t)d\mathbf{r}$$

Let's make some assumptions:

- the pump is a monochromatic plane wave at frequency Ω_P, vertically polarized, propagating along the z axis. We assume it is undepleted in the process and can be treated classically. It can therefore be expressed by:
$$E_P(\mathbf{R},t) = E_0 e^{i(k_p z - \Omega_P t)} \tag{1.20}$$

- the phase-matching conditions are imposed so as to have the signal photon with polarization s and the idler photon with polarization i, with $s,i = H,V$.

- the quasi-monochromatic paraxial approximation is valid for the down-converted photons:
$$E_i^{(+)}(\mathbf{r},t) = i\sum_{\mathbf{q},\omega}\sqrt{\frac{\hbar\omega}{2\epsilon_0 V}}\hat{a}_{\mathbf{q},\omega}e^{i[\kappa(\mathbf{q},\omega)z+\mathbf{q}\cdot\rho-\omega t]} \tag{1.21}$$
where $\rho = (x,y)$ and $\kappa(\mathbf{q},\omega) = \sqrt{(\frac{n_i\omega}{c})^2 - |\mathbf{q}|^2}$

- the nonlinear crystal is assumed infinite in the x-y plane and of thickness L in the z direction

Since the effect is weak we can use the time-dependent perturbation theory up to the linear term:
$$|\psi> \approx \int dt H_I(t)|0> \tag{1.22}$$
Substituting:
$$|\psi> \approx \sum_{\mathbf{q}_s,\mathbf{q}_i}\sum_{\omega_s,\omega_i}\int dt\int d\rho\int_{-L}^{0} dz\chi E_0 e^{i[k_p-\kappa(\mathbf{q}_s,\omega_s)-\kappa(\mathbf{q}_i,\omega_i)]z} e^{i(\mathbf{q}_s-\mathbf{q}_i)\cdot\rho}e^{i(\Omega_P-\omega_s-\omega_i)t}\hat{a}^\dagger_{\mathbf{q}_s,\omega_s}\hat{a}^\dagger_{\mathbf{q}_i,\omega_i}|0> \tag{1.23}$$
From the integrations over time and position:

- transverse momentum is conserved:
$$\int d\rho e^{i(\mathbf{q}_s-\mathbf{q}_i)\cdot\rho} \approx \delta(\mathbf{q}_s-\mathbf{q}_i) \tag{1.24}$$

- energy is conserved:
$$\int dt e^{i(\Omega_P-\omega_s-\omega_i)t} \approx \delta(\Omega_P-\omega_s-\omega_i) \tag{1.25}$$
This can be expressed also as frequency anticorrelation: if one photon is at frequency ω_s the other is at frequency $\Omega_P - \omega_s$

If we define the phase mismatch function as:

$$\Delta(\mathbf{q}_s, \omega_s; \mathbf{q}_i, \omega_i) = k_p - \kappa(\mathbf{q}_s, \omega_s) - \kappa(\mathbf{q}_i, \omega_i) \tag{1.26}$$

we end up with:

$$|\psi^{(2)}>= \int d\mathbf{q_s} d\mathbf{q_i} d\omega_s d\omega_i \tilde{\Phi}(\mathbf{q_s}, \mathbf{q_i}; \omega_s, \omega_i) \hat{a}_s^\dagger(\mathbf{q_s}, \omega_s) \hat{a}_i^\dagger(\mathbf{q_i}, \omega_i)|0> \tag{1.27}$$

where

$$\tilde{\Phi}(\mathbf{q_s}, \mathbf{q_i}; \omega_s, \omega_i) = \delta(\omega_s - \Omega_P + \omega_i)\delta(\mathbf{q_s} + \mathbf{q_i}) \int dz \chi(z) e^{i\Delta(\mathbf{q}_s, \omega_s; \mathbf{q}_i, \omega_i)z} \tag{1.28}$$

The form of the function $\tilde{\Phi}(\mathbf{q_s}, \mathbf{q_i}; \omega_s, \omega_i)$ will be determined by the specific phase-matching conditions and by the distribution of nonlinearity inside the crystal. For a bulk crystal of length L:

$$\chi(z) = \chi_0 \Pi\left[\frac{z}{L} + \frac{1}{2}\right] \qquad \Pi[x] = \begin{cases} 1 & |x| \leq \frac{1}{2} \\ 0 & |x| > \frac{1}{2} \end{cases} \tag{1.29}$$

so that:

$$\begin{aligned} \tilde{\Phi}(\mathbf{q_s}, \mathbf{q_i}; \omega_s, \omega_i) = L\delta(\omega_s - \Omega_P + \omega_i)\delta(\mathbf{q_s} + \mathbf{q_i}) e^{\Delta(\mathbf{q}_s, \omega_s; \mathbf{q}_i, \omega_i)L/2} \\ Sinc[\Delta(\mathbf{q}_s, \omega_s; \mathbf{q}_i, \omega_i)L/2] \end{aligned} \tag{1.30}$$

1.2.2 Phase-matching

We will now derive approximate expression for the phase mismatch function $\Delta(\mathbf{q}_s, \omega_s; \mathbf{q}_i, \omega_i)$ in the case of type-I and type-II collinear phase-matching.

Type-I phase-matching

In type-I phase-matching the downconverted photons have the same polarization, for example according to the scheme:

$$e \rightarrow o + o$$

Assuming nondegenerate case the central frequencies of the photons are different ($\Omega_s \neq \Omega_i$) but, due to energy conservation:

$$\omega_s = \Omega_s + \nu \qquad \omega_i = \Omega_i - \nu \tag{1.31}$$

and due to transverse momentum conservation:

$$\mathbf{q}_s = \mathbf{q} \qquad \mathbf{q}_i = -\mathbf{q} \tag{1.32}$$

So:

$$\kappa(\mathbf{q}_s, \omega_s) = \sqrt{(\frac{n(\Omega_s + \nu)(\Omega_s + \nu)}{c})^2 - |\mathbf{q}|^2} \tag{1.33}$$

$$\kappa(\mathbf{q}_i, \omega_i) = \sqrt{(\frac{n(\Omega_i - \nu)(\Omega_s - \nu)}{c})^2 - |\mathbf{q}|^2} \tag{1.34}$$

$$\tag{1.35}$$

Expanding in Taylor series one finds:

$$\Delta \approx -\nu D + \frac{|\mathbf{q}|^2}{\tilde{K}} \tag{1.36}$$

where:

$$\frac{1}{\tilde{K}} = \frac{1}{2}\left(\frac{1}{K_s} + \frac{1}{K_i}\right) \tag{1.37}$$

$$D = \frac{1}{u_0(\Omega_s)} - \frac{1}{u_0(\Omega_i)} \tag{1.38}$$

and u_0 is the group velocity of the ordinary ray through the crystal.

If there is perfect phase matching ($\Delta = 0$) Eq. (1.36) describes in the far-field a set of concentric circles with different radii for different frequencies.

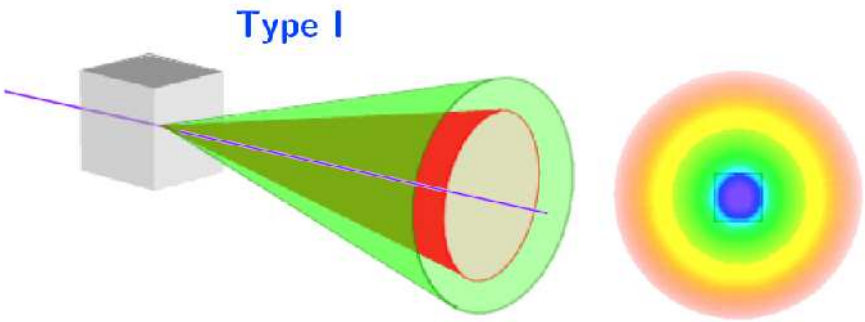

Figure 1.1: Far-field emission pattern for type-I downconversion. The photons are emitted along concentic cones, with radii dependent on the frequency. The frequencies of the signal (ω_s) and idler (ω_i) photons are anticorrelated, meaning that $\omega_i = \Omega_P - \omega_s$.

In the case of degenerate collinear type-I downconversion ($\Omega_s = \Omega_i = \Omega_P/2$) there is no group delay between the photons (D=0) so we must resort to the second-order term in angular frequency:

$$\Delta \approx -\nu^2 D' + \frac{|\mathbf{q}|^2}{K_0} \tag{1.39}$$

where

$$D' = \frac{d}{d\nu}\left[\frac{1}{u_0(\Omega_0+\nu)}\right]_{\nu=0} \tag{1.40}$$

Type-II phase-matching

In type-II phase-matching the downconverted photons have opposite polarization, for example according to the scheme:

$$e \to e + o$$

As for type-I SPDC one needs to expand the phase mismatch function on a Taylor series. Let's consider just the degenerate case, which we will employ in our experiments. For the ordinary ray we simply have:

$$\kappa_o(\mathbf{q},\nu) \backsimeq K_o + \frac{\nu}{u_o} - \frac{|\mathbf{q}|^2}{2K_o} \tag{1.41}$$

For the extraordinary ray the situation is more complicated since the refractive index depends also in the direction of propagation. In the end one finds (see [13]):

$$\kappa_e(\mathbf{q},\nu) \backsimeq K_e + \frac{\nu}{u_e} - \frac{|\mathbf{q}|^2}{2K_o} + M\mathbf{e}_2 \cdot \mathbf{q} \tag{1.42}$$

where $\mathbf{e}_2$ is the direction of the optical axis of the crystal, and

$$D = \frac{1}{u_o} - \frac{1}{u_e} \tag{1.43}$$

$$M = \frac{\partial}{\partial\theta_e} \ln\left[n_e\left(\frac{\Omega_P}{2}, \theta_e\right)\right]$$

to

(1.45)

For the phase mismatch we therefore get:

$$\Delta \approx -\nu D + \frac{2|\mathbf{q}|^2}{\tilde{K}_p} + M\mathbf{e}_2 \cdot \mathbf{q} \tag{1.46}$$

This time the cones along which the photons are emitted are not collinear concentric anymore, but are tilted with respect to one another due to spatial walkoff.

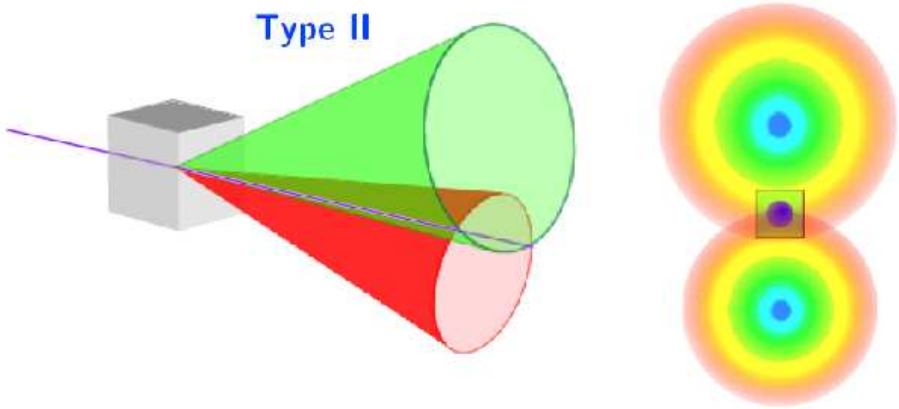

Figure 1.2: Far-field emission pattern for the downconverted photons in type-II SPDC. The photons are emitted alond two cones: the cone for the extraordinary beam is tilted with respect to the ordinary one due to the spatial walkoff in birefringent phase-matching.

1.2.3 Multiparameter entanglement

The optical state generated in parametric processes is clearly multiparametric, in the sense that the state parameters (polarization, frequency and wavevector) are correlated one with respect to the others. In Fig. 1.3 one can see the correlation between the emission directions of the photons along the vertical axis (parameter q) and shift ν from the central frequency Ω_0.

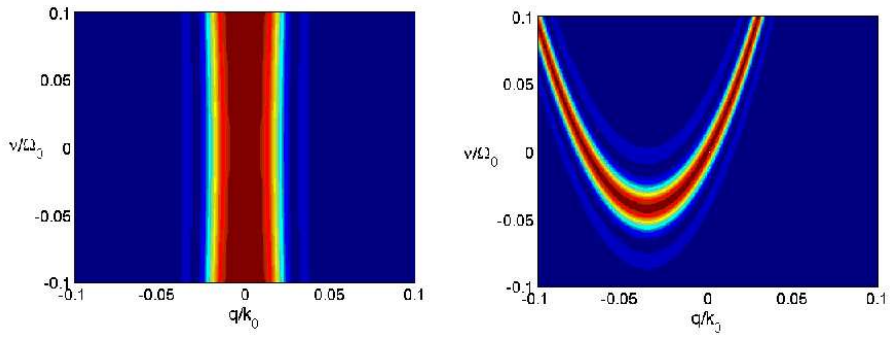

Figure 1.3: Correlation between frequency and emission angle in parametric downconversion. Correlations are stronger in type-II birefringent phase-matching (right side) than they are in type-I (left side).

Clearly, in type I downcovertion frequency and emission directions are very weakly correlated, while for type-II downconversion, in the case of birefringent phase-matching the correlations are much stronger, due to the spatial walkoff.

In Fig. 1.4 one can see that if we restrict to a small area around the collinear emission, the correlation can be supposed to be almost linear.

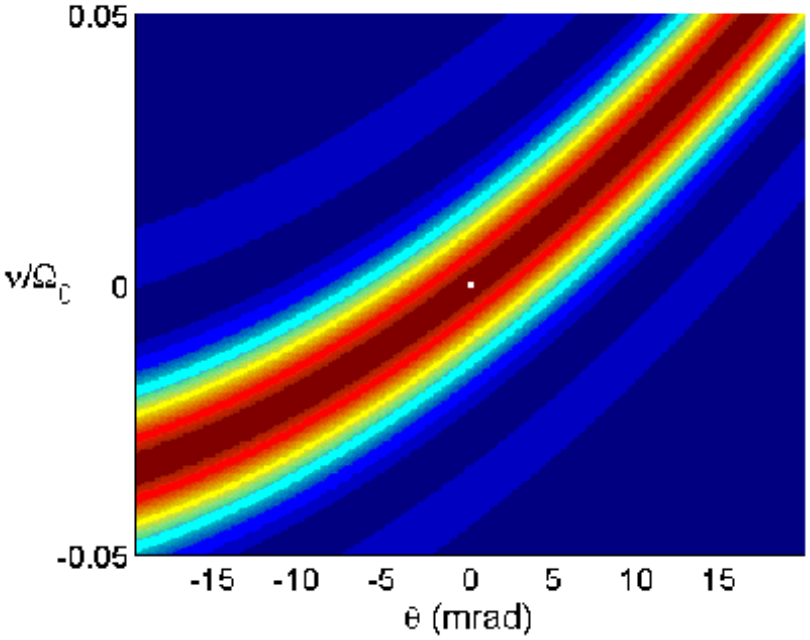

Figure 1.4: Correlation between emission angle and frequency for type-II birefringent phase-matching: the correlation function is almost linear.

1.3 Quantum Interferometry using SPDC light

Spontaneous parametric downconversion has been used since the seminal HOM experiment to perform fourth-order interference experiments. Normally, in this kind of experiments, a single spatial mode ($\mathbf{q} = \mathbf{0}$)is ideally selected by means of small apertures, so that only the frequency and polarization degrees of freedom are relevant. Under this approximation the state can be approximated as:

$$|\psi> \quad \approx \quad \int d\nu \Phi(\nu) \hat{a}_s^\dagger(\Omega_0 + \nu) \hat{a}_i^\dagger(\Omega_0 - \nu)|0> \tag{1.47}$$

If we consider just degenerate emission, the emission spectra $\Phi(\nu)$ for type-I and type-II phase matching in a BBO crystal pumped with 351 nm light ($cD = 0.07, \quad c^2 D' = 3.4 \cdot 10^{-3} \mu m$) are shown in Fig. 1.5. We will review the most important configurations using type-I and type-II downconversion.

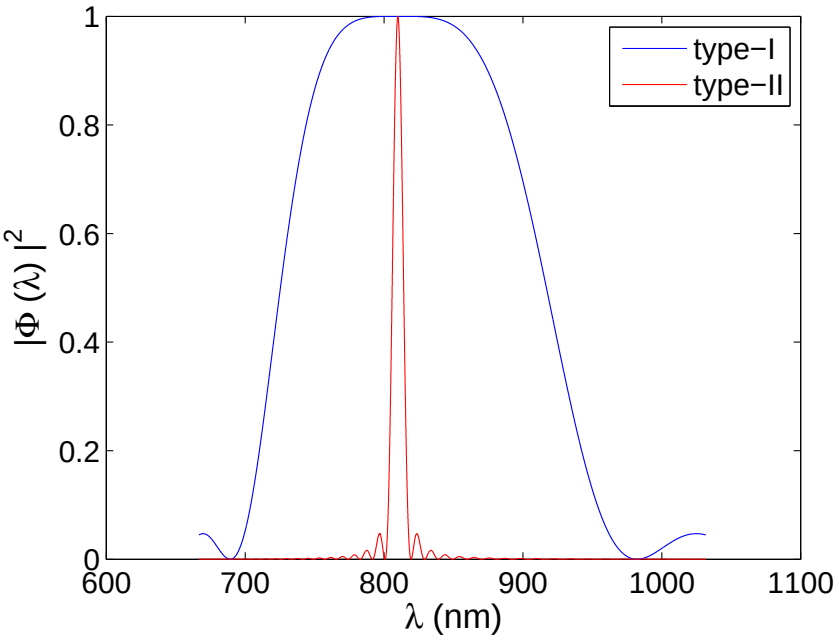

Figure 1.5: Spectrum for degenerate type-I and type-II parametric downconvertion in the single spatial mode $\mathbf{q} = \mathbf{0}$ *for a 1-mm long BBO crystal. The spectrum for type-II is narrower since the dominant term in the phase-mismatch function is the linear one, due to the group velocity difference between the ordinary and extraordinary photons, while for type-II the dominant term is the quadratic one.*

1.3.1 HOM interferometer

For a 50:50 beamsplitter, assuming the reflected beam suffers a $\pi/2$ phase shift, the input and output modes are related according to:

$$\hat{a}_A = \frac{1}{\sqrt{2}}(\hat{a}_1 + i\hat{a}_2) \qquad \hat{a}_B = \frac{1}{\sqrt{2}}(i\hat{a}_1 + \hat{a}_2) \tag{1.48}$$

When two monochromatic single photons are injected into the two input ports of a beamplitter the output state will be:

$$\begin{aligned} |1>_1 |1>_2 \longrightarrow & \frac{1}{2}(\hat{a}_A^\dagger + i\hat{a}_B^\dagger)(i\hat{a}_A^\dagger + \hat{a}_B^\dagger)|0>_A |0>_B \\ & = \frac{i}{2}(\hat{a}_A^\dagger \hat{a}_A^\dagger + \hat{a}_B^\dagger \hat{a}_B^\dagger)|0>_A |0>_B \end{aligned} \tag{1.49}$$

So, the photons will emerge either both from port A or both from port B and detector placed in the output beams will never register coincidence events.

This effect is due to the interference between the probability amplitudes of going though a certain path. We can detect a coincidence event as a result of two possible events:

- both photons are transmitted (probability amplitude $A_T = \frac{1}{\sqrt{2}} \cdot \frac{1}{\sqrt{2}} = \frac{1}{2}$)
- both photons are reflect, acquiring a $\pi/2$ phase shift (probability amplitude $A_R = \frac{i}{\sqrt{2}} \cdot \frac{i}{\sqrt{2}} = -\frac{1}{2}$)

So the probability of having a coincidence is:

$$P_{Coinc} = |A_T + A_R|^2 = 0 \tag{1.50}$$

Without interference filters

If the photons are not monochromatic, as the ones produced in SPDC, there can be interference only if they arrive to the beamsplitter within a time shorter than their correlation time. In a setup like the one on the left in Fig. (1.6), introducing a delay τ between the photons, we get zero coincidences when the paths are exactly equal, while we get coincidences outside the coherence time of the photon pair.
Mathematically the fields out of the crystal are:

$$E_{A,B}(t_{A,B}) = \int d\omega e^{-i\omega t_{A,B}} \hat{a}_{A,B}(\omega) \tag{1.51}$$

After the beamsplitter, as set by Eq. (1.48), the field are:

$$E_1(t_1) = \frac{1}{2}\left\{\int d\omega e^{-i\omega t_1} e^{i\omega\tau} \hat{a}_A(\omega) + i\int d\omega e^{-i\omega t_1} \hat{a}_B(\omega)\right\} \tag{1.52}$$

$$E_2(t_2) = \frac{1}{2}\left\{i\int d\omega e^{-i\omega t_2} e^{i\omega\tau} \hat{a}_A(\omega) + \int d\omega e^{-i\omega t_2} \hat{a}_B(\omega)\right\} \tag{1.53}$$

The expression for the coincidence count rate is:

$$\begin{aligned} R(\tau) &= \int dt_1 dt_2 |<0|E_2^{(-)}(t_2)E_1^{(-)}(t_1)|\psi>|^2 \\ &= R_0 - \int d\omega \Phi^*(\omega)\Phi(-\omega)e^{i\omega\tau} \end{aligned} \tag{1.54}$$

with

$$R_0 = \int d\omega |\Phi(\omega)|^2 \tag{1.55}$$

This kind of setup was used by Hong, Ou and Mandel in 1987 to measure the correlation time of the downconverted photons [12].

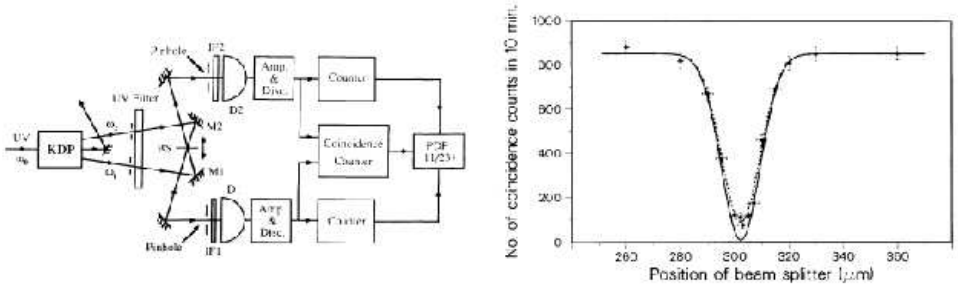

Figure 1.6: On the left, the experimental apparatus used by Hong, Ou and Mandel to measure the correlation time T_C of the downconverted photons. On the right their experimental data, showing a coherence time of about 100 fs. (From [12])

1.3.2 Type-II interferometry

Type-II collinear phase matching can produce a state which exhibits frequency entanglement and polarization correlation (one photon is H-polarized and the other V-polarized). If we put narrowband filters and just concentrate on polarization properties, supposing to let the beam through a non-polarizing beamsplitter we get:

$$\begin{aligned} |o,e>_1 |vac>_2 \longrightarrow & \frac{1}{2}(\hat{a}^\dagger_{Ao} + i\hat{a}^\dagger_{Bo})(i\hat{a}^\dagger_{Ae} + \hat{a}^\dagger_{Be})|vac>_A |vac>_B \\ & = \frac{i}{2}(\hat{a}^\dagger_{Ao}\hat{a}^\dagger_{Ae} + \hat{a}^\dagger_{Ae}\hat{a}^\dagger_{Bo} + \hat{a}^\dagger_{Ao}\hat{a}^\dagger_{Be} + \hat{a}^\dagger_{Be}\hat{a}^\dagger_{Bo})|vac>_A |vac>_B \end{aligned} \tag{1.56}$$

Since we are detecting coincidences the terms with the two photons going out through the same port do not contribute. This way, from polarization correlation we have created polarization entanglement:

$$|\psi> = \frac{1}{\sqrt{2}}(\hat{a}^\dagger_{Ae}\hat{a}^\dagger_{Bo} + \hat{a}^\dagger_{Ao}\hat{a}^\dagger_{Be})|vac>_A |vac>_B \tag{1.57}$$

At this point we have no interference between the photons because they are distinguishable, being in different polarization modes. If we put two polarizer, one oriented at an angle θ_1, the other at an angle θ_2 before the detectors, we get:

$$\begin{aligned} |\psi> = \frac{1}{\sqrt{2}} & \sin(\theta_1 - \theta_2) \left\{ \cos\theta_1 \hat{a}^\dagger_{1H} + \sin\theta_1 \hat{a}^\dagger_{1V} \right\} \\ & \left\{ \cos\theta_2 \hat{a}^\dagger_{2H} + \sin\theta_2 \hat{a}^\dagger_{2V} \right\} |0> \end{aligned} \tag{1.58}$$

So that the probability of having a coincidence is:

$$P_{12}(\theta_1, \theta_2) = \sin^2(\theta_1 - \theta_2) \tag{1.59}$$

If $\theta_1 = \theta_2$ the two possible paths that can give a coincidence event are indistinguishable, leading to quantum interference and complete cancellation of the coincidence rate. The quantum interference effect can be seen in Fig. (1.7)

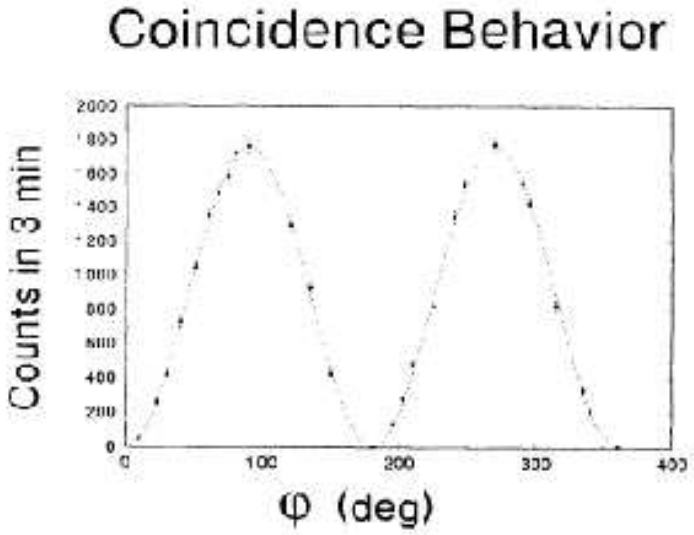

Figure 1.7: Polarization interference in type-II parametric downconversion. Measurement of coincidences as a function of $\phi = \theta_1 - \theta_2$, for fixed $\theta_1 = 45$ degrees and variable θ_2 is plotted (from ??)

Without interference filters

If we consider no spectral filtering of the downconverted photons, we have cuncurrent entanglement in frequency and polarization. Therefore, polarization interference can happen only within the coherence time T_C and, on the other hand, the visibility of spectral interference depends on the orientation of the polarization analyzers.
The biphoton probability amplitude is:

$$\begin{aligned} A(t_1, t_2) &= < 0|E_2^{(-)}(t_2)E_1^{(-)}(t_1)|\psi > \\ &= \sin_2 \cos\theta_1 e^{i\Omega_0(t_1+t_2)} \int d\nu e^{i\nu\tau}\Phi(\nu) \\ &\quad \left[\sin\theta_2 \cos\theta_1 e^{i\nu(t_1-t_2)} - \sin\theta_1 \cos\theta_2 e^{-i\nu(t_1-t_2)}\right] \end{aligned} \tag{1.60}$$

and the visibility function results:

$$V(\tau;\theta_1,\theta_2) = 1 - \frac{R(\tau)}{R_0} \tag{1.61}$$

where:

$$R_0 = (\sin^2\theta_2\cos^2\theta_1 + \sin^2\theta_1\cos^2\theta_2)\int d\nu|\Phi(\nu)|^2 \tag{1.62}$$

and

$$R(\tau) = \sin\theta_1\cos\theta_2\cos\theta_1\cos\theta_2\int d\nu\Phi^*(\nu)\Phi(-\nu)e^{2i\nu\tau} \tag{1.63}$$

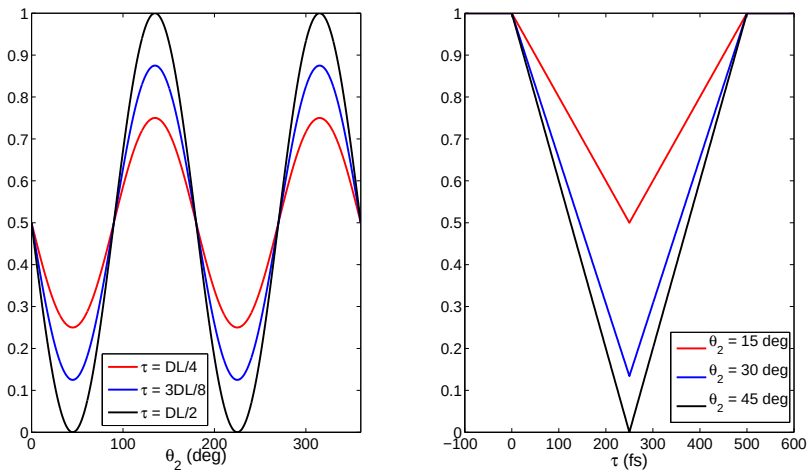

Figure 1.8: Polarization interference in type-II parametric downconversion without interference filters. On the left, polarization interference for different time-dalays between the photons. On the right, temporal interference for different analyzer settings.

As shown in the simulations in Fig. 1.8 we have full-visibility in the polarization interference only when we set the delay to $\tau = \frac{DL}{2}$, bringing back the two photons to a separation shorter than their coherence time. On the other hand, high visibility in the temporal interference can be obtained only restoring complete polarization indistinguishability, that is setting the analyzers at 45 degrees.

1.3.3 Dispersion cancellation

Dispersion cancellation was predicted by Franson in 1992 [14] and demonstrated experimentally shortly after by Steinberg and coworkers [15]. Consider

a HOM interferometer and suppose to insert a slice of dispersive material, described by the transfer function $T(\omega) = t(\omega)e^{i\phi(\omega)}$ in one arm. Repeating the calculations in Section 1.3.1 one finds the following expression for the coincidence count rate:

$$C(\tau) = C_0 + 2Re\left[\int_{-\infty}^{\infty} \zeta^*(\Omega)\zeta(-\Omega)e^{j\Phi(\omega_0-\Omega)}e^{-j\Phi(\omega_0+\Omega)}d\Omega\right] \tag{1.64}$$

with:

$$C_0 = 2\int_{-\infty}^{\infty} |\zeta(\Omega)|^2 d\Omega \tag{1.65}$$

As we said, this configuration exhibits even-order dispersion cancelation; if we expand $\Phi(\Omega)$ in Taylor series:

$$\Phi(\omega_0 + \Omega) = \sum_{n=0}^{\infty} \phi_n \Omega^n \qquad \phi_n = \frac{1}{n!}\frac{d^n\Phi}{d^n\omega}(\omega)|_{\omega=\omega_0} \tag{1.66}$$

where of course ϕ_1 is the group delay (GD) and ϕ_2 is the group delay dispersion (GDD), then only the odd-order terms contribute to the interferogram:

$$\Gamma(\Omega) = \Phi(\omega_0 + \Omega) - \Phi(\omega_0 - \Omega) = \sum_{n=0}^{\infty} \gamma_{2n+1}\Omega^{2n+1}, \quad \gamma_{2n+1} = 2\phi_{2n+1} \tag{1.67}$$

1.4 SPDC as a surce of polarization-entangled photons

Particularly important, especially in quantum information context, is the production of photon pairs entangled in polarization. Different approaches have been studied in order to create bright sources: we will give a brief overview of the subject.

1.4.1 Two type-I crystals

A source of polarization-entangled photons can be realized putting together two thin nonlinear crystals cut for type-I phase matching, with perpendicular optic axes. A pump beam polarized at 45 degrees will generate downconverted photons either in the first and second crystals and the two processes will be coherent as long as the emission spatial modes will be indistinguishable.

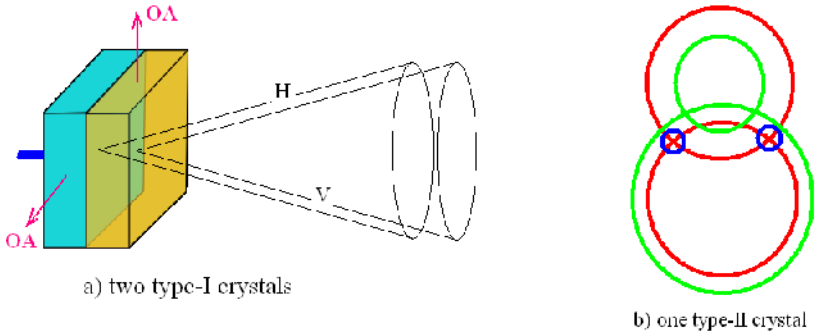

Figure 1.9:

1.4.2 Non-collinear type-II

In type-II noncollinear SPDC the photons are emitted in two spatially tilted cones, one for the H-polarized photon and the other for the V-polarized photon. Picking up the emission at the intersection (T_1 and T_2) of the cones one does not know if he is collecting the H-polarized photon in T_1 and the V-polarized photon in T_2 or viceversa, obtaining the state:

$$|\psi>=\frac{1}{\sqrt{2}}[|H_1>|V_2>+e^{i\phi}|V_1>|H_2>] \tag{1.68}$$

1.4.3 Other approaches

Recently fiber sources of polarization entangled photons have been developed, based on processes different from SPDC, like the Kerr nonlinearity of the fiber itself (which is a $\chi_{(3)}$ process). When the pump wavelength is close to the zero-dispersion wavelength of the fiber, phase-matching is achieved and the probability of inhelastic four-photon scattering is enhanced. In this process, two pump photons at frequency ω_P are converted in two Stokes and anti-Stokes photons, predominantly co-polarized with the pump beam. Polarization entanglement can be created by coherently adding two such processes.
Other recent experiments have employed photonic crystal fibers as nonlinear material.

Chapter 2

Multiparameter Entangled-State Engineering using Adaptive Optics

As described in Chapter 1, spontaneous parametric down-conversion is an optical process in which a pump photon, due to nonlinear interactions in a $\chi^{(2)}$ material, is split in two photons concurrently entangled in wave-vector, frequency and polarization. The states generated by this process have been used in experiments on the foundations of quantum mechanics, as well as in applications in different areas like spectroscopy, imaging or quantum information. In most case entanglement in just one degree of freedom is selected: for example many experiments in the area of quantum information have been performed using polarization entanglement, eliminating the other degrees of freedom by means of spectral and spatial filtering. However, the most general theory of optical parametric down-conversion must account for the concurrent entanglement in all the degrees of freedom since the quantum-interference pattern in a single parameter can be modified using the other parameters. For example, the polarization interference pattern has been studied as a function of the selected range of transverse wave vectors in literature [16].

Here we use an adaptive optics system to assign a controlled phase to each wave-vector and we study the resulting polarization quantum-interference pattern. This gives us a possible technique to generate quantum states for applications in metrology and quantum information, as well as a technique to study spatial entanglement with bucket detectors (without resorting to the correlations between pixels in an imaging setup). Particularly, the existence of an effect similar to dispersion cancellation in the space of wave-vectors is

predicted. We will focus on type-II SPDC using birefringent phase-matching since the correlations between wave-vectors and spectrum are stronger than employing other phase-matching conditions (as discussed in Chapter 1).

2.1 Theoretical modelling

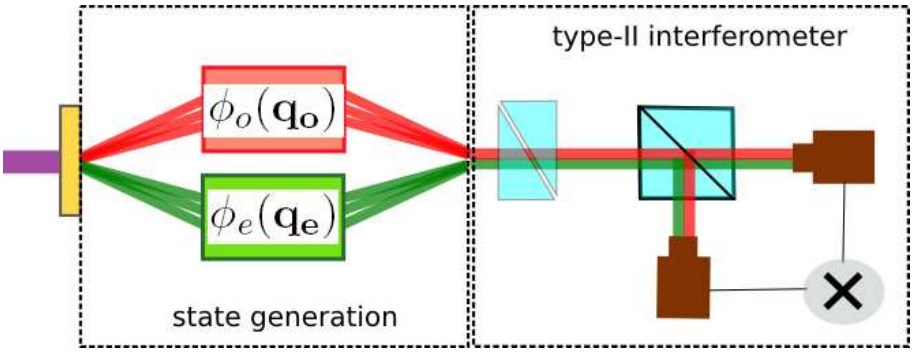

Figure 2.1: Scheme of the proposed setup. Horizontally-polarized photons from type-II SPDC are assigned a phase dependent on the photon transverse momentum $\phi_o(q_o)$, while the vertically-polarized ones are assigned a phase $\phi_e(q_e)$. The modulated photons enter a type-II quantum interferometer, which records the coincidence count rate as a function of the delay τ between the photons given by an appropriate delay-line.

Consider the scheme in Fig. 2.1: a laser beam pumps a $\chi^{(2)}$ nonlinear material designed to obtain type-II parametric down-conversion. The generated photons enter a modulation system which assigns to each wave-vector for the horizontally polarized photon the phase $\phi_o(\mathbf{q_o})$ and for the vertically-polarized photon the phase $\phi_e(\mathbf{q_e})$. This system can be implemented by means of two separate 4f systems and creates an image of the output face of the crystal on the plane B, just with the wavevectors modulated. After this we place the usula type-II quantum interferometer consisting of a birefringent delay line, which delays the horizontally-polarized photon with respect to the vertically-polarized one and a nonpolarizing beamsplitter, followed by two polarizers oriented at 45 degrees to create the superposition of states needed to convert the polarization correlations into polarization entanglement. Finally we place two single-photon detectors with a coincidence circuit. For each delay τ between the horizontally-polarized photon and the vertically-polarized one we record the coincidence rate $C(\tau)$.

2.1.1 State Generation

As we have seen in Section 1.2, using first-order time-dependent perturbation theory the two-photon state at the output of the nonlinear cystal is:

$$|\psi^{(2)}>=\int d\mathbf{q_o}d\mathbf{q_e}d\omega_o d\omega_e \tilde{\Phi}(\mathbf{q_o},\mathbf{q_e},\omega_o,\omega_e)\hat{a}_o^\dagger(\mathbf{q_o},\omega_o)\hat{a}_e^\dagger(\mathbf{q_e},\omega_e)|0> \quad (2.1)$$

where, in the case of monochromatic plane-wave pump at frequency Ω_p:

$$\tilde{\Phi}(\mathbf{q_o},\mathbf{q_e},\omega_o,\omega_e)=\Phi(\mathbf{q_o},\omega_o)\delta(\omega_e-\Omega_p+\omega_o)\delta(\mathbf{q_o}+\mathbf{q_e}) \quad (2.2)$$

In the case of a single bulk crystal of thickness L and constant nonlinearity χ_o the two-photon wavefunction can be written as:

$$|\psi^{(2)}>\sim \chi_o L\int d\mathbf{q}d\nu \quad \mathrm{sinc}\left[\frac{L\Delta(\mathbf{q},\nu)}{2}\right]e^{i\frac{\Delta(\mathbf{q},\nu)L}{2}}\hat{a}_o^\dagger(\mathbf{q},\nu)\hat{a}_e^\dagger(-\mathbf{q},-\nu)|0> \quad (2.3)$$

2.1.2 Propagation

The propagation of the photons between the ouput face of the crystal and the detection planes is described by the optical transfer function H. The probability amplitude of detecting a photon pair the detection planes, with space-time coordinates $(\mathbf{x_A},t_A)$ and $(\mathbf{x_B},t_B)$:

$$A(\mathbf{x_A},\mathbf{x_B};t_A,t_B)=<0|\hat{E}_A^{(+)}(\mathbf{x}_A,t_A)\hat{E}_B^{(+)}(\mathbf{x}_B,t_B)|\psi^{(2)}> \quad (2.4)$$

The quantized electric fields at the detector planes are:

$$\begin{aligned}\hat{E}_A^{(+)}(\mathbf{x}_A,t_A)&=\int d\mathbf{q}d\nu e^{i\omega t_A}[H_{Ae}(\mathbf{x_A},\mathbf{q};\omega)\hat{a}_e(\mathbf{q},\omega)+H_{Ao}(\mathbf{x_A},\mathbf{q};\omega)\hat{a}_o(\mathbf{q},\omega)]\\ \hat{E}_B^{(+)}(\mathbf{x}_B,t_B)&=\int d\mathbf{q}d\nu e^{i\omega t_B}[H_{Be}(\mathbf{x_B},\mathbf{q};\omega)\hat{a}_e(\mathbf{q},\omega)+H_{Bo}(\mathbf{x_B},\mathbf{q};\omega)\hat{a}_o(\mathbf{q},\omega)]\end{aligned} \quad (2.5)$$

where $H_{ij}(\mathbf{q},\omega)$ is the transfer function describing the propagation of the mode with transverse momentum $\mathbf{q}$ and frequency ω and polarization $j=o,e$ to the detection plane $i=A,B$. For the biphoton probability amplitude we get:

$$\begin{aligned}A(\mathbf{x_A},\mathbf{x_B};t_A,t_B)=\int d\mathbf{q_o}d\mathbf{q_e}d\omega_o d\omega_e \Phi(\mathbf{q_o},\mathbf{q_e};\omega_o,\omega_e)\\ \Big[H_{Ae}(\mathbf{x_A},\mathbf{q_e};\omega_e)H_{Bo}(\mathbf{x_B},\mathbf{q_o};\omega_o)e^{-i(\omega_e t_A+\omega_o t_B)}+\\ H_{Ao}(\mathbf{x_A},\mathbf{q_o};\omega_o)H_{Be}(\mathbf{x_B},\mathbf{q_e};\omega_e)e^{-i(\omega_o t_A+\omega_e t_B)}\Big]\end{aligned} \quad (2.6)$$

This probability amplitude represents the coherent superposition of two possible events:

1. the V-polarized photon with momentum $\mathbf{q_e}$ and frequency ω_e going through path A and the H-polarized photon with momentum $\mathbf{q_o}$ and frequency ω_o going through path B

2. the V-polarized photon with momentum $\mathbf{q_e}$ and frequency ω_e going through path B and the H-polarized photon with momentum $\mathbf{q_o}$ and frequency ω_o going through path A

Since the superposition is coherent, interference effects between the two probabilities amplitudes are expected.

State engineering section

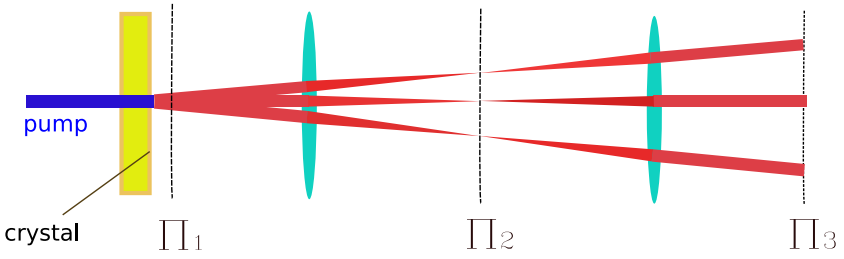

Figure 2.2: Setup for the state generation section. Each transverse momentum $\mathbf{q_i}$ on the output plane of the crystal Π_1 is mapped by the first lens into a point $\mathbf{x_i}$ on the plane Π_2. Here a spatial modulator imparts to the mode a factor $m(\mathbf{x_i}) = \mu(\mathbf{x_i})e^{i\phi(\mathbf{x_i})}$ and it is then remapped into a direction $\mathbf{q_i}$ on the plane Π_3.

The state engineering section consists of two separate 4-f systems, one for the horizontally polarized photon, the other for the vertically polarized one (see Fig. 2.2. Given a transverse momentum $\mathbf{q_i}$ on the output plane of the crystal Π_1, generated in the parametric process, it is mapped by the first lens into a point $\mathbf{x_i}$ on the plane Π_2. Here a spatial modulator imparts to the mode a factor $m(\mathbf{x_i}) = \mu(\mathbf{x_i})e^{i\phi(\mathbf{x_i})}$ and it is then remapped into a direction $\mathbf{q_i}$ on the plane Π_3.
Using Fourier optics calculations, the transfer function between the planes Π_1 and Π_3 can be calculated to be:

$$h_1(\mathbf{x_1}, \mathbf{x_3}) = \int d\mathbf{x} \quad m(\mathbf{x}) \quad e^{-i\frac{k}{f}\mathbf{x}\cdot(\mathbf{x_1}+\mathbf{x_3})} \tag{2.7}$$

The corresponding momentum transfer function is:

$$H_1(\mathbf{q_1}, \mathbf{q_3}) = e^{-i\frac{f}{k}\mathbf{q_1}}\delta(\mathbf{q_1} - \mathbf{q_3}) \tag{2.8}$$

Therefore this optical stage just gives a phase shift $e^{-i\frac{f}{k}\mathbf{q_1}}$ to each transverse momentum $\mathbf{q_1}$ generated by the nonlinear process.

Interferometer

After the plane Π_3 the two photons enter the usual type-II quantum interferometer: they propagate through free space, the birefringent delay-line and a detection aperture $p(\mathbf{x})$ to be finally focused on the detection plane by means of a lens of focal length f_0. Following the derivation in [16] the transfer function is:

$$H_2(\mathbf{x_i}, \mathbf{q}; \omega) = e^{i(\omega/c)(d_1+d_2+f_0)} \exp\left[-i\frac{\omega|\mathbf{x_i}|^2}{2cf}\left(\frac{d_2}{f}-1\right)\right] \\ e^{-i(cd_1/2\omega)|\mathbf{q}|^2}\tilde{P}\left(\frac{\omega}{cf}\mathbf{x_i}-\mathbf{q}\right) \tag{2.9}$$

where $\tilde{P}(\mathbf{q})$ is the Fourier transform of $p(\mathbf{x})$.

2.1.3 Detection

Quantum-interference experiments are usually performed using slow bucket detectors, imparting temporal and spatial integration. Therefore the coincidence count-rate expressed in terms of the biphoton probability amplitude is:

$$C(\tau) = \int d\mathbf{x_A} d\mathbf{x_B} dt_A dt_B |A(\mathbf{x_A}, \mathbf{x_B}; t_A, t_B)|^2 \tag{2.10}$$

Using the expression for the phase mismatch derived in Eq. (1.46) we get $C(\tau) = R_0 + R(\tau)$, with:

$$R_0 = \int d\mathbf{q} d\mathbf{q}' d\nu \Phi^*(\mathbf{q}, \nu)\Phi(\mathbf{q}, \nu) m^*\left(\frac{f}{k}\mathbf{q}\right) m\left(\frac{f}{k}\mathbf{q}'\right) W^{(0)}(\mathbf{q}, \mathbf{q}', \nu) \tag{2.11}$$

$$R(\tau) = \int d\mathbf{q} d\mathbf{q}' d\nu \Phi^*(\mathbf{q}, \nu)\Phi(\mathbf{q}, \nu) m^*\left(\frac{f}{k}\mathbf{q}\right) m\left(\frac{f}{k}\mathbf{q}'\right) W^{(0)}(\mathbf{q}, \mathbf{q}', \nu) \tag{2.12}$$

where

$$W^{(0)}(\mathbf{q}, \mathbf{q}', \nu) = \int d\mathbf{x_A} d\mathbf{x_B} H^*(\mathbf{x_A}, \mathbf{q}, \nu) H^*(\mathbf{x_B}, -\mathbf{q}, -\nu) H(\mathbf{x_A}, \mathbf{q}', \nu) H(\mathbf{x_B}, -\mathbf{q}', -\nu) + \\ H^*(\mathbf{x_A}, -\mathbf{q}, -\nu) H^*(\mathbf{x_B}, \mathbf{q}, \nu) H(\mathbf{x_A}, -\mathbf{q}', -\nu) H(\mathbf{x_B}, \mathbf{q}', \nu) \tag{2.13}$$

$$W(\mathbf{q},\mathbf{q}',\nu)=\int d\mathbf{x_A}d\mathbf{x_B}H^*(\mathbf{x_A},\mathbf{q},\nu)H^*(\mathbf{x_B},-\mathbf{q},-\nu)H(\mathbf{x_A},-\mathbf{q}',\nu)H(\mathbf{x_B},\mathbf{q}',-\nu)+ H^*(\mathbf{x_A},-\mathbf{q},-\nu)H^*(\mathbf{x_B},\mathbf{q},\nu)H(\mathbf{x_A},\mathbf{q}',-\nu)H(\mathbf{x_B},-\mathbf{q}',\nu) \tag{2.14}$$

and

$$\Phi(\mathbf{q},\nu)=\int dz \quad \Pi\left[\frac{z}{L}+\frac{1}{2}\right]e^{-i\Delta(\mathbf{q},\nu)z} \tag{2.15}$$

Performing the integrals over the spatial coordinates:

$$W^{(0)}(\mathbf{q},\mathbf{q}',\nu)=e^{i\frac{2d_1}{k_p}[|\mathbf{q}|^2-|\mathbf{q}'|^2]}\hat{P}_A[(\mathbf{q}-\mathbf{q}')]\hat{P}_B[-(\mathbf{q}-\mathbf{q}')] + \hat{P}_A[-(\mathbf{q}-\mathbf{q}')]\hat{P}_B[(\mathbf{q}-\mathbf{q}')] \tag{2.16}$$

$$W(\mathbf{q},\mathbf{q}',\nu)=e^{i\frac{2d_1}{k_p}[|\mathbf{q}|^2-|\mathbf{q}'|^2]}\hat{P}_A[(\mathbf{q}+\mathbf{q}')]\hat{P}_B[-(\mathbf{q}+\mathbf{q}')]+ \hat{P}_A[-(\mathbf{q}+\mathbf{q}')]\hat{P}_B[(\mathbf{q}+\mathbf{q}')] \tag{2.17}$$

Finally, under the approximation $L \ll d_1$ and using the relation:

$$\Pi[x]\Pi[x-\alpha]=\Pi\left[\frac{z}{\Lambda(\alpha)}-\frac{\alpha}{2\Lambda(\alpha)}\right] \tag{2.18}$$

where $\Lambda(\alpha)=1-|\alpha|$ if $|\alpha|<1$ and $\Lambda(\alpha)=0$ otherwise, one can find the following expressions:

$$C(\tau)=R_0-R(\tau)=R_0[1-V(\tau)] \tag{2.19}$$

where:

$$R_0=\int d\mathbf{q}d\mathbf{q}'\mathrm{sinc}[ML\hat{\mathbf{e}}_\mathbf{2}\cdot(\mathbf{q}-\mathbf{q}')]e^{i\phi(\frac{f}{k}\mathbf{q})}e^{-i\frac{ML}{2}\hat{\mathbf{e}}_\mathbf{2}\cdot(\mathbf{q}-\mathbf{q}')} e^{i\frac{2d_1}{k_p}[|\mathbf{q}|^2-|\mathbf{q}'|^2]}\tilde{P}_A(\mathbf{q}-\mathbf{q}')\tilde{P}_B(-\mathbf{q}+\mathbf{q}') \tag{2.20}$$

and

$$R(\tau)=\Lambda\left(1-\frac{2\tau}{DL}\right)\int d\mathbf{q}d\mathbf{q}'\mathrm{sinc}\left[ML\hat{\mathbf{e}}_\mathbf{2}\cdot(\mathbf{q}+\mathbf{q}')\Lambda\left(1-\frac{2\tau}{DL}\right)\right]e^{i\phi(\frac{f}{k}\mathbf{q})} e^{-i\frac{M}{D}\tau\hat{\mathbf{e}}_\mathbf{2}\cdot(\mathbf{q}-\mathbf{q}')}e^{i\frac{2d_1}{k_p}[|\mathbf{q}|^2-|\mathbf{q}'|^2]}\tilde{P}_A\left[\mathbf{q}+\mathbf{q}'\right]\tilde{P}_A\left[-\left(\mathbf{q}+\mathbf{q}'\right)\right] \tag{2.21}$$

where $\Lambda(\alpha)=1-|\alpha|$ if $|\alpha|<1$ and $\Lambda(\alpha)=0$ otherwise.

2.2 Particular solutions

The equations we have just derived have no easy analytical solutions, and require also much computational power to be solved numeically due to the presence of four nested integrals. However simple solutions can be found in a few interesting special cases.

2.2.1 No phase modulation

If we apply no phase modulation our equations reduce to the ones derived in [16]. Particularly we find:

$$R_0 = \tilde{P}_A(\mathbf{0})\tilde{P}_B(\mathbf{0}) \tag{2.22}$$

and

$$\begin{aligned} R(\tau) = \Lambda\left(1-\frac{2\tau}{DL}\right)\operatorname{sinc}\left[\frac{M^2Lk_p}{2d_1D}\tau\Lambda\left(1-\frac{2\tau}{DL}\right)\right] \\ \tilde{P}_A\left[\frac{Mk_p}{2d_1D}\tau\hat{\mathbf{e}}_\mathbf{2}\right]\tilde{P}_B\left[-\frac{Mk_p}{2d_1D}\tau\hat{\mathbf{e}}_\mathbf{2}\right] \end{aligned} \tag{2.23}$$

If we consider Gaussian apertures of radius R_G centerd along the system's optical axis:

$$p(\mathbf{x}) = e^{-\frac{|\mathbf{x}|^2}{2R_G^2}} \tag{2.24}$$

we can derive a simple mathematical expression for the normalized coincidence rate which can be useful for our physical intuition:

$$V(\tau) = 1 - \Lambda\left(1-\frac{2\tau}{DL}\right)e^{-\frac{\tau^2}{2\tau_1^2}} \tag{2.25}$$

with:

$$\tau_1 = \frac{2d_1D}{k_pMR_G} \tag{2.26}$$

Tipically sharp circular apertures are used in experiments, which have a diffraction pattern described by a first-order Bessel function. However the Gaussian approximation is a good one if the width R_G of the Gaussian is taken to roughly fit the Bessel function (of width R_B): in our case we take $R_G = R_B/(2\sqrt{2})$.
Therefore Eq. (2.25) is still approximately valid in the case of sharp circular apertures, one just needs to take:

$$\tau_1 = \frac{4\sqrt{2}d_1D}{k_pMR_B} \tag{2.27}$$

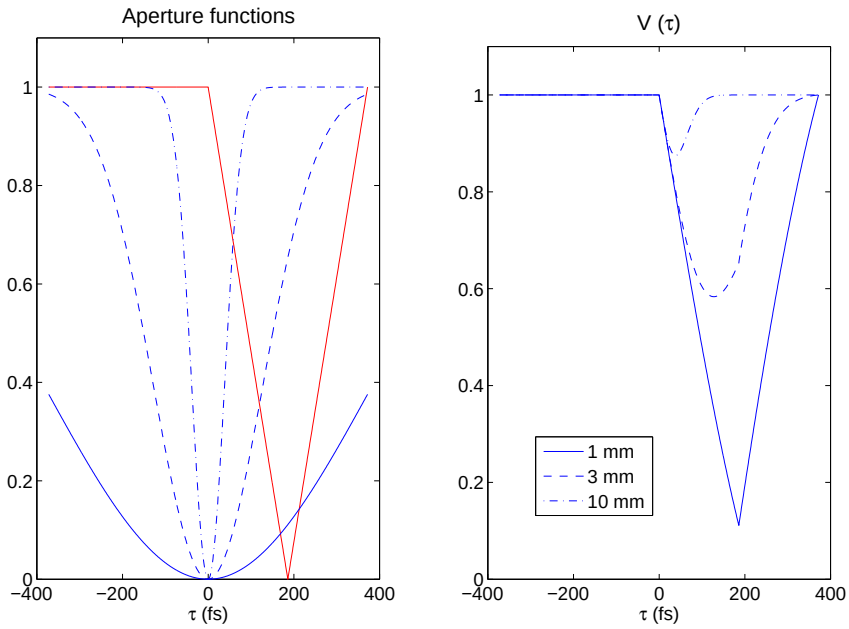

Figure 2.3: On the right side we can see the interference patterns with three different detector aperture sizes: the corresponding aperture functions are shown on the left side.

Mathematically in Eq. (2.25) the interferece pattern is given by the multiplication of a triangular function, centered in $\tau = DL/2$ by a Gaussian function centered in $\tau = 0$. The width of the Gaussian function τ_1 decreases with increasing radius of the aperture R_B. Therefore, in the small aperture approximation, the width of the Gaussian is so large that it is approximately constant between $\tau = 0$ and $\tau = DL/2$, giving the typical tringular dip found in quantum interference experiments. On the other hand, increasing the aperture size, the width of the Gaussian function decreases, reducing the dip visibility (see Fig. 2.3).
Physically this can be explained by the fact that increasing the aperture size we let more wave-vectors into the system and, due to spatial walk-off in type-II interferometry we introduce distinguishability, reducing the interference visibility.

2.2.2 Linear phase shift

If we introduce a simple tilt of the mirror:

$$\phi(\mathbf{x}) = \alpha \cdot \mathbf{x} \tag{2.28}$$

we get:

$$V(\tau) = \frac{1}{\tilde{P}_A(\mathbf{0})\tilde{P}_A(\mathbf{0})}\Lambda\Big(1-\frac{2\tau}{DL}\Big)\mathrm{sinc}\Big[\frac{MLk_p}{2d_1}\left(\frac{M}{D}\tau + 2f\alpha\cdot\hat{\mathbf{e}}_\mathbf{2}\right)\Big] \\ \hat{P}_A\left[\frac{k_p}{2d_1}\left(\frac{M}{D}\tau\hat{\mathbf{e}}_\mathbf{2}+2f\alpha\right)\right]\hat{P}_B\left[-\frac{k_p}{2d_1}\left(\frac{M}{D}\tau\hat{\mathbf{e}}_\mathbf{2}+2f\alpha\right)\right] \tag{2.29}$$

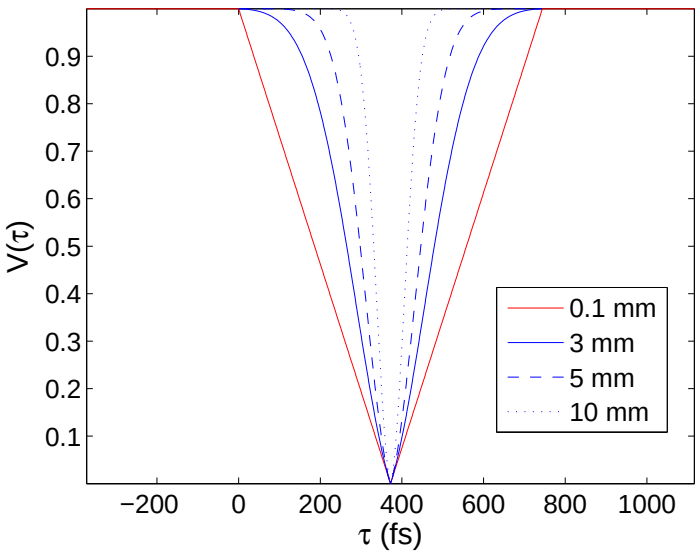

Figure 2.4: Quantum interference pattern for different detector aperture sizes, introducing a linear modulation of the deformable mirror, in order to restore the indistinguishability between the photons, decreased by the spatial walkoff in the generation process.

If we compare Eq. (2.29) with Eq. (2.25) we can see that the structure is the same, we again have a trinagular function centered in $\tau = DL/2$ and two aperture functions. But this time the aperture functions, instead of being centered in $\tau = 0$, can be shifted at will along the τ axis. So, if we open the apertures, the aperture functions became narrower, but if we shift them to the center of the tringular dip we can still keep the visibility high.
Physically what we do is to compensate for the spatial walk-off and to restore indistinguishability between the photons.

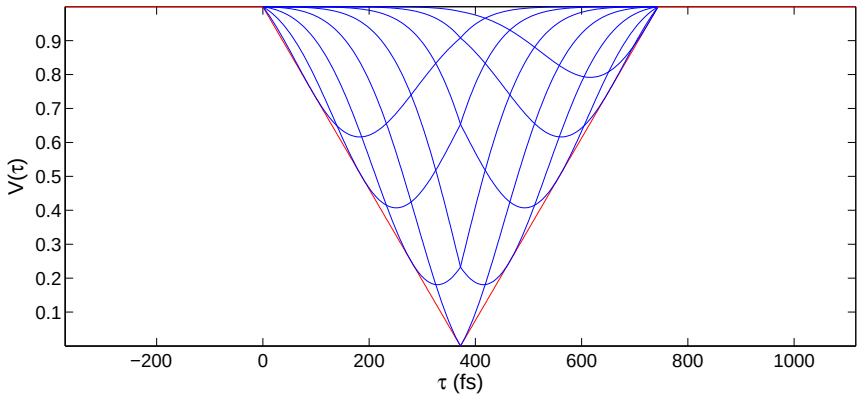

Figure 2.5: Quantum interference patterns for different linear modulations. Increasing the linear modulation the dip increases, reaching the maximum when $\tau_0 = DL/2$, to decrease afterwards. Note that the center of the dip shifts within the range $\tau = [0, DL]$

2.2.3 Large aperture approximation

If the detection apertures are large enough for the $\tilde{P}_i$ function to be successfully approximated by a delta-function we get:

$$V(\tau) = \Lambda \left(1 - \frac{2\tau}{DL}\right) \int d\mathbf{q} \quad m^*(\mathbf{q}) m(-\mathbf{q}) \quad e^{i\frac{2Mk}{fD}\tau \hat{\mathbf{e}}_2 \cdot \mathbf{q}} \tag{2.30}$$

Suppose that the spatial modulator is a circular aperture with radius r:

$$\begin{aligned} m(\mathbf{x}) &= 0 \qquad && \text{if } |\mathbf{x}| > r \\ m(\mathbf{x}) &= e^{i\phi(\mathbf{x})} \qquad && \text{if } |\mathbf{x}| < r \end{aligned} \tag{2.31}$$

In this case the function $\phi(\mathbf{x})$ can be expanded on a set of polynomials which are orthogonal on the unit circle, like the Zernicke polynomials:

$$\phi(\mathbf{q}) = \sum_n \phi_{nm} \sum_m R_n^m(\rho) \cos(m\theta) \qquad m = -n, -n+2, -n+4, ..., n \tag{2.32}$$

where $\mathbf{q} = (\rho\cos\theta, \rho\sin\theta)$. To calculate $\phi(-\mathbf{q})$ we note that $-\mathbf{q} = [\rho\cos(\theta + \pi), \rho\sin(\theta + \pi)]$, so:

$$\phi(-\mathbf{q}) = \sum_n \sum_m R_n^m(\rho) \cos[m(\theta + \pi)] \tag{2.33}$$

If m is even then $\cos[m(\theta+\pi)] = \cos(m\theta)$, otherwise if m is odd $\cos[m(\theta+\pi)] = -\cos(m\theta)$. Therefore:

$$\begin{aligned}\phi(\mathbf{q}) - \phi(-\mathbf{q}) &= \sum_n \Big[\sum_{meven} \phi_{nm} R_n^m(\rho)\cos(m\theta) + \sum_{meven} \phi_{nm} R_n^m(\rho)\cos(m\theta)\Big] \\ &\quad - \sum_n \Big[\sum_{meven} \phi_{nm} R_n^m(\rho)\cos(m\theta) - \sum_{meven} \phi_{nm} R_n^m(\rho)\cos(m\theta)\Big] \\ &= 2\sum_n \sum_{modd} \phi_{nm} R_n^m(\rho)\cos(m\theta)\end{aligned} \tag{2.34}$$

So, only the Zernike polynomials with m odd contribute to the shape of the interference pattern. This effect is the spatial counterpart of the dispersion cancellation effect, in which only the odd-order terms in the Taylor expansion of the spectral phase survive.

2.3 Numerical solutions

We propose the following as a fast and accurate way of solving Eq. (**??**) and Eq. (**??**), valid in the case where the function $m(\mathbf{x})$ changes smoothly over the mirror surface, as it is the case in experimentally relevant situations.

Following the procedure illustrated in Fig. (2.6) the mirror surface can be divided in small squares (side d). The square (l, m) is identified by:

$$\sigma_{l,m}(x,y) = \Pi\left[\frac{x}{d} + l\right] \Pi\left[\frac{y}{d} + m\right] \tag{2.35}$$

selecting the area:

$$\begin{aligned}\left(l - \frac{1}{2}\right) d < x < \left(l + \frac{1}{2}\right) d \\ \left(m - \frac{1}{2}\right) d < y < \left(m + \frac{1}{2}\right) d\end{aligned} \tag{2.36}$$

We approximate the value of the phase in each square as the mean value of the real phase within the square:

$$\phi(x,y) = \phi_{lm} \qquad \phi_{lm} = \frac{1}{d^2}\int dxdy\phi(x,y)\Pi\left[\frac{x}{d} + l\right] \Pi\left[\frac{y}{d} + m\right] \tag{2.37}$$

that is:

$$e^{i\phi(x,y)} \approx \sum_{l,m} e^{i\phi_{l,m}\Pi\left[\frac{x}{d}+l\right]\Pi\left[\frac{y}{d}+m\right]} \tag{2.38}$$

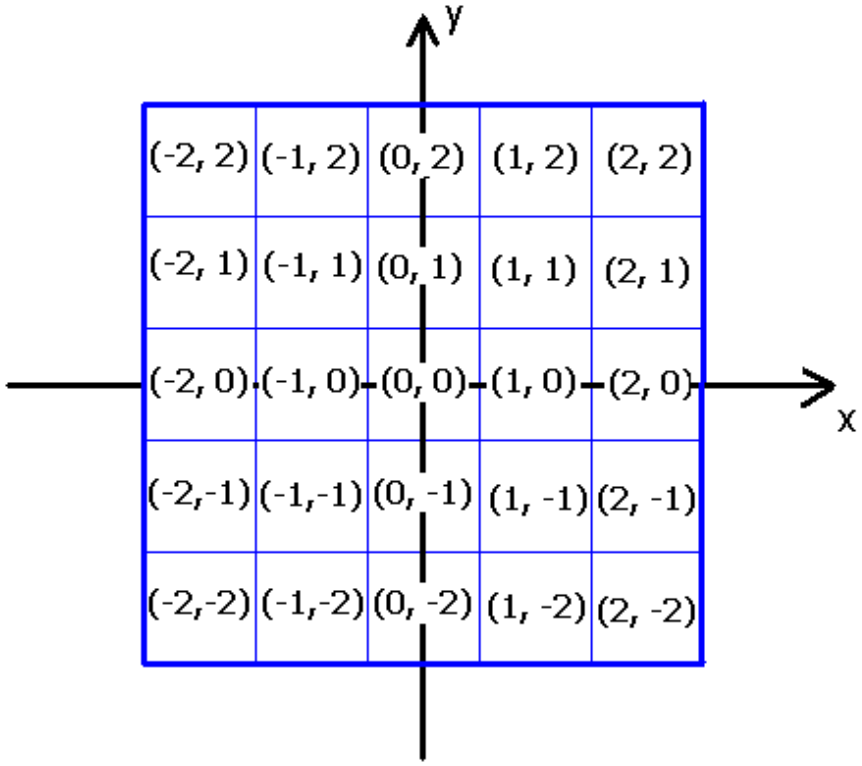

Figure 2.6: Mirror segmentation and labelling of the squares

In this case (see the next paragraph for the derivation):

$$\sum_{l,m} e^{i\phi_{l,m}\Pi\left[\frac{x}{d}+l\right]\Pi\left[\frac{y}{d}+m\right]} = \sum_{l,m} e^{i\phi_{l,m}}\Pi\left[\frac{x}{d}+l\right]\Pi\left[\frac{y}{d}+m\right] \tag{2.39}$$

Substituting this expression in Eq. 2.21, and collecting the integrations one finds:

$$R(\tau) \approx \sum_{l,m}\sum_{\lambda,\mu} e^{-i\phi_{lm}-\phi_{\lambda,\mu}}\alpha_{l\lambda}I_{m\mu}(\tau) \tag{2.40}$$

where:

$$\alpha_{l\lambda} = \int dq_x \int d'_{qx}\Pi\left[\frac{f}{kd}q_x - l\right]\left[\frac{f}{kd}q'_x - \lambda\right] \underset{e^{j\frac{2d_1}{k_p}(q_x^2-{q'_x}^2)P[q_x+q'_x]P[-(q_x+q'_x)]}}{} \tag{2.41}$$

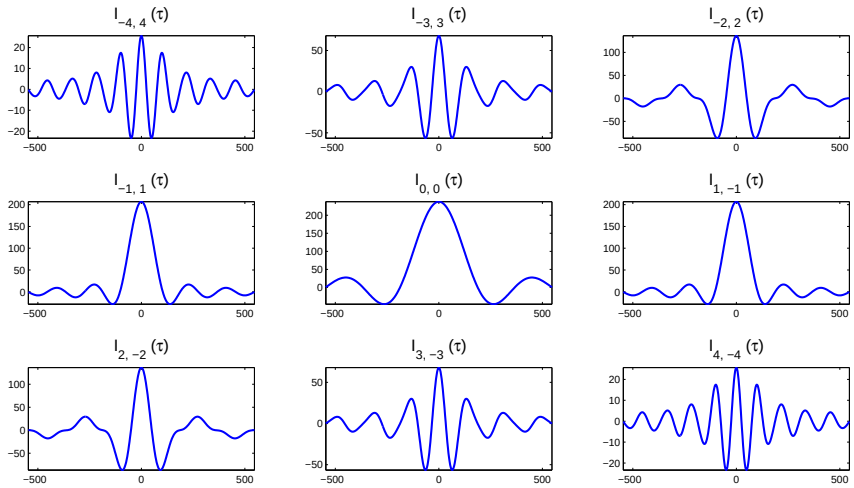

Figure 2.7: Plot of the non-zero $I_{m,\mu}(\tau)$ functions for a 9-by-9 mirror segmantation. For a 10 mm collection aperture (at 1 m distance from the crystal) the functions $I_{m,\mu}(\tau)$ are non-zero only for $\mu = -m$, originating even-order aberration cancellation.

and

$$Im,\mu(\tau) = \int dq_y \int dq'_y \Pi\left[\frac{f}{kd}q_y - m\right]\left[\frac{f}{kd}q'_y - \mu\right] e^{j\frac{2d_1}{k_p}(q_y^2 - q'^2_y)} e^{-j\frac{M}{D}\tau(q_y - q'_y)} \\ \text{Sinc}\left[ML(q_y + q'_y)\Lambda\left(1 - \frac{2\tau}{DL}\right)\right] P[q_y + q'_y]P[-(q_y + q'_y)] \tag{2.42}$$

Performing the integrations one gets:

$$\alpha_{l\lambda} = \int dx \tilde{P}(x)\Lambda\left[\frac{fx}{kd} - (l+\lambda)\right] \\ \text{sinc}\left\{\frac{2dd_1}{f}x\Lambda\left[\frac{fx}{kd} - (l+\lambda)\right]\right\} e^{i\frac{dd_1}{f}(l-\lambda)x} \tag{2.43}$$

and

$$I_{m\mu}(\tau) = \int dx \tilde{P}(x)\Lambda\left[\frac{fx}{kd} - (m+\mu)\right] \text{sinc}\left\{MLx\Lambda\left[1 - \frac{2\tau}{DL}\right]\right\} \\ \text{sinc}\left\{\frac{2kd}{f}\left(\frac{2d_1}{k_p}x - \frac{M}{D}\tau\right)\Lambda\left[\frac{fx}{kd} - (m+\mu)\right]\right\} e^{i\frac{kd}{f}\left(\frac{2d_1}{k_p}x - \frac{M}{D}\tau\right)(m-\mu)} \tag{2.44}$$

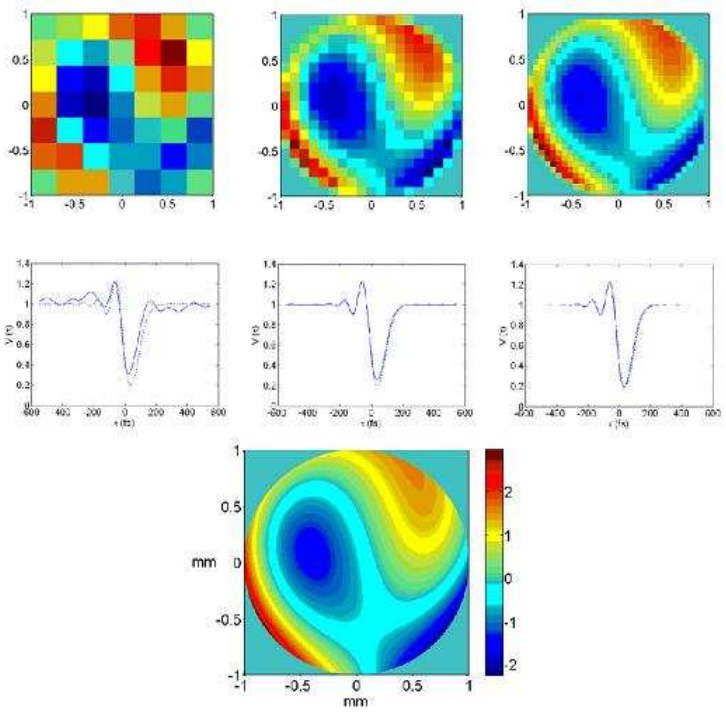

Figure 2.8: Comparison between the results obtained sectioning the mirror into a different number of squares (respectively 7-by-7, 19-by-19 and 31-by-31. Increasing the number of squares the accuracy obviously increases: already in the 31by31 case the approximate interference pattern is indistinguishable from the real one.

A similar expression can be found for the background coincidence rate:

$$R_0 \approx \sum_{l,m} \sum_{\lambda,\mu} e^{-i(\phi_{lm}-\phi_{\lambda,\mu})} R_{l\lambda}^{(x)} R_{m\mu}^{(y)} \tag{2.45}$$

where:

$$\begin{aligned} R_{l\lambda}^{(x)} = \int dx \tilde{P}(x) \Lambda \left[\frac{fx}{kd} - (l-\lambda) \right] \\ \operatorname{sinc} \left\{ \frac{2dd_1}{f} x \Lambda \left[\frac{fx}{kd} - (l-\lambda) \right] \right\} e^{i\frac{dd_1}{f}(l+\lambda)x} \end{aligned} \tag{2.46}$$

and

$$\begin{aligned} R_{m\mu}^{(y)} = \int dx \tilde{P}(x) \Lambda \left[\frac{fx}{kd} - (m-\mu) \right] \operatorname{sinc}(MLx) \\ \operatorname{sinc} \left\{ \frac{2dd_1}{f} x \Lambda \left[\frac{fx}{kd} - (m-\mu) \right] \right\} e^{i\left[\frac{dd_1}{f}(m+\mu) - \frac{ML}{2}\right]x} \end{aligned} \tag{2.47}$$

In the limit of large detector apertures $\tilde{P}(x) \approx \delta(x)$:

$$\alpha_{l\lambda} = \delta(l + \lambda) \tag{2.48}$$

$$I_{m\mu} = \text{sinc}\left[\frac{2kdM}{fD}\tau\right] e^{-i\frac{2kdM}{fD}m\tau}\delta(m + \mu) \tag{2.49}$$

So:

$$R_{BIG}(\tau) \approx \sum_{l,m} e^{-i(\phi_{lm}-\phi_{-l,-m})}\alpha_{l,-l}I_{m,-m}(\tau) \tag{2.50}$$

We have a discrete formulation of the even-order spatial phase cancellation effect. The even-parity components of the phase function are such that their value on the square (l, m) is equal to their value on the square (-l, -m) so that $\phi_{lm} - \phi_{-l,-m} = 0$ and they do not contribute to the coincidentce pattern. This way our approximate solution technique is consistent with the general theory.

Derivation of Eq. (2.39)

Suppose to have a set A, which can be divided into a set of disjoint subsets $A_k, k = 1, 2, ...$:

$$\sum_k A_k = A \qquad A_k \cap A_l = \delta_{kl}A_k \tag{2.51}$$

To each set we can associate a function: such that:

$$\sum_k \chi_k(x) = \chi_A \qquad \chi_k(x)\chi_l(x) = \delta_{kl}\chi_k(x) \tag{2.52}$$

So, if we want to calculate:

$$\begin{aligned} e^{i\sum_k \phi_k\chi_k(x)} &= \prod_k e^{i\phi_k\chi_k(x)} \\ &= \prod_k \left[1 \cdot (1 - \chi_k(x)) + e^{i\phi_k} \cdot \chi_k(x)\right] \\ &= \prod_k \left[1 + (e^{i\phi_k} - 1)\chi_k\right] \end{aligned} \tag{2.53}$$

If we express the first few terms we get:

$$\begin{aligned} \prod_k \left[1 + (e^{i\phi_k} - 1)\chi_k\right] &= \left[1 + (e^{i\phi_1} - 1)\chi_1\right]\left[1 + (e^{i\phi_2} - 1)\chi_2\right]\left[1 + (e^{i\phi_3} - 1)\chi_3\right]... \\ &= 1 + (e^{i\phi_1} - 1)\chi_1 + (e^{i\phi_2} - 1)\chi_2 + ... \\ &\quad + (e^{i\phi_1} - 1)(e^{i\phi_2} - 1)\chi_1\chi_2 + (e^{i\phi_1} - 1)(e^{i\phi_3} - 1)\chi_1\chi_3 + ... \\ &\quad + (e^{i\phi_1} - 1)(e^{i\phi_1} - 1)(e^{i\phi_1} - 1)\chi_1\chi_2\chi_3 \\ &\quad\quad + (e^{i\phi_1} - 1)(e^{i\phi_2} - 1)(e^{i\phi_4} - 1)\chi_1\chi_2\chi_4 + ... \end{aligned} \tag{2.54}$$

So that in the end:

$$\begin{aligned} e^{i\sum_k \phi_k \chi_k(x)} &= 1 + \sum_k \left[\left(e^{i\phi_k} - 1 \right) \chi_k \right] \\ &= 1 + \sum_k e^{i\phi_k} \chi_k - \sum_k \chi_k \\ &= \sum_k e^{i\phi_k} \chi_k \end{aligned} \tag{2.55}$$

Since the squares sets we used to for our porpouses satisfy Eq. (B1) then the result expressed in Eq. (B5) is valid for our case.

2.4 Experiments

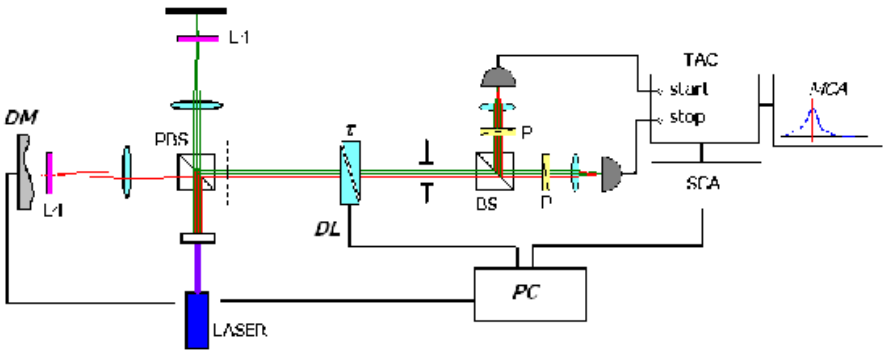

Figure 2.9: Experimental configuration. The photons generated by type-II downconversion enter two separate 4-f systems, one comprising a deformable mirror, getting a relative phase dependent on the emission wave-vector. The photons are then recombined and enter a type-II quantum interferometer. Coincidence events are detected as a function of the temporal delay between the photons.

The experimental configuration adopted is shown in Fig. 2.9. A blue laser diode with single longitudinal-mode selection (10 mW power) is used to pump a 1.5 mm long BBO crystal cut for type-II phase matching. A polarizing beam-splitter transmits the horizontally-polarized photon and reflects the vertically-polarized one. From the output surface of the crystal the V-polarized photon travels a distance f = 20 cm to the lens (focal length f), then again a distance f to the deformable mirror, passing through a quarter wave plate oriented at 45 degrees. After reflection it travels the way back, but, passing twice through the QWP, it becomes horizontally polarized, being then transmitted by the

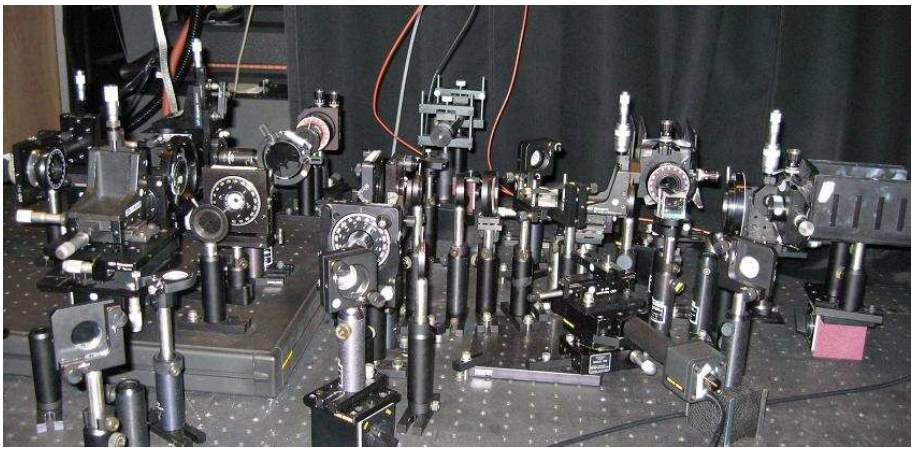

Figure 2.10: Picture of the whole experimental configuration.

beamsplitter. A similar path is described by the originally horizontally polarized photon, it only goes to a flat mirror instead of going to the deformable one. This way we created two separate 4-f systems for the photons, one of which comprises a spatial modulation effect.

After exiting the modulation stage the two photons pass through a birefringent delay-line and then through a non polarizing beamsplitter, from which the downconverted beam is split into two different paths. In each path we placed a polarizer oriented at 45 degrees and a collection lens, which focused the light into the detectors. To maximize the amount of collected wavevectors we chosed not to use the usual fiber-coupled detectors, but to use open face ones. No spectral filters were used and the coincidence detection was performed using a 3 ns integration window.

2.4.1 The deformable mirror

The mirror, completely developed in the CNR-INFM LUXOR laboratory, is a thin nitrocellulose membrane aluminium coated deformable by 37 electrodes as depicted in Fig. 2.12. It is deformed by electrostatic force created applying a high voltage drop between the electrodes.

The membrane is $5\mu m$ thick, its initial flatness is less than 60 nm rms. Pulling all the electrodes at the maximum voltages of 230V, the distance from the central point of the deflected surface to the plano is about $10\mu m$ as depicted in the interferogram. This deformation is a paraboloid that corresponds to a focal length of about 2m. Fig. 2.13 shows the interferograms, taken by a

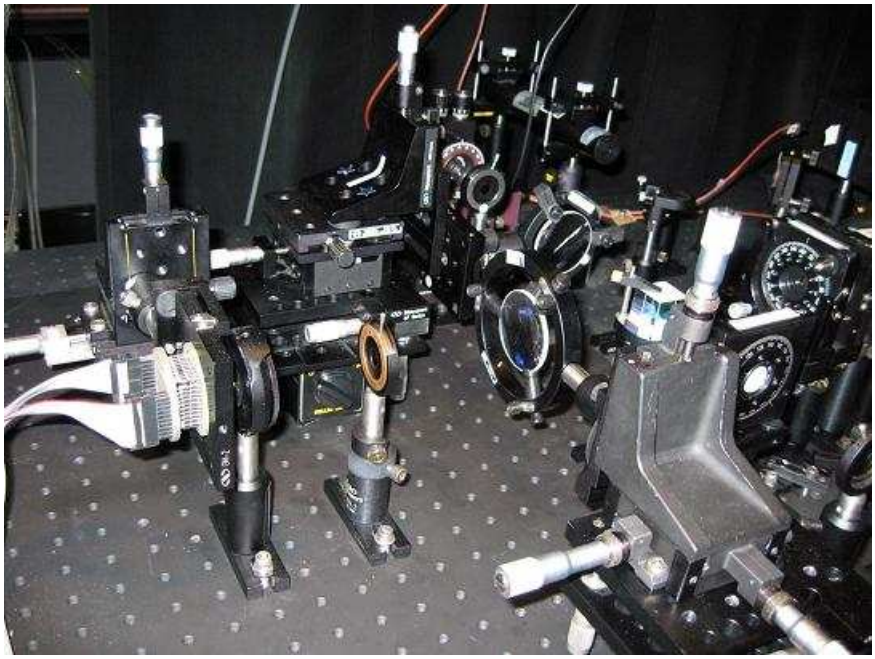

Figure 2.11: Picture of the modulation part

Zygo interferometer, of the flat surface and of the mirror pulled by the half of maximum voltage (115V).

The mirror is controlled by a MATLAB program, which solves the Poisson equation and selects the relative values for the actuator tension (a 8 bit digital value). This digital value is converted to an analog voltage level, successively amplified by a set of high voltage DC amplifiers to drive the actuators.

2.4.2 The birefringent delay-line

In a type-II quantum interferometry experiment one should give a delay between the H-polarized photon and the V-polarized photon. The most stable way of doing this is to use a pair of sliding wedges of a birefringent material, for example quartz.
The setup is illustrated in Fig. 2.14: a quartz wedge is kept fixed and the other one is mounted on a sliding stage. A slab of birefringent material, mounted on a rotating stage is used to select the zero-path position. The sliding stage is controlled by a Nanomover motorized actuator (by Melles Griot), controlled by the computer via GPIB.

Alignment of the quartz wedges was made looking at the interference of a HeNe laser beam by the surfaces of the wedges: if the surfaces were exactly

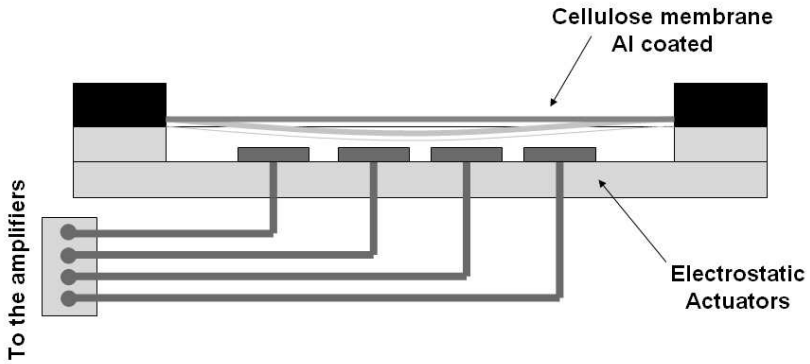

Figure 2.12: Adaptive mirror scheme.

plabe the fringes would disappear. One should also check that sliding the moving wedge the interference pattern would not change.

2.4.3 Single photon detectors

Our experimental configuration, in which a large angular acceptance was needed, urged us to use open-face detectors. The choice was between photomultipliers, which could provide sensitive areas as large as a few mm, but with very low quantum efficiency at 820 nm (few percents) and open-face avalance photodiodes (with smaller sensitive area, but much higher quantum efficiency, up to 60%). Due to the low pump power at our disposal, a very low number of coincidences per second could be detected with photomultipliers (few tens with open apertures) making it impossible to perform the experiment. So silicon APD were chosen.

Particularly we used SPCM-AQ model from EGG, which has nearly 50% quantum efficiency at 820 nm and a sensitive area of around $180\mu m$. Such devices are actively quenched, and can get to counting speeds up to 10 millions counts per second. The dead time between pulses is 30 ns and single photon arrival can be measured with an accuracy of 300 ps FWHM. Each module has its own integrated high-voltage supply and output pulse shaping circuitry, providing with output TTL pulses.

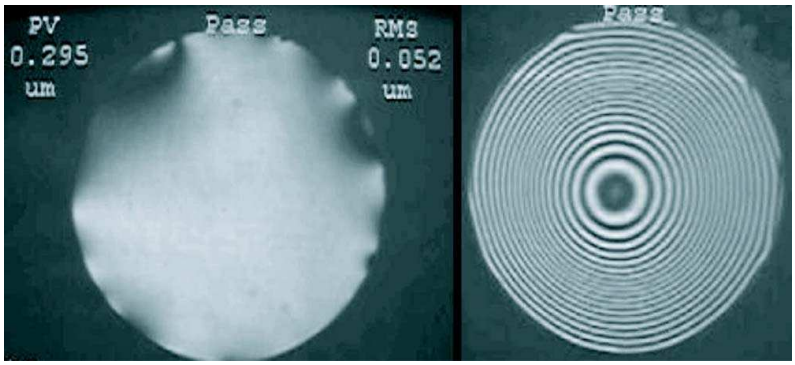

Figure 2.13: Interferograms of the mirror: a) flat position; b) pulled each electrodes by half driving voltage (115V).

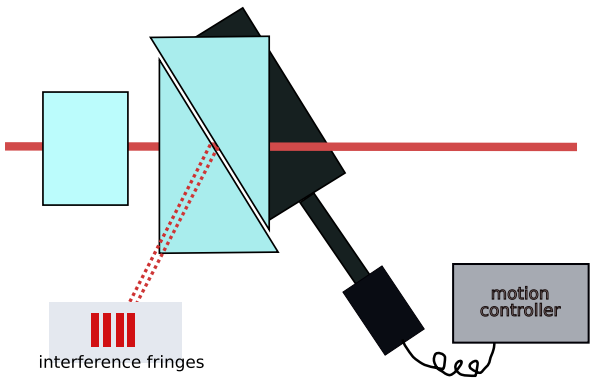

Figure 2.14: Scheme for the birefringent delay line.

2.4.4 The coincidence detection circuit

Once a photon is detected, each detector gives in output a TTL pulse, which is split in two cables: one goes to the single event counter, the other to the Time-to-Amplitude Converter (TAC), see Fig. 2.18. This device takes in input a Start signal (from the detector connected with the shorter cable) and a Stop signal (from the detector with a longer cable). Every time it gets a Start followed by a stop, it gives in output a pulse whose heigth is proportional to the temporal difference between the Start and the Stop.

Now, as a first step one can feed this signal to a MultiChannel Analyzer (MCA), which takes a set of pulses and makes a histogram of the heights. This way one can see the distribution of the time differences between the clicks of

Figure 2.15: Picture of the birefringent delay line.

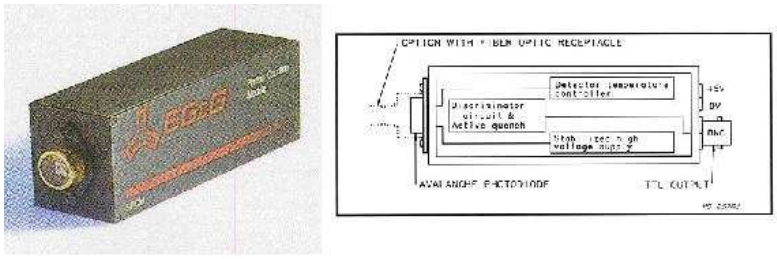

Figure 2.16: EG&G silicon avalanche photodiode SPCM-AQ.

the two detectors. The presence of a clear peak at the pulse height corresponding to time τ_0 indicates that there are many events with a given time difference τ_0, as it is the case of the detection of photon pairs generated at the same time, but then electrically delayed by means of different cable length. We found a clear peak in the MCA scan, whose width was about 1 ns.
Then the output of the TAC can be fed into the Single Channel Analyzers (SCA), which gives a click only in the presence of pulses whose height is in selected range around a certain value. Of course, if one sets the height corresponding to τ_0 as the central value and sets the window to contain all the events in the peak, one selects only the coincidence events. The output of the SCA is connected to a counter, whose count rate is acquired by a computer by means of a GPIB connection. All electronics was placed in a standard NIM

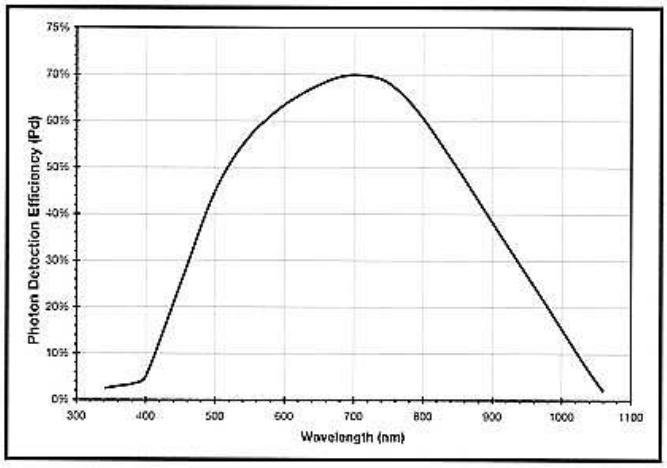

Figure 2.17: Quantum efficiency of our APDs vs wavelength. At 820 nm we could get nearly 0.5 quantum efficiency

crate: specifically an ORTEC 567 TCA/SCA, together with an Ortec 994 CC-NIM Quad 100-MHz Counter and a Canberra MultiChannel Analyzer were employed.

2.4.5 Experiment control

The electronics was set up to make the experiment run automatically. The software to control the deformable mirror and perform the interferometer scan was written in MATLAB. Particularly all the devices in the interferometer were controlled via GPIB, using a National Instrument USB-GPIB device. In each step the sliding wedge position was set and the number of single and coincidence counts was acquired. The counting integration time for each scan could be set via software by the experimenter.

2.5 Experimental results

Experimental results for linear spatial phase, obtained with a mirror tilt are shown in Fig. 2.19 and Fig. 2.20. Experiments were conducted with 15 mm apertures, 50 cm distant from the crystal image plane, giving a collection angle of approximately 30 mrad.
In Fig. 2.19 one can see the evolution of the interference pattern with different value of mirror tilt. As predicted in Section 2.2.2, the dip is shifted and its

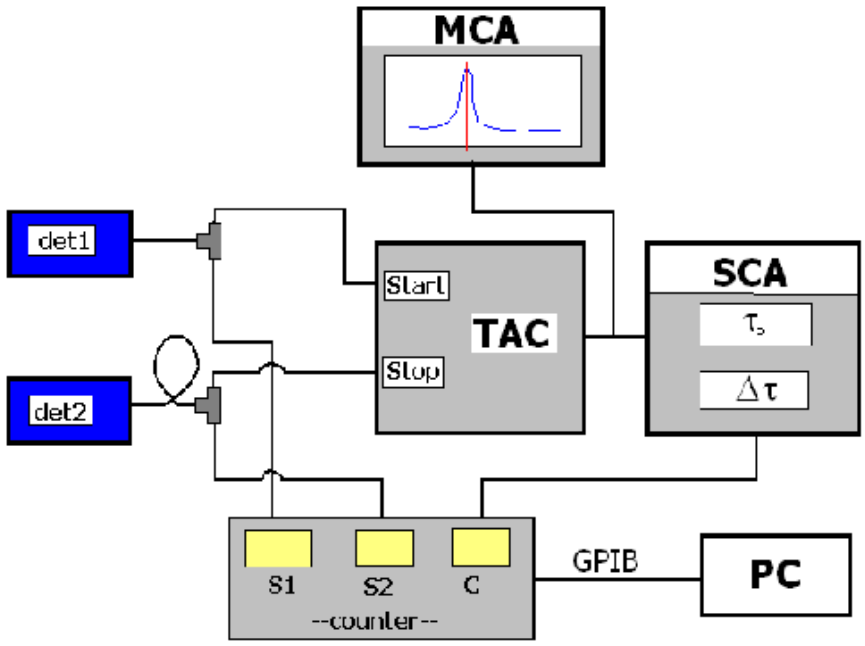

Figure 2.18: Coincidence detection apparatus (TAC = Time-to-Amplitude Converter, MCA = MultiChannel Analyzer, SCA = Single Channel Analyzer).

visibility changes, getting the maximum value when the spatial walk-off is completely compensated for.

2.6 Conclusions

In this Chapter we studied multiparameter entanged states produced by spontaneous parametric downconversion, proposing a technique to manipulate the emission wavevectors of the photons and studying the effects on the temporal and polarization interference pattern. The major results we obtained were:

- the development of a model for the phaenomenon, together with a numerical solution technique
- in type-II quantum interferometry, incresing the collection angular acceptance (to increase intensity and bandwidth) the interference pattern visibility decreases due to spatial walk-off. We demonstrated the possibility to restore high visibility even with large detection apertures.

- we suggested the existence of a spatial counterpart of spectral dispersion cancellation and studied it with numerical simulations.

All the work presented in this Chapter, comprising experiment design, theoretical analysis, numerical modelling and experimental development were performed by the PhD candidate during his visit to Quantum Imaging Laboratory (Boston University).

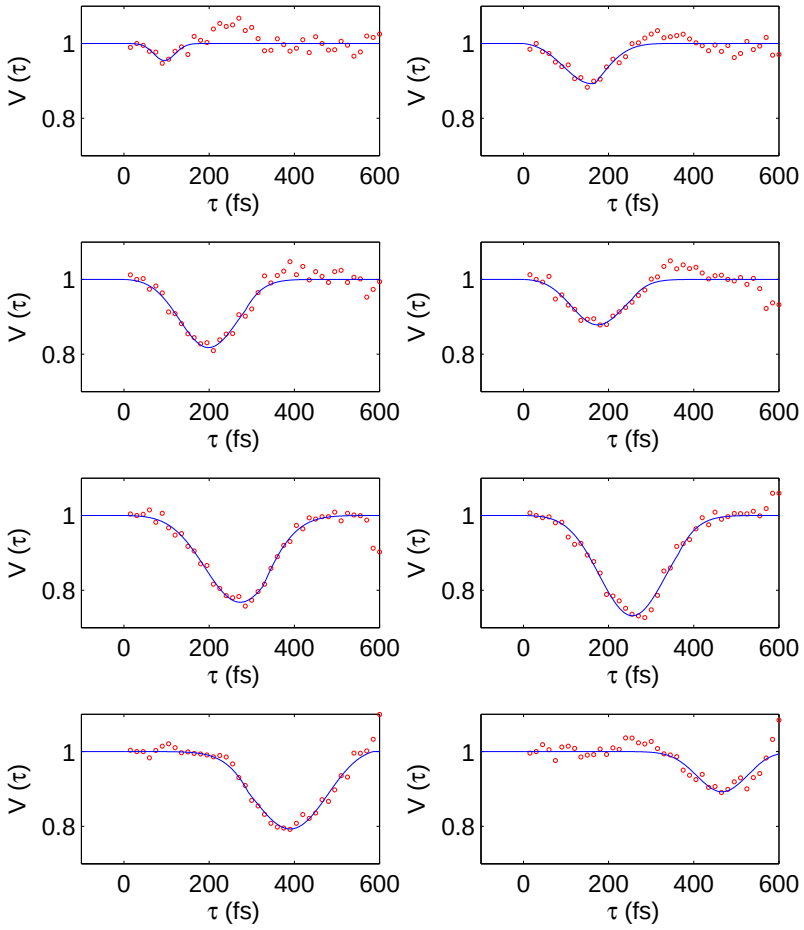

Figure 2.19: Experimental result for dfferent tilting angle of te mirror. The experimental results clearly reproduce the simulated data shown in Fig. 2.4, with the interference patern first increasing and then decreasing its visibility.

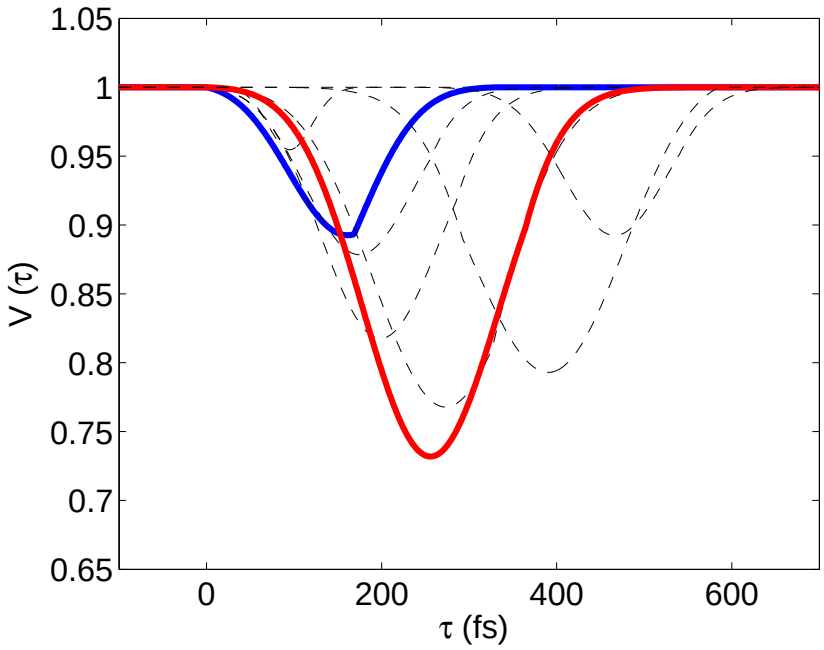

Figure 2.20: Comparison between the data shown in Fig. 2.19, showing a clear imprvement in dip visibility using a tilt of the deformable mirror

Chapter 3

Two-photon spectral coherence matrix

The detailed characterization of quantum optical states is important both in fundamental studies of quantum mechanics and in practical quantum information and quantum measurement applications. The polarization state tomography technique, leading to polarization density matrix reconstruction, has been developed by Kwiat and co-workers in order to provide quantitative characterization of polarization entanglement created in the SPDC [17]. The conventional Stokes parameters formalism of polarization optics has also been extended to cover the domain of two-photon polarization entangled states [18]. In the field of ellipsometry, the reconstruction of the polarization state of light, after reflection from a material, can provide an information about the surface geometry and the chemical composition of the system under investigation. A quantum analog of ellipsometry that makes use of polarization-entangled states has been developed recently [19, 20] that provides higher measurement accuracy in the low-power regime [21]. In quantum ellipsometry the retrieval of the two-photon polarization density matrix by using polarization state tomography can provide more accurate characterization of the sample properties even when the source emits polarization entangled light in a mixed state [22].

However, monochromatic (single-frequency) ellipsometry cannot provide enough information to completely characterize the sample in many challenging applications. This becomes particularly clear when dealing with complex surface geometries, or with layers of materials that have similar refractive indices at the particular probing wavelength. To address this problem, a technique known as spectroscopic ellipsometry has been developed based on polarization properties of spectrally broadband light. Classical spectroscopic ellipsometry

is currently used in several areas of nanotechnological metrology.

Traditionally, the polarization state of broadband light has been described in terms of the spectral coherence matrix and spectral Stokes parameters [23, 24]. In this Letter we introduce the two-photon spectral coherence matrix and the spectral two-photon Stokes parameters along with procedures for evaluating their components in experiment. These tools will be crucial for characterizing multi-parameter entanglement and for developing a quantum version of spectroscopic ellipsometry that is built around spectral and polarization entanglement.

In this Chapter we first briefly review the concepts of spectral coherence matrix and spectral Stokes parameters in classical optics. We then introduce a two-photon spectral coherence matrix and spectral two-photon Stokes parameters for entangled-photon states. In conclusion we outline experimental procedures for evaluation of matrix elements and discuss several special cases.

3.1 Classical Coherence Matrix

Classical partially polarized light can be described by the coherence matrix [25]:

$$J(\tau) = \begin{bmatrix} < E_x^*(t)E_x(t+\tau) > & < E_x^*(t)E_y(t+\tau) > \\ < E_y^*(t)E_x(t+\tau) > & < E_y^*(t)E_y(t+\tau) > \end{bmatrix} \tag{3.1}$$

or by the spectral coherence matrix [26, 27, 28]:

$$R(\omega) = \begin{bmatrix} R_{xx}(\omega) & R_{xy}(\omega) \\ R_{yx}(\omega) & R_{yy}(\omega) \end{bmatrix} \tag{3.2}$$

where:

$$R_{ij}(\omega) = \int_{-\infty}^{+\infty} J_{ij}(\tau) e^{j\omega\tau} d\tau \tag{3.3}$$

Since the spectral coherence matrix is Hermitian we can express it in terms of Pauli matrices σ_i:

$$\sigma_0 = \begin{bmatrix} 1 & 0 \\ 0 & 1 \end{bmatrix} \qquad \sigma_1 = \begin{bmatrix} 1 & 0 \\ 0 & -1 \end{bmatrix} \qquad \sigma_2 = \begin{bmatrix} 0 & 1 \\ 1 & 0 \end{bmatrix} \qquad \sigma_3 = \begin{bmatrix} 0 & i \\ -i & 0 \end{bmatrix} \tag{3.4}$$

so that:

$$R(\omega) = \frac{1}{2} \sum_{i=0}^{3} S_i(\omega)\sigma_i \tag{3.5}$$

where the $S_j(\omega)$ are called the spectral Stokes parameters:

$$S_j(\omega) = \mathrm{Tr}[\sigma_j R(\omega)] \tag{3.6}$$

The spectral coherence matrix can be written as:

$$R(\omega) = \frac{1}{2}\begin{bmatrix} S_0(\omega) + S_1(\omega) & S_2(\omega) + iS_3(\omega) \\ S_2(\omega) - iS_3(\omega) & S_0(\omega) - S_1(\omega) \end{bmatrix} \tag{3.7}$$

The trace of the spectral coherence matrix equals the spectral intensity:

$$\mathrm{Tr}[R(\omega)] = R_{xx}(\omega) + R_{yy}(\omega) = S_0(\omega) = I(\omega) \tag{3.8}$$

If we consider, for example, light described by the Jones vector:

$$\begin{bmatrix} E_H(t) \\ E_V(t) \end{bmatrix} \tag{3.9}$$

where:

$$E_i(t) = \int_{-\infty}^{+\infty} \epsilon_i(\omega) e^{-j\omega t} d\omega \tag{3.10}$$

The elements of the spectral coherency matrix are:

$$\begin{aligned} R_{ij}(\omega) &= \textstyle\int_{-\infty}^{+\infty} < E_i(t) E_j^*(t+\tau) > e^{j\omega\tau} d\omega \\ &= \epsilon_i(\omega)\epsilon_j^*(\omega) \end{aligned}$$

and it can be presented as:

$$R(\omega) = \begin{bmatrix} |\epsilon_H(\omega)|^2 & \epsilon_H^*(\omega)\epsilon_V(\omega) \\ \epsilon_H(\omega)\epsilon_V^*(\omega) & |\epsilon_V(\omega)|^2 \end{bmatrix} \tag{3.11}$$

Stokes parameters cannot be generally defined for the coherence matrix since it is Hermitian only for $\tau = 0$:

$$J^\dagger(\tau) = J(-\tau) \tag{3.12}$$

3.2 Two-photon Case

Consider the setup in Fig. 3.1. The two separate spatial modes are projected by two identical tomography devices and coincidence events between the two arms are detected. Each tomography device consists of a polarization tomography part followed by a Michelson interferometer in collinear configuration. It is preferable to use an interferometric configuration for evaluation of

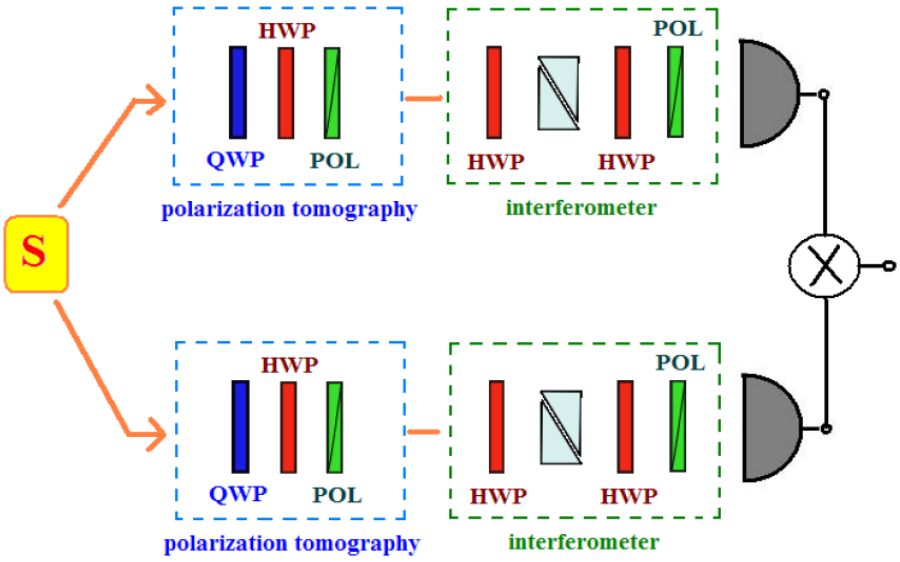

Figure 3.1: Schematic of experimental apparatus to measure the two-photon spectral coherence matrix (HWP = half-wave plate, QWP = quarter-wave plate, POL = polarizer). In each of the two separate photon paths there is a tomography device comprising a polarization tomography part and a collinear Michelson interferometer. Scanning 16 independent polarizatin settings and the two delay-lines one can retrieve the two-photon spectral coherence matrix elements.

spectral properties with respect to one based on a monochromator. In Fourier-transform interferometry spectral resolution can be made arbitrarily high by increasing the measurement interval, and, due to multiplex advantage [29], a higher signal-to-noise ratio is attainable in the case of the additive noise, that is common in single-photon measurements [30].
The polarization tomography device [17] converts the information regarding the polarization state into the amplitude of a linear polarized state. It consists of a quarter wave plate (at angle q with respect to the vertical direction), a half-wave plate (at angle h) and a vertical linear polarizer, described by the Jones matrix:

$$\begin{aligned} T(h,q) &= T_{POL}(\theta=0)T_{\lambda/2}(h)T_{\lambda/4}(q) \\ &= \frac{1}{2\sqrt{2}}\begin{bmatrix} 0 & 0 \\ 0 & 1 \end{bmatrix}\begin{bmatrix} \cos 2h & \sin 2h \\ \sin 2h & -\cos 2h \end{bmatrix}\begin{bmatrix} i-\cos 2q & \sin 2q \\ \sin 2q & i+\cos 2q \end{bmatrix} \\ &= \begin{bmatrix} 0 & 0 \\ \zeta_1(h,q) & \zeta_2(h,q) \end{bmatrix} \end{aligned}$$

In the collinear Michelson interferometer the input vertically polarized light is first rotated by 45 degrees thus providing equal horizontal and vertical projections. Then delay τ between the horizontally-polarized component and the vertically-polarized one is introduced through a birefringent delay-line, comprising two sliding quartz wedges. Finally, both polarization components are recombined again by means of a half-wave plate and a polarizer.

The quantized fields at the detectors are:

$$E_n^{(+)}(t_n) = \sum_{\gamma=0}^{1} \zeta_{n,\gamma} \int d\omega (1 + e^{j\omega\tau_n}) \hat{a}_{n,\gamma}(\omega) e^{-j\omega t_n} \tag{3.13}$$

with:

$$\zeta_{n,0}(h_n, q_n) = \frac{1}{\sqrt{2}} \{\sin(2h_n) - i \sin[2(h_n - q_n)]\} \tag{3.14}$$

and:

$$\zeta_{n,1}(h_n, q_n) = -\frac{1}{\sqrt{2}} \{\cos(2h_n) + i \cos[2(h_n - q_n)]\} \tag{3.15}$$

3.2.1 Interferograms

For a two-photon system considering the frequency and polarization degrees of freedom, the density matrix can be written as:

$$\rho = \sum_{i,j,k,l=0}^{1} \int d\Omega \int d\Omega' \int d\Omega'' \int d\Omega''' \rho_{(2i+j),(2k+l)}(\Omega, \Omega', \Omega'', \Omega''') \\ |(\Omega, i)_1; (\Omega', j)_2 >< (\Omega'', k)_1; (\Omega''', l)_2| \tag{3.16}$$

The coincidence count rate, integrating over time due to the slow detectors, can be calculated:

$$\begin{aligned} G(\tau_A, \tau_B) &= \int dt_1 \int dt_2 \quad \mathrm{Tr}\left[\rho E_1^{(-)}(t_1) E_2^{(-)}(t_2) E_2^{(+)}(t_2) E_1^{(+)}(t_1)\right] \\ &= \sum_{\lambda,\mu,\gamma,\delta=0}^{1} \int d\omega \int d\omega' (1 + \cos\omega\tau_A)(1 + \cos\omega'\tau_B) \\ &\qquad \zeta_\gamma \zeta_\delta \zeta_\lambda^* \zeta_\mu^* \quad \rho_{(2\gamma+\delta),(2\lambda+\mu)}(\omega, \omega'; \omega, \omega') \end{aligned} \tag{3.17}$$

Replacing the four one-photon polarization indices ($\gamma, \delta, \lambda, \mu$ = H, V) with two two-photon polarization indices:

$$k = 2\gamma + \delta \qquad l = 2\lambda + \mu \qquad k, l = 0..3 \quad \text{(HH, HV, VH, VV)} \tag{3.18}$$

and:

$$B_k = \zeta_\gamma \zeta_\delta \qquad B_l = \zeta_\lambda \zeta_\mu \tag{3.19}$$

So, going back to the coincidence count rate:

$$G(\tau_A, \tau_B) = \sum_{k,l=0}^{3} B_k B_l^* G_{k,l}(\tau_A, \tau_B) \tag{3.20}$$

where:

$$G_{k,l}(\tau_A, \tau_B) = \int d\omega \int d\omega' \rho_{k,l}(\omega, \omega') \left[1 + \cos(\omega\tau_A)\right] \left[1 + \cos(\omega\tau_B)\right] \tag{3.21}$$

The interferograms depend on:

$$R_{ij}^{(2)}(\Omega, \Omega') = \rho_{ij}(\Omega, \Omega', \Omega'', \Omega''')|_{\Omega''=\Omega, \Omega'''=\Omega'} \tag{3.22}$$

which we define as the elements of the two-photon spectral coherence matrix.

Since there are 16 unknown functions $R_{ij}^{(2)}$, 16 different polarization measurements (described by the index $\nu = 1...16$) are needed, with 16 independent values for $(h_1, q_1; h_2, q_2)$. Let's indicate the measured interferograms with:

$$G^{(\nu)}(\tau_A, \tau_B) = \sum_{k,l=0}^{3} B_l^{(\nu)*} B_k^{(\nu)} G_{kl}(\tau_A, \tau_B) \tag{3.23}$$

3.2.2 Two-photon Spectral Coherence Matrix

Let us now introduce the 2D Fourier Transform of the interferograms. The calculations are identical to the ones performed for the single photon case:

$$\begin{aligned} G^{(\nu)}(\Omega, \Omega') &= \int\int G^{(\nu)}(\tau_A, \tau_B) e^{-j\Omega\tau_A} e^{-j\Omega'\tau_B} d\tau_A d\tau_B \\ &= 2 \sum_{k,l=0}^{3} B_l^{(\nu)*} B_k^{(\nu)} \int d\tau_A \int d\tau_B \int d\omega \int d\omega' \rho_{kl}(\omega, \omega'; \omega, \omega') \\ &\qquad (1 + \cos\omega\tau_A)(1 + \cos\omega'\tau_B) e^{-j\Omega\tau_A} e^{-j\Omega'\tau_B} \end{aligned} \tag{3.24}$$

This time the physically significant function ($\Omega \geq 0$, $\Omega' \geq 0$) will be repeated in reversed form in the other three quadrants of the (Ω, Ω') plane. Switching from positive variables to variables defined on the whole real range, and selecting $\Omega > 0, \Omega' > 0$ we obtain:

$$G^{(\nu)}(\Omega, \Omega') = \sum_{k,l=0}^{3} B_l^{(\nu)*} B_k^{(\nu)} R_{kl}^{(2)}(\Omega, \Omega') \tag{3.25}$$

Introducing the new index: $\mu = 4k + l, \quad \mu = 0...15$ we can then build the 4-by-4 matrix:

$$\Gamma_{\nu\mu} = B_l^{(\nu)*} B_k^{(\nu)} \tag{3.26}$$

we have:

$$G^{(\nu)}(\Omega, \Omega') = \sum_{\mu=0}^{15} \Gamma_{\nu,\mu} \tilde{R}_{\mu}^{(2)}(\Omega, \Omega') \tag{3.27}$$

In matrix form:

$$\mathbf{G}(\Omega, \Omega') = \Gamma \tilde{\mathbf{R}}^{(\mathbf{2})}(\Omega, \Omega') \tag{3.28}$$

If the tomography apparatus settings have been chosen so that $\det\Gamma \neq 0$:

$$\tilde{\mathbf{R}}^{(\mathbf{2})}(\Omega, \Omega') = \Gamma^{-1} \mathbf{G}(\Omega, \Omega') \tag{3.29}$$

The spectral coherence matrix can be obtained with a simple rearrangement of the elements of the vector $\tilde{\mathbf{R}}^{(\mathbf{2})}(\Omega, \Omega')$:

$$\tilde{\mathbf{R}}^{(\mathbf{2})}_{kl} = \mathbf{R}^{(\mathbf{2})}{}_{4k+l} \tag{3.30}$$

3.2.3 Two-photon Spectral Stokes Parameters

As in the case of monochromatic twin-photon states, we can now formally express $R^{(2)}(\omega, \omega')$ in terms of the two-photon Pauli matrices $\sigma_{ij} = \sigma_i \bigotimes \sigma_j$, so that:

$$R^{(2)}(\omega, \omega') = \frac{1}{4} \sum_{i,j=0}^{3} S_{ij}(\omega, \omega') \sigma_{ij}(\omega) \tag{3.31}$$

The $S_{ij}(\omega.\omega')$ are the spectral two-photon Stokes parameters, generalization of the two-photon Stokes parameters defined by Abouraddy et al. [18]:

$$S_{ij}(\omega, \omega') = \mathrm{Tr}[R^{(2)}(\omega, \omega') \sigma_{ij}] \tag{3.32}$$

3.3 Examples

3.3.1 Pure state with general frequency correlation

Consider the state:

$$|\psi> = \int d\omega \int d\omega' \Phi(\omega, \omega') \left[\hat{a}^{\dagger}_{1H}(\omega) \hat{a}^{\dagger}_{2V}(\omega') + \hat{a}^{\dagger}_{1V}(\omega') \hat{a}^{\dagger}_{2H}(\omega) \right] |0> \tag{3.33}$$

where the function $\Phi(\omega, \omega')$ also contains information about the correlations between the frequencies of the two photons. An example could be Gaussian anticorrelation, like:

$$\Phi(\omega, \omega') = e^{-(\omega + \omega' - \Omega_p)^2 / \sigma^2} sinc(\Delta\omega) \tag{3.34}$$

The two-photon wavefunction is given by:

$$\begin{aligned} A(t_1, t_2) &= < 0 | \hat{E}^{(+)}_2(t_2) \hat{E}^{(+)}_1(t_1) | \psi > \\ &= \frac{1}{4} \int d\omega \int d\omega' (1 + e^{j\omega\tau_A})(1 + e^{j\omega\tau_B}) e^{-j\omega t_1} e^{-j\omega' t_2} \\ &\qquad \left\{ \zeta_{1H} \zeta_{2V} \Phi(\omega, \omega') + \zeta_{1V} \zeta_{2V} \Phi(\omega', \omega) \right\} \end{aligned} \tag{3.35}$$

which gives the following bidimensional interferogram:

$$
\begin{aligned}
G(\tau_A,\tau_B) &= \int dt_1 \int dt_2 \quad |A(t_1,t_2)|^2 \\
&= \frac{1}{4}\int d\omega \int d\omega' \quad (1+\cos\omega\tau_A)(1+\cos\omega\tau_B) \\
&\qquad \{|\zeta_{1H}|^2|\zeta_{2V}|^2|\Phi(\omega,\omega')|^2 + |\zeta_{1V}|^2|\zeta_{2V}|^2|\Phi(\omega',\omega)|^2 + \\
&\qquad \zeta^*_{1H}\zeta^*_{2V}\zeta_{1V}\zeta_{2H}\Phi^*(\omega,\omega')\Phi(\omega',\omega) + \zeta^*_{1V}\zeta^*_{2H}\zeta_{1H}\zeta_{2V}\Phi^*(\omega',\omega)\Phi(\omega,\omega')\}
\end{aligned}
\tag{3.36}
$$

From this we can extract the matrix:

$$
R^{(2)}(\omega,\omega') = \begin{bmatrix} 0 & 0 & 0 & 0 \\ 0 & |\Phi(\omega,\omega')|^2 & \Phi^*(\omega,\omega')\Phi(\omega',\omega) & 0 \\ 0 & \Phi^*(\omega',\omega)\Phi(\omega',\omega) & |\Phi(\omega,\omega')|^2 & 0 \\ 0 & 0 & 0 & 0 \end{bmatrix} \tag{3.37}
$$

3.3.2 Frequency-anticorrelated states

States produced by spontaneous parametric downconversion exhibit frequency anticorrelation as a consequence of energy conservation in the nonlinear process which leads to pair emission. In this specific case, one photon is at frequency ω and the other at frequency $\omega_p - \omega$. The general density matrix is, therefore:

$$
\begin{aligned}
\rho = \sum_{i,j,k,l=0}^{1} \int d\Omega \int d\Omega' \rho_{(2i+j),(2k+l)}(\Omega,\Omega_p-\Omega,\Omega',\Omega_p-\Omega') \\
|(\Omega,i)_1;(\Omega_p-\Omega,j)_2><(\Omega',k)_1;(\Omega_p-\Omega',l)_2|
\end{aligned}
\tag{3.38}
$$

Due to presence of correlations between the two photons, only one interferometer is needed, so that we have the interferogram:

$$
G(\tau_A,0) = 4\sum_{\lambda,\mu,\gamma,\delta=0}^{1} \int d\omega (1+\cos\omega\tau_A)\zeta_\gamma\zeta_\delta\zeta^*_\lambda\zeta^*_\mu \quad \rho_{(2\gamma+\delta),(2\lambda+\mu)}(\omega,\Omega_p-\omega';\omega,\Omega_p-\omega) \tag{3.39}
$$

As in the general case, we need 16 independent experimental interferograms:

$$
G^{(\nu)}(\tau_A) = 2\sum_{k,l=0}^{3} B_l^{(\nu)*} B_k^{(\nu)} \{G_{kl} + \rho_{kl}(\tau_a)\} \tag{3.40}
$$

with:

$$\rho_{k,l}(\tau_A) = \int d\omega \rho_{k,l}(\omega, \Omega_p - \omega) \cos(\omega \tau_A) \tag{3.41}$$

By using a one-dimensional Fourier transform and performing the same kind of matrix calculations we did for the general case we can recover the matrix we need.

For example, if we consider a polarization-entangled frequency-anticorrelated $|\psi^{(+)}>$ Bell state:

$$|\psi>=\int_{-\infty}^{+\infty} \Phi(\omega) \left\{ \hat{a}^{\dagger}_{1H}(\Omega_0+\omega)\hat{a}^{\dagger}_{2V}(\Omega_0-\omega) + \hat{a}^{\dagger}_{1V}(\Omega_0-\omega)\hat{a}^{\dagger}_{2H}(\Omega_0+\omega) \right\} |0> \tag{3.42}$$

which can also be rewritten as:

$$|\psi>=\int_{-\infty}^{+\infty} \left\{ \Phi(\omega)\hat{a}^{\dagger}_{1H}(\Omega_0+\omega)\hat{a}^{\dagger}_{2V}(\Omega_0-\omega) + \Phi(-\omega)\hat{a}^{\dagger}_{1V}(\Omega_0+\omega)\hat{a}^{\dagger}_{2H}(\Omega_0-\omega) \right\} |0> \tag{3.43}$$

the two-photon spectral coherence matrix is:

$$\begin{aligned} R^{(2)}(\omega) &= |\psi(\omega)><\psi(\omega')||_{\omega=\omega'} \\ &= \begin{bmatrix} 0 & 0 & 0 & 0 \\ 0 & |\Phi(\omega)|^2 & \Phi(\omega)\Phi^*(-\omega) & 0 \\ 0 & \Phi^*(\omega)\Phi(\omega) & |\Phi(-\omega)|^2 & 0 \\ 0 & 0 & 0 & 0 \end{bmatrix} \end{aligned} \tag{3.44}$$

Note that this state exhibit dispersion cancellation, as it appears in the expression $\Phi^*(\omega)\Phi(-\omega)$.

3.4 Discussion

We introduced a general approach for detailed characterization of the broadband polarization-entangled quantum optical state based on the spectral coherence matrix technique. Several results for single-parameter entangled states described in the literature can be obtained from our general consideration as special cases.

For example, our protocol produces the polarization quantum tomography approach introduced by Kwiat and coworkers [17] when a *monochromatic* two-photon state at frequency Ω_0 is considered:

$$\rho_{(2i+j),(2k+l)}(\Omega,\Omega',\Omega'',\Omega''') = \widetilde{\rho}_{(2i+j),(2k+l)}\delta(\Omega-\Omega_0)\delta(\Omega'-\Omega_0)\delta(\Omega''-\Omega_0)\delta(\Omega'''-\Omega_0) \tag{3.45}$$

when the relation between the measured interferograms and the spectral coherence matrix is:

$$G^{(\nu)}(\Omega,\Omega') = \sum_{\mu=0}^{15}\Gamma_{\nu,\mu}\widetilde{\rho}_{\mu}\delta(\Omega-\Omega_0)\delta(\Omega'-\Omega_0) \tag{3.46}$$

The delta-function frequency dependence can be factorized and dropped, thus producing a matrix equation based only on polarization.

In case of a *single photon*, on the other hand, our approach produces known classical spectral coherence matrix. In particular, the density matrix of a broadband single-photon wavepacket, can be expressed as:

$$\rho = \sum_{k,l=0}^{1}\int d\Omega \int d\Omega' \rho_{kl}(\Omega,\Omega')|\Omega,k><\Omega',l| \tag{3.47}$$

Having just one input spatial mode in such a case, we will need only one tomography device and one detector. The counting rate after integration over time, to account for slow detectors, is therefore:

$$\begin{aligned} G(\tau) &= \int dt \quad \mathrm{Tr}\left[\rho E^{(-)}(t)E^{(+)}(t)\right] \\ &= 2\sum_{k,l=0}^{1}\zeta_l^*\zeta_k\{G_{kl}+\rho_{kl}(\tau)\} \end{aligned} \tag{3.48}$$

where:

$$G_{kl} = \int d\omega \rho_{kl}(\omega,\omega) \tag{3.49}$$

and:

$$\rho_{kl}(\tau) = \int d\omega \rho_{kl}(\omega,\omega)\cos\omega\tau \tag{3.50}$$

The interferograms depend on the elements:

$$R_{ij}^{(1)}(\Omega) = \rho_{ij}(\Omega,\Omega')|_{\Omega'=\Omega} \tag{3.51}$$

which are the elements of the quantum spectral coherence matrix for the single photon case. By reducing the dimensionality of the process we defined

for the two-photon case we can retrieve the matrix elements $R_{ij}^{(1)}(\Omega)$ from the interferograms.

For example, considering a source emitting the single-photon wavepacket:

$$|\psi>=\int d\omega \left[\epsilon_H(\omega)\hat{a}_H^\dagger(\omega)+\epsilon_V(\omega)\hat{a}_V^\dagger(\omega)\right]|0> \tag{3.52}$$

we can retrieve the following matrix:

$$\mathbf{R^{(1)}}(\omega)=\rho(\omega,\omega)=\begin{bmatrix} |\epsilon_H(\omega)|^2 & \epsilon_H^*(\omega)\epsilon_V(\omega) \\ \epsilon_H(\omega)\epsilon_V^*(\omega) & |\epsilon_V(\omega)|^2 \end{bmatrix} \tag{3.53}$$

which corresponds to the classical case (Eq. 13).

In classical optics, the polarization properties of an optical device can be described by means of a 2-by-2 complex Jones matrix $L(\nu)$. The input and output spectral density matrices $R_0(\nu)$ and $R(\nu)$ are related by the transformation:

$$R(\nu)=L^\dagger(\nu)R_0(\nu)L(\nu) \tag{3.54}$$

In the same way a similar 4-by-4 complex matrix $T(\nu)$ can be defined for the two-photon polarization-entangled case:

$$R^{(2)}(\nu)=T^\dagger(\nu)R_0^{(2)}(\nu)T(\nu) \tag{3.55}$$

and can be used to characterize devices or materials that act on the two entangled photon wavepackets.

However, the more general and informative way to characterize the polarization properties of the material is the Mueller matrix. This is a real 4-by-4 matrix which, for classical light, relates four Stokes parameters of the input beam to the four Stokes parameters of the output beam:

$$\begin{bmatrix} S_0(\nu) \\ S_1(\nu) \\ S_2(\nu) \\ S_3(\nu) \end{bmatrix} = \begin{bmatrix} M_{11} & M_{12} & M_{13} & M_{14} \\ M_{21} & M_{22} & M_{23} & M_{24} \\ M_{31} & M_{32} & M_{33} & M_{34} \\ M_{41} & M_{42} & M_{43} & M_{44} \end{bmatrix} \begin{bmatrix} S_0^{(0)}(\nu) \\ S_1^{(0)}(\nu) \\ S_2^{(0)}(\nu) \\ S_3^{(0)}(\nu) \end{bmatrix} \tag{3.56}$$

In the quantum two-photon case the 16 spectral Stokes parameters for the output light will be related to the Stokes parameters of the two-photon input light by means of a 16-by-16 Mueller matrix:

$$\begin{bmatrix} S_0(\nu) \\ S_1(\nu) \\ ... \\ S_{15}(\nu) \end{bmatrix} = \begin{bmatrix} M_{0,0} & M_{0,1} & ... & M_{0,15} \\ M_{1,0} & M_{1,1} & ... & M_{1,15} \\ ... & ... & ... & ... \\ M_{15,0} & M_{15,1} & ... & M_{15,15} \end{bmatrix} \begin{bmatrix} S_0^{(0)}(\nu) \\ S_1^{(0)}(\nu) \\ ... \\ S_{15}^{(0)}(\nu) \end{bmatrix} \tag{3.57}$$

3.5 Conclusions

We have shown that all the quantities normally used to characterize the polarimetric properties of materials and devices in ellipsometry will have a counterpart for two-photon light. One major difference is a significant increase in dimensionality in the quantum case. This increase in dimensionality could be exploited in the field of optical measurement, providing more subtle information about the material system under investigation.

Several approaches have been available in the literature for independent evaluation and characterization of polarization states entangled either in polarization or in frequency. Here we concentrated on developing a generalized approach providing tools for a detailed characterization of a quantum-optical state that is entangled both in spectrum and in polarization. We accomplished this by generalizing the classical definition of the spectral coherence matrix in order to introduce the two-photon coherence matrix for a broadband two-photon entangled state. We then outlined the experimental procedure for the measurement of its elements and illustrated how it can be used to quantify properties of frequency-polarization entangled states. Moreover, we discussed that such a technique can be used to characterize properties of devices and materials through which such a two-photon entangled state has propagated. We believe that the increased system dimensionality in the quantum case will find applications for optical measurement techniques, particularly in the field of quantum ellipsometry.

This formalism could also be useful in the description of general nonlinear optical interactions that do not necessarily involve states of fixed polarization. For example, a spectral polarization engineering technique has found an important application in the field of optical attosecond physics. The polarization-gating of spectral components of the original laser pulse allows researchers implementing an efficient control of high-order harmonic generation in order to obtain a single attosecond laser pulse.

Characterization and control of spectral polarization [31, 32, 33] is also important in nonlinear spectroscopy, in photochemistry and in quantum control where ultrashort pulses with carefully designed spectral polarization are employed to drive specific tasks (chemical reactions, molecular alignment, etc.). It was recognised recently that the down conversion light, even if not coherent, can behave like ultrashort pulses due to its inherent correlation between signal and idler photons. For example, the two-photon absorption using down-converted light with spectrally-engineered entangled photons has been demonstrated recently [34]. Our formalism could help in extending these results into areas where spectral polarization is important.

This formalism will also be helpful in the technique we will examine in the following Chapter, where we will show that using the frequency-anticorrelated photons produced by SPDC one can increase the sensitivity in the measurement of odd-order dispersion coefficient. The two-photon spectral coherence matrix will be useful when dealing with spectral polarzation dispersion, for example in fiber optics communication systems.

Chapter 4

White-light interferometry with broadband frequency-anticorrelated light

The precise measurement of optical chromatic dispersion is important in basic science and in technological applications.
From a fundamental point of view, the dependence of the refractive index on wavelength can give important informations about the optical and electronic properties of materials (see, for example[35, 36]) and photonic structures [37]. Moreover, in ultrafast optics, dispersion provides limits in the generation and applications of femtosecond optical pulses [38]. All typical optical elements (mirrors, prisms, lenses...) contribute to the total dispersion, and must be carefully characterized.
As regards applications, dispersive phaenomena cause the spreading of optical pulses in fiber communication systems. With increasing bit rates, transmission bandwidths and wavelength-division-multiplexed channels, broader and broader optical bandwiths are injected into fiber systems, increasing more and more the detrimental effects of dispersion: precise measurement techniques are therefore required [39, 40].

White-light interferometry is a well-established technique which allows to measure group-delay dispersion, as well as higher-order dispersion, with high accuracy and resolution, using a low-coherence light source and a Michelson interferometer [41, 42, 43, 44, 45]. Since it is based on a Fourier-transform technique, the spectral resolution can be made arbitrarily high increasing the scanning interval and its performance is particularly good in the presence of additive noise [29].

As we discussed in Chapter 1, energy conservation in the SPDC process results in frequency-anticorrelation between the photons: if one photon is at frequency ω_s, then the other will be at frequency $\omega_i = \omega_p - \omega_s$. Frequency anticorrelated light exhibits the remarkable effect of even-order dispersion cancellation: the interference pattern in coincidence dectection between the two-photons after a beam-splitter depends only on the odd-order terms of the spectral phase, while the even-order terms get canceled. This effect has been exploited in time-of-flight measurements in dispersive materials, where from the temporal shift of an interference pattern the group delay acquired in the propagation can be retrieved. In these kind of measurements, a broader optical bandwidth can give a narrower interferogram, increasing the measurement accuracy. On the other hand, if the material is sufficiently dispersive, the interferogram broadens, reducing the precision with which its position can be estimated. A mechanism that eliminates group velocity dispersion can bring significant advantages in these situations and it has been applied to measure group delays [46] or to enhance the sensitivity in optical coherence tomography [47, 48].
Using SPDC light in white light interferometry one can measure the odd-order dispersion terms separately. Without noise there would be no profit in doing this: one can simply retrieve the spectral phase and can therefore separate the contributions from group delay, group delay dispersion and so on. But in this paper, we will show that, in the presence of noise, when dispersion broadens the interferogram, the reduction in the signal-to-noise ratio for the interferograms implies a reduction in the precision with which the dispersion coefficients can be estimated. Using frequency anticorrelated light, the broadening is reduced and the features of the interferogram remain clearer, resulting in a better accuracy in phase estimation, particularly in situations where the amount of noise is significant.
Even though dispersion cancellation was discovered and studied in the realms of quantum optics, it can be simulated classically, at the expense of added system complexity [49].

4.1 Introduction

4.1.1 Classical White-light interferometry

A typical white-light interferometry setup (see Fig. 4.1a) consists of a Michelson interferometer feeded by a source with broad optical bandwidth, for example a bulb, a femtosecond laser, or a superluminescent diode.
The input electric field E(t) is split by a beamsplitter into the two arms of the

Michelson interferometer. The field propagating through the first arm hits a translating mirror and is delayed of an amount τ with respect to the field travelling through the second arm. The presence of a dispersive sample (length L), in the second arm, causes the component at frequency ω, to acquire a phase:

$$e^{j\phi(\omega)} = e^{jk(\omega)L} \tag{4.1}$$

The intensity registered by the detector, integrated over time to account for slow detectors, is:

$$I(\tau) = 2\left\{I_0 + Re\left[\int_0^\infty |E_0(\omega)|^2 e^{j\Phi(\omega)} e^{-j\omega\tau} d\omega\right]\right\} \tag{4.2}$$

with:

$$I_0 = \int_0^\infty |E(\omega)|^2 d\omega \tag{4.3}$$

From the interferogram, by means of an inverse Fourier transform, $\Phi(\omega)$ can be retrieved.

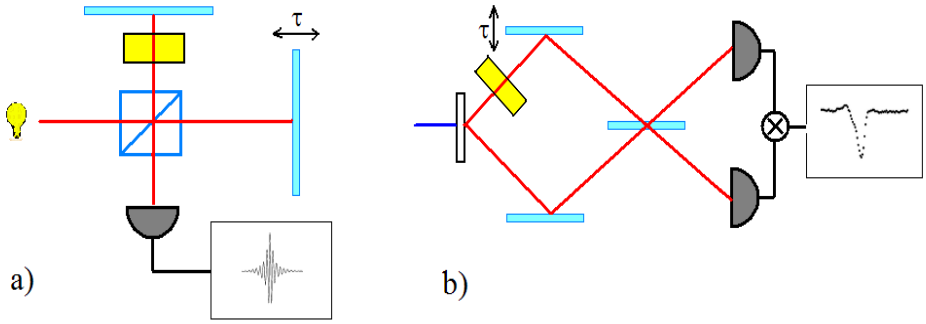

Figure 4.1: On the left experimental configuration for classical white light interferometry: a Michelson interferometer is feeded by a broadband optical source. From the recorded intensity interference pattern the spectral phase auired by propagation through the dispersive sample can be retrieved. On the right, a Hong-Ou-Mandel interferometer: photon emitted by parametric downconversion are sent to a beamsplitter and coincidence events are detected at the ouput ports. From the recorded interference pattern in the coincidence rate the odd-order terms of the spectral phase can be retrieved.

Assuming that the field spectrum $E_0(\omega)$ is centered around the frequency ω_0, the spectral phase function $\Phi(\omega_0 + \Omega)$ can be expanded in Taylor series:

$$\Phi(\omega_0 + \Omega) = \sum_{n=0}^{\infty} a_n \Omega^n \qquad a_n = \frac{1}{n!}\frac{d^n\Phi}{d^n\omega}(\omega)|_{\omega=\omega_0} \tag{4.4}$$

The coefficient c_1 is called group delay, and it measures the propagation optical path inside the material; its effect is a temporal shift of the interference pattern. The second order term, c_2 is called group delay dispersion and results in different frequencies travelling at different speeds, broadening the interferogram.

4.1.2 Quantum white-light interferometry

Twin photons emitted by SPDC exhibit entanglement between anticorrelated frequencies:

$$|\psi>=\int_{-\infty}^{+\infty}\zeta(\Omega)\hat{a}^{\dagger}(\omega_0+\Omega)\hat{a}^{\dagger}(\omega_0-\Omega)|0>d\Omega \tag{4.5}$$

Considering the configuration in Fig. 4.1b, the coincidence count rate at the detector is:

$$C(\tau)=C_0+2Re\left[\int_{-\infty}^{\infty}\zeta^*(\Omega)\zeta(-\Omega)e^{j\Gamma(\Omega)}e^{j\Omega\tau}d\Omega\right] \tag{4.6}$$

with:

$$C_0=2\int_{-\infty}^{\infty}|\zeta(\Omega)|^2d\Omega \tag{4.7}$$

and:

$$\Gamma(\Omega)=\Phi(\omega_0-\Omega)-\Phi(\omega_0+\Omega) \tag{4.8}$$

Expanding $\Phi(\Omega)$ in Taylor series we get:

$$\Gamma(\Omega)=\sum_{n=0}^{\infty}b_n\Omega^n \tag{4.9}$$

with:

$$b_n=\begin{cases}2a_n & \text{n odd}\\ 0 & \text{n even}\end{cases} \tag{4.10}$$

Therefore the interference pattern in coincidence events depends only on the odd-order terms of the spectral phase. The even-order terms, like group delay dispersion (c_2) get canceled. Since in many materials the coefficient c_2 is quite large, its cancellation results in narrower interferograms and higher accuracy for time-domain optical measurement techniques, like optical coherence tomography.

Since $\Gamma(\Omega)$ is an even function, i.e. $\Gamma(\Omega) = -\Gamma(-\Omega)$:

$$\begin{aligned} C(\tau) &= C_0 + 2Re\left[\int_{-\infty}^{\infty} \zeta^*(\Omega)\zeta(-\Omega)e^{j\Gamma(\Omega)}e^{j\Omega\tau}d\Omega\right] \\ &= C_0 + \int_{-\infty}^{\infty} \zeta^*(\Omega)\zeta(-\Omega)e^{j\Gamma(\Omega)}e^{j\Omega\tau}d\Omega + \int_{-\infty}^{\infty} \zeta^*(\Omega)\zeta(-\Omega)e^{-j\Gamma(\Omega)}e^{-j\Omega\tau}d\Omega \\ &= C_0 + \int_{-\infty}^{\infty} \zeta^*(\Omega)\zeta(-\Omega)e^{j\Gamma(\Omega)}e^{j\Omega\tau}d\Omega \end{aligned} \tag{4.11}$$

then, performing an inverse Fourier transform on the interferogram, $\Gamma(\Omega)$ can be retrieved.

4.2 Accuracy comparison for odd-order terms

White light interferometry can be performed using frequency anticorrelated light, to measure the odd-order terms. Due to factor 2 in Eq. 4.10, the coefficients in the quantum case are twice the values for in classical interferometry. The effect of the presence of group delay dispersion and other higher order terms is a temporal spreading of the different frequencies emitted by the source, resulting in a broadening of the interferogram.

An example of this effect is presented in Fig. 4.2, where simulations for propagation through a slab of ZnSe (5 mm long) are presented. The absence of even-order dispersion terms, including group velocity delay, makes the quantum interferograms more clear and with higher contrast with respect to the classical ones. Through numerical simulations we will show that, in situations where the noise level is comparable to the signal level, this effect can give benefits in terms of the accuracy of phase retrieval.

To give a quantitative estimate of the accuracy in the two cases we consider the classical and quantum interferograms produced passing through a slab of material, respectively $I_C^{(o)}(\tau)$ and $I_Q^{(o)}(\tau)$. From Eq. 4.10 the coefficients of the spectral phase in the quantum case (b_k) are non-zero only for the odd-order terms. Moreover, for the even-order terms, $b_k = 2 \quad a_k$.

We consider a noise process η and we add N different implementations $\{\eta_i(\tau), \quad i = 1..N\}$ to the interferograms. We get N noisy interferograms:

$$I_{C,i}(\tau) = I_C^{(o)}(\tau) + \eta_i(\tau) \qquad I_{Q,i}(\tau) = I_Q^{(o)}(\tau) + \eta_i(\tau) \tag{4.12}$$

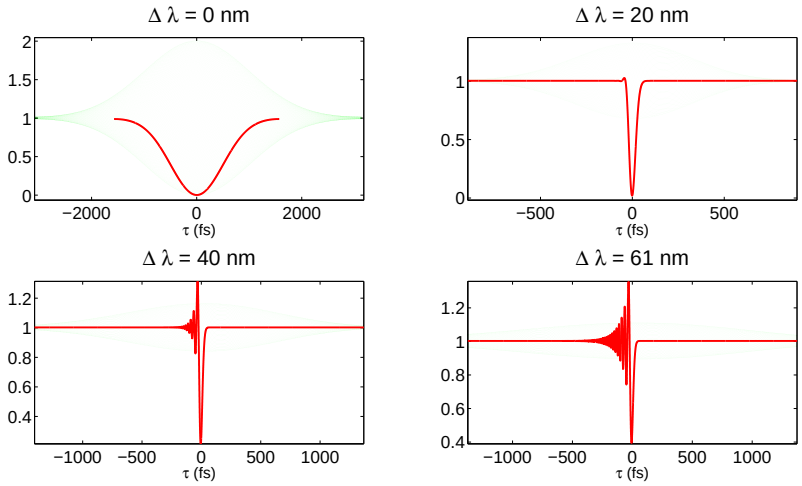

Figure 4.2: Comparison of classical and quantum interferograms for different source bandwidths, calculated for propagation in 5 mm of ZnSe. The dispersion-cancelled interferograms (red line) show higher contrast and clearer features than the classical ones (green line), giving higher performance in the presence of noise. The asimmetry in the quantum interferogram is due to the third order dispersion term, which becomes a clearer feature when the secont order term is cancelled.

For each interferogram we perform an inverse Fourier transform:

$$M_{C,i}(\omega) = \int_{-\infty}^{\infty} I_{C,i}(\tau) e^{-j\omega\tau} d\tau \qquad M_{Q,i}(\omega) = \int_{-\infty}^{\infty} I_{Q,i}(\tau) e^{-j\omega\tau} d\tau \tag{4.13}$$

and we retrieve the spectral phase function:

$$\phi_{C,i}(\omega) = \arg\left[M_{C,i}(\omega)\right] \qquad \phi_{Q,i}(\omega) = \arg\left[M_{Q,i}(\omega)\right] \tag{4.14}$$

For each classical and quantum phase function we make a least-squares polynomial interpolation, finding:

$$\phi_{C,i}(\omega) = \sum_{k=0}^{n} \alpha_k^{(i)} \omega^k \qquad \phi_{Q,i}(\omega) = \sum_{k=0}^{n} \beta_k^{(i)} \omega^k \tag{4.15}$$

We can then calculate the statistics for each of the coefficients a_k and b_k, based on the N values $\alpha_k^{(i)}, i = 1..N$ and $\beta_k^{(i)}, i = 1..N$. We take as the estimated value for a_k the mean value of the coefficients $\left\{\alpha_k^{(i)}\right\}$, and as the estimated value for b_k the mean value of the $\left\{\beta_k^{(i)}\right\}$:

$$\tilde{a}_k = \text{mean}\left\{\alpha_k^{(i)}, \quad i = 1..N\right\} \qquad \tilde{b}_k = \text{mean}\left\{\beta_k^{(i)}, \quad i = 1..N\right\} \tag{4.16}$$

From the standard deviations we can have an estimate of the measurement accuracy:

$$\sigma[a_k] = \mathrm{std}\left\{\alpha_k^{(i)}, \quad i = 1..N\right\} \qquad \sigma[b_k] = \mathrm{std}\left\{\beta_k^{(i)}, \quad i = 1..N\right\} \tag{4.17}$$

Since we are dealing with a finite sample (N individuals) of the population of all the possible coefficients retrieved from every possible implementation of the noise process, the precision with which we can estimate the standard deviation in Eq. 17 is limited. In particular, for a Gaussian probability density the error on the standard deviation is:

$$\sigma = \sqrt{\frac{2}{N-1}} \tag{4.18}$$

Increasing N would give higher precision in the estimate of the standard deviation, but would also require a longer computation time. A good compromise was found to be N = 2000, for which the error on the variance is of the order of a few percents.

4.2.1 Varying bandwidth

We first performed simulations with increasing source bandwidth and Poissonian noise. For a Poissonian noise process the signal-to-noise ratio depends on the signal level $I(\tau)$. For classical white-light interferometry (similar considerations are valid in the quatum case) the signal level for a balanced interferometer, with no sample, is:

$$I(\tau = 0) = 4I_0, \qquad I_0 = \int_0^\infty |E(\omega)|^2 d\omega \tag{4.19}$$

To compare the accuracy in cases with different bandwidths, we kept the value for I_0 constant, in order to have the same signal-to-noise ratio.

In Fig. 4.4 the values for $\sigma[a_k]$ and $\sigma[b_k]$ are presented for $k = 1, 2, 3$. Initially, if we increase the bandwidth, the measurement error σ gets lower and lower, since we add more information to our measurement and it is likely to expect higher accuracy. This is particularly evident in the case of higher-order dispersion (coefficients a_3 and a_5 in the picture), since higher order terms become more and more important when the bandwidth is large.
For larger bandwidths, dispersive effects become so strong to reduce the interferogram amplitude to a level comparable to the noise. In this situation phase

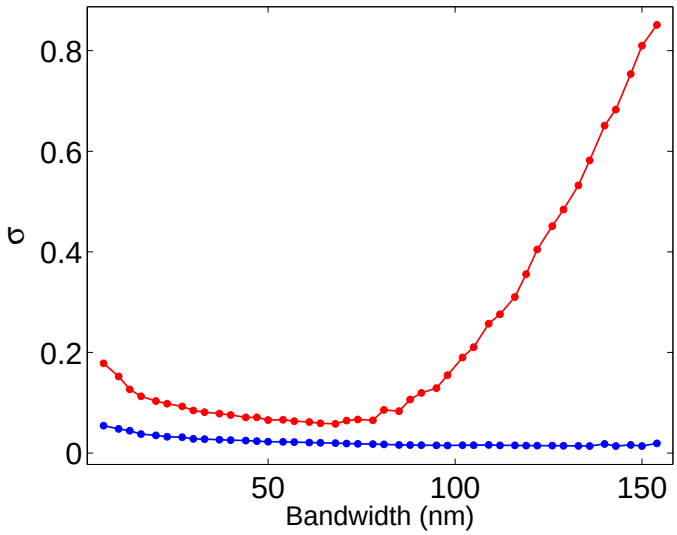

Figure 4.3: Measurement error on the group delay coefficient in the classical case (a_1, red line) and in the quantum case (b_1, blue line) with respect to the source bandwith (central wavelength 800 nm) for a slab of ZnSe 5-mm thick. The noise on the interferograms is assumed to be Poissonian. The error initially decreases increasing the bandwidth, since more and more information is added. When, due to dispersive broadening, the interferogram SNR becomes low, the classical measurement's accuracy grows worse and worse. On the other hand dispersion-cancellation keeps higher the SNR of the quantum interferogram.

retrieval becomes more and more complicated and the error for the classical case ($\sigma[a_k]$) starts to grow exponentially. Using dispersion cancellation, on the other hand, the signal-to-noise ratio in the time domain remains higher, allowing accurate phase retrieval.

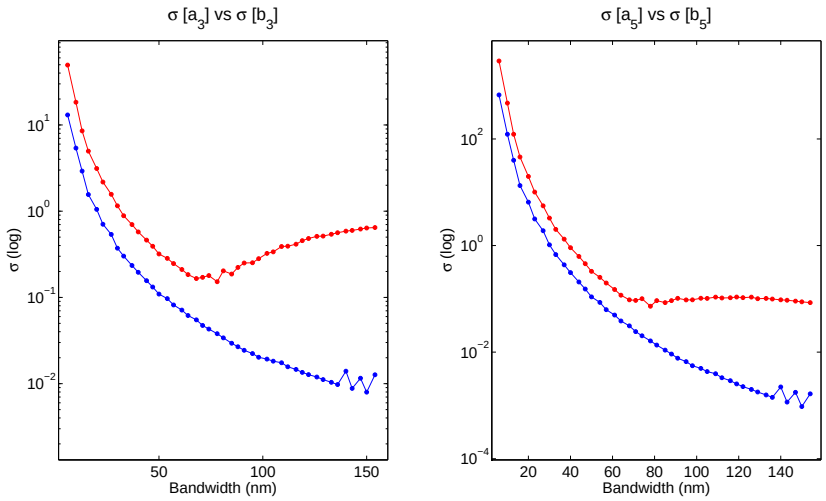

Figure 4.4: Logarithmic plot of the measurement error on third and fifth order coefficients with respect to the source bandwith, centered around 800 nm for a slab of ZnSe 5-mm thick. The error in the quantum case (blue line) is lower than it is in the classical case (red line). The noise on the interferograms is assumed to be Poissonian.

In dispersion-cancelled measurements we also get a factor 2 in the phase coefficients (Eq. 4.10). When doing experiments with monochromatic entangled photons the fact of having twice the phase that one gets in classical experiments increases the sensitivity in phase measurements, as if one was doing the measurement with light at double frequency. In the presence of dispersion, this is the case only if the phase is linear with the frequency, that is:

$$2\phi(\omega) = \phi(2\omega) \tag{4.20}$$

only if $\phi(\omega) = \alpha\omega$, as is the case in ranging applications [50] . However, even though in our case the dispersion relation $\phi(\omega)$ is much more complicated, the fact of getting twice the coefficients ϕ_n, given a fixed amount of noise, makes the quantum measurement, in general, more accurate. This can be seen in Fig. 4.3 and 4.4, where the error in the classical case ($\sigma[a_k]$) is always higher than in the frequency-anticorrelated case ($\sigma[b_k]$).

4.2.2 Varying noise level

In order to understand at what ratio between the interferogram amplitude and the noise level we have the break point in accuracy we performed some simulations keeping the bandwidth constant and adding a Gaussian noise process with zero mean and variable variance. In particular, to compare different cases we define a normalized noise level μ:

$$\mu = \frac{\zeta_G}{2I_0} \tag{4.21}$$

where ζ_G is the standard deviation of the Gaussian noise process.

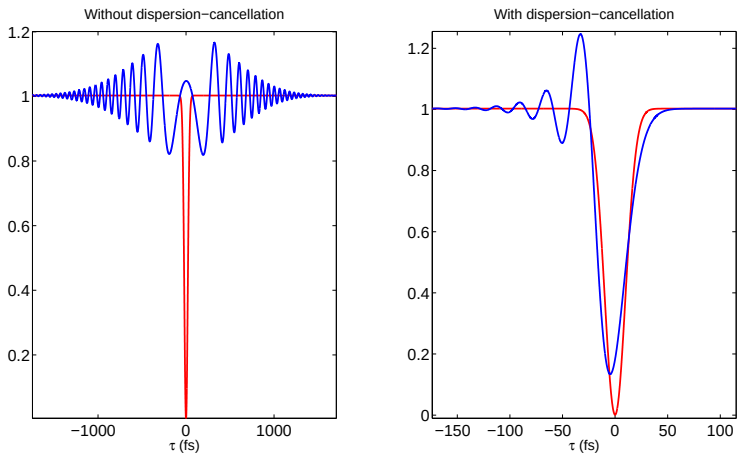

Figure 4.5: On the left, normalized envelope of the classical interferogram with (blue line) and without the sample (red line). On the left dispersion-cancelled interferograms with (blue line) and without (red line) the sample. In both cases the source bandwidth is 33 nm. These parameters are used in the simulations with different levels of Gaussian noise, shown in Fig. 6

Increasing the noise level, the errors $\sigma[a_k]$ and $\sigma[b_k]$ on the estimate of the coefficents get higher. But, while for low noise levels the error grows linearly, when the noise becomes comparable to the signal the $\sigma[a_k]$ (classical case) starts to increase exponentially. In the dispersion-cancelled measurements, instead, $\sigma[b_k]$ remains linear much longer (see Fig. 4.6).
In Fig. 4.7 the retrieved phase for 2000 noisy inteferograms can be seen. In the first row we are below the break point, and the classical interferograms give us a clear shape, while in the second row (noise level B) we can see that in the spectral regions where the signal has lower power (the ones at the extremes) there are problems in the phase retrieval and unwrapping that give a higher

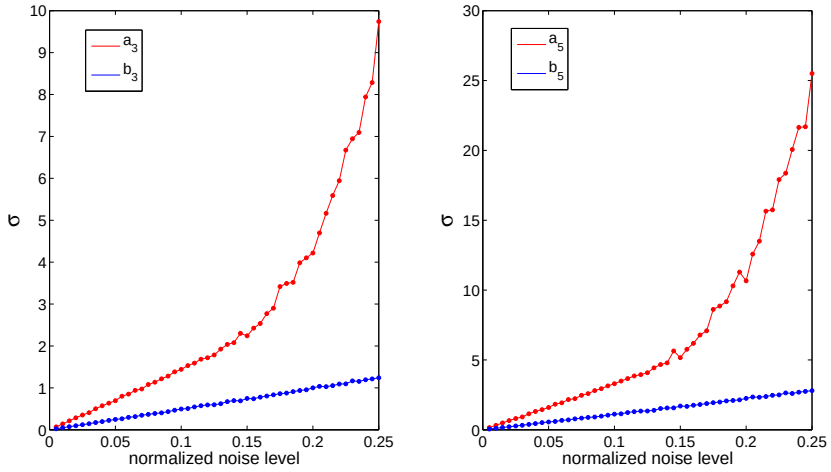

Figure 4.6: Measurement error on third (on the left) and fifth order (on the right) coefficients with respect to the normalized noise level. The noise is assumed to be Gaussian, with zero mean and incresing variance. The source bandwidth is 33 nm, centered around 800 nm and the light propagates through a slab of ZnSe 5-mm thick (see Fig. 5 for details). The error in the quantum case (blue line) is lower than it is in the classical case (red line).

error in the polinomial fit. On the other hand, the dispersion-cancelled phase remains much better.

4.2.3 Varying bandwidth and noise level

Curves for measurement errors $\sigma[a_1]$ and $\sigma[b_1]$ as a function of the source bandwidth for different normalized noise levels (ranging from 0.03 to 0.3) are shown in Fig. 4.8. As discussed in Section 2.1, increasing the source bandwidth the measurement error decreases, since our estimate is based on a larger and larger dataset of frequencies. On the other hand, when the bandwidth is so large that, due to dispersive effects, the signal level becomes comparable to the noise level, the measurement accuracy cannot be inceased more increasing the source bandwidth. The break-point bandwidth between the two regimes, as shown in Fig. 4.8, decreases with incresing noise. Classical (left side) and quantum (right side) regimes are compared in Fig. 4.8. For the same noise level, the break point occurs for shorter bandwidths in the classical case than it does in the quantum one.

For example, for a normalized noise level of 0.21, the source bandwidth for which the minimum measurement error can be obtained is nearly 40 nm in the classical case, while in the quantum case it is around 100 nm. The main

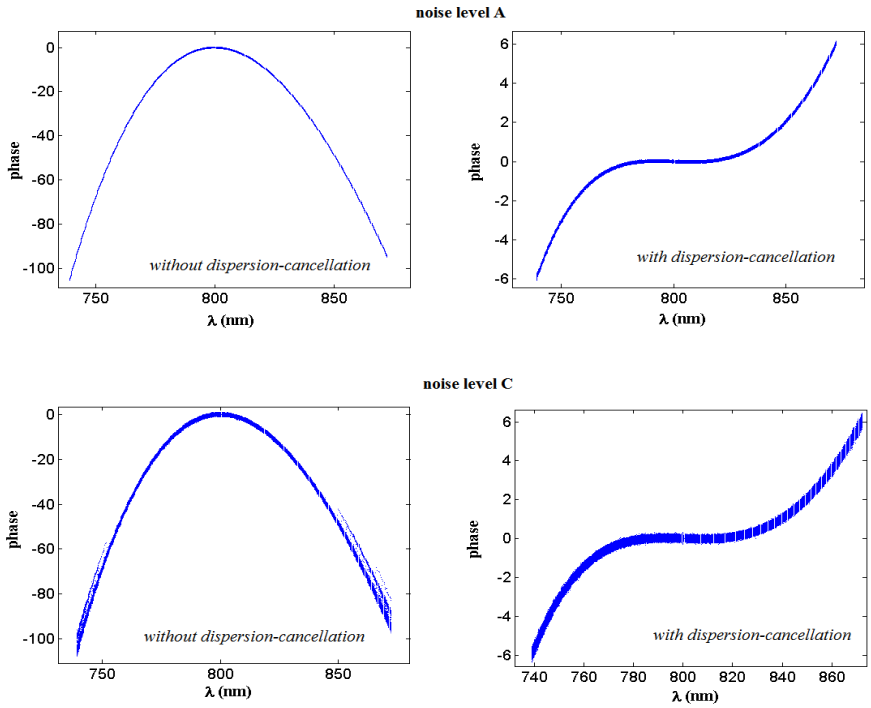

Figure 4.7: Phase reconstruction for 2000 interferograms with and without dispersion cancellation for two different noise levels. With noise level C we can see an increase in the phase error around 750 nm and 850 nm, which s responsible of the degrade of fit accuracy: this problem in not present in the corresponding dispersion-cancelled measurement

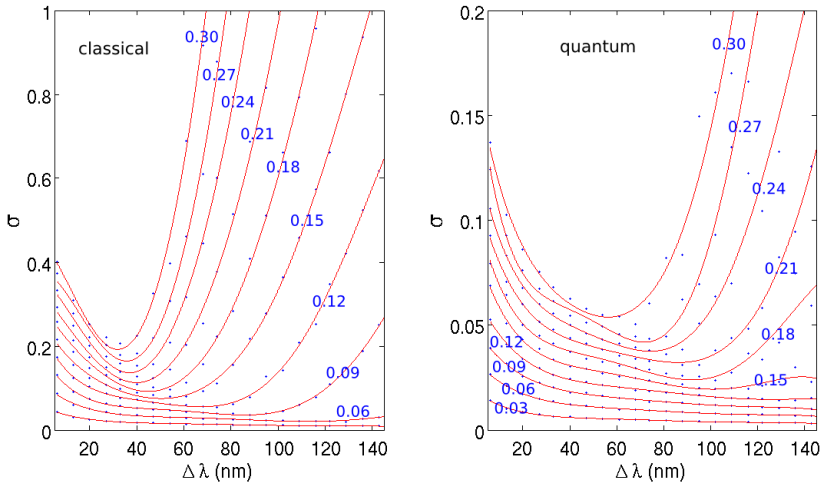

Figure 4.8: Curves for measurement error σ as a function of source bandwith for different noise levels, for classical (on the left) and quantum (on the right) measurements. The normalized noise levels span the interval between 0.03 to 0.3.

consequence is that the minimum measurement error is much lower in the quantum case ($\sigma = 0.015$) than in the classical case ($\sigma = 0.06$). A comparison is shown in Fig. 4.9. On the left, curves for the minimum measurement error as a function of source bandwidth and noise level are presented. It is evident that, for a given noise level, the bandwidth that gives the minimum error is shorter in the classical case than it is in the quantum one. On the left the minimum values for $\sigma[a_1]$ and $\sigma[b_1]$ are shown: the quantum error curve (red line) is always lower than the classical one (blue line).

4.3 Conclusions

We discussed the possibility of performing white light interferometry using spontaneous parametric downconversion in combination with a Hong-Ou-Mandel interferometer. This configuration exhibits the cancellation of the even-order dispersion terms.
We showed that the presence of a highly dispersive sample reduces the signal-to-noise ratio in classical white-light interferometry, decreasing the measuement accuracy of the dispersion coefficients. The possibility of measuring only the odd-order coefficients, given by Hong-Ou-Mandel iterferometry, keeps the signal-to-noise level higher for larger bandwidths. This results in higher accuracy in the measurement of odd-order dispersion terms.

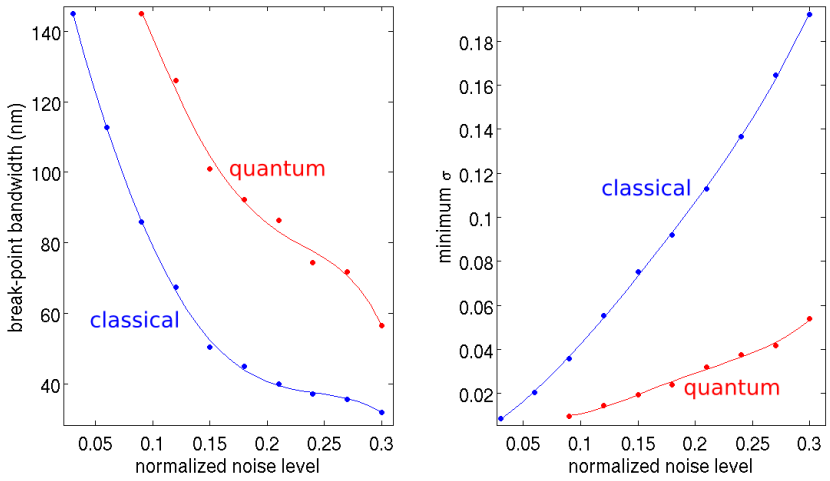

Figure 4.9: On the left, characterizazion of the break point where the measurement error starts to increase with increasing source bandwith. The break-point bandwith is plotted with respect to different noise levels for classical (blue line) and quantum (red line) cases. Increasing the noise level the break-point bandwidth decreases. For the same noise level, the break-point bandwidth is smaller for classical sources than it is for quantum sources. On the right, minimum measurement errors (at the break-point bandwidth) for classical (blue) and quantum (red) cases, plotted as a function of the normalized noise level. Increasing the noise level the minimum measurement error increases, but in the quantum case it is always smaller than in the classical case.

The technique we proposed may as well be suited for spectral polarization measurements, using the formalism for the spectral two-photon coherence matrix introduced in Chapter 3.

All the work presented in this Chapter was made by the PhD candidate and was performed during his visit to Quantum Imaging Laboratory (Boston University).

Chapter 5

The QSpace experiment

The area where the concept of entanglement has found the most successful application is Quantum Information.
As the trend of miniaturization in electronic components moves further and further, quantum effects start to become more and more important. Since the electronic devices that we presently use work according to classical laws, the presence of quantum effects, like tunneling, would clearly degrade their performace. But, on the other hand, the possibility to control quantum effects could potentially allow us to design new devices with completely new properties.
Since the rules that the physical devices obey determine also the rules under which information is processed, transferred and stored, people have started to elaborate a new theory of information based on the rules of quantum mechanics, giving birth to the science of Quantum Information.
If the basis of classical information is the bit, a variable which can assume the value 0 or the value 1, its quantum counterpart is the qubit, which is a quantum coherent superposition of a state $|0>$ and a state $|1>$.

5.1 Quantum Cryptography

The first practical application of the new paradigms introduced with the development of Quantum Information Theory is Quantum Cryptography, or Quantum Key Distribution (QKD). It is a technique which exploits the superposition principle and the indetermination principle to distribute a secret key between two parties, allowing the detection of eavesdroppers in the channel.
Consider a qubit:

$$|Q>=\alpha|0>+\beta|1>, \qquad \alpha,\beta \in C \tag{5.1}$$

Such a state can be implemented with any quantum two-level system, for example an atom, a particle in a double-well potential, a spin-1/2 particle, or the polarization of a single photon. Since this last one is the most convenient system of choice in communication experiments, we will concentrate on this specific implementation, assuming that $|0>$ is the horizontally-polarized state and $|1>$ is the vertically-polarized one.
As regards photon polarization state, measurements are performed using polarizers. A measurement in the basis $\{|0>, |1>\}$ would give the output 0 with a probability $p_0 = |\alpha|^2$ or the value 1 with a probability $p_1 = |\beta|^2$. As a consequence of the measurement operation the qubit will suddenly collapse to the state $|Q>= |0>$ if the result of the measurement was 0, or to $|Q>= |1>$ if the result was 1.
Suppose now that two parties, Alice and Bob agree to use the qubit:

$$|+>= \frac{1}{\sqrt{2}} [|0> +|1>] \tag{5.2}$$

to encode the value 1. If Bob sets his polarizer at an angle $\theta = \pi/4$, he can retrieve the value 1 with 100% probability and he has no chance to find the complementary value 0, associated to the state:

$$|->= \frac{1}{\sqrt{2}} [|0> -|1>] \tag{5.3}$$

On the other hand, a measurement on the basis $\{|0>, |1>\}$ will give either the outcome 0, or the outcome 1, each with 50% probabilty. Moreover the state will be perturbed, becoming $|0>$ or $|1>$ and therefore exhibiting different outcome statistics with respect to the original state. So, if an eavesdropper, let's call her Eve, performs a man-in-the-middle attack, with a measurement in the wrong basis she will perturb the state making her presence detectable from the statistics of Bob's measurement outcomes.
Suppose now that Eve somehow discovers which basis Alice and Bob are using: she would then be able to set her analyzers on that basis and retrieve all the bits without adding perturbations. To avoid this Alice an Bob must add unforeseen changes: Alice uses one of two orthogonal bases to encoded her bits so anyone else, Bob and Eve included, cannot know which basis has been used. Bob will set up his receiver randomly, sometimes for a measurement on the basis 1, sometimes for a measurement in basis 2: so, sometimes he will find the correct result, sometimes he will find something completely random. To know in what cases they were using the same basis they can comunicate the basis choices on a classical communication channel: in the end Alice and Bob will know which bits have been received correctly and which must be discarded. The classical

channel will be used also to compare a small subset of the data: differences between Alice's and Bob's data above a certain threshold will mean that a perturbation has been introduced, revealing the presence of an eavesdropper. Just like Bob, sometimes Eve will get correct results, sometimes random ones. Even though she could listen to the classical channel the informations she can get are completely useless because the measurement she performed will be different from the ones performed by Bob and the perturbation introduced by her measurements will reveal her presence. The only thing she could do is to copy the qubits transmitted, store them and perform measurements on the correct bases using the data shared by Alice and Bob in the final classical communication.
But this is prohibited by the **No-cloning Theorem**.

The No-cloning Theorem

According to this theorem, proved by Wooters and Zurek in 1982 ([51]), a quantum cloning apparatus, that is a machine that can copy the qubit $|Q>$ in a blank state $|\flat>$ does not exist.
Let us consider an ipothetical quantum cloning machine which copies a qubit $|a>$ or $|b>$ in a blank state, while its status changes from $|\psi_0>$ to $|\psi_a>$ or $|\psi_b>$:

$$\begin{cases} U|\psi_0>|a>|\flat>=|\psi_a>|a>|a> \\ U|\psi_0>|b>|\flat>=|\psi_b>|b>|b> \end{cases} \quad (5.4)$$

Let's now calculate:

- $<\flat|<a|<\psi_0|U^\dagger U|\psi_0>|b>|\flat>=$

$$<\flat|<a|<\psi_0|\psi_0>|b>|\flat>=<a|b>$$

- $<\flat|<a|<\psi_0|U^\dagger U|\psi_0>|b>|\flat>=$

$$<a|<a|<\psi_a|\psi_b>|b>|b>=<a|b>^2<\psi_a|\psi_b>$$

So one finds:

$$<a|b>^2<\psi_a|\psi_b>=<a|b>$$

If $|a>$ and $|b>$ are not orthogonal then $<a|b>\neq 0$ and we can simplify:

$$<a|b><\psi_a|\psi_b>=1$$

But this equation cannot be true, because:

$$| < a|b > | < 1$$

$$| < \psi_a|\psi_b > | \leq \|\psi_a\|\|\psi_b\| = 1$$

So, a quantum cloning machine does not exist.

5.1.1 The BB84 protocol

The first protocol created according to these ideas was the BB84 protocol, proposed in 1984 by Charles Bennet and Gilles Brassard. The steps required to share a secret quantum key according to this protocol are the following:

1. the first step is to choose two bases. For example:
   - basis 1 : $\{|0>, |1>\}$
   - basis 2 : $\{|+>, |->\}$
   The bases are maximally conjugated, that is, any pair of vectors, one from each basis, have the same overlap (e.g. $| < 1|+ > |^2 = 1/2$): we choose this because we want a measuremtn performed in the wrong basis to give a completely random result (i.e. 0 or 1 with 50% probability).

2. Alice and Bob must agree on an encoding scheme for the bits. For example they can attribute the value 0 to $|0>$ and $|->$ and the value 1 to the other two states.

3. Alice sends individual qubits to Bob chosen at random among the four possible states. Bob measures the incoming qubits in one of the two basis, again chosen at random. In the cases they use the same basis, Alice and Bob will get perfectly correlated results, while, whenever the chosen bases are different, their results will be completely uncorrelated.

4. Using the classical channel Bob announces for each bit which basis he has used. Alice reveals if the chosen basis is the correct one. Both Alice and Bob discard the uncorrelated bits. This shorter key obtained after basis reconciliation is called the *sifted key*.

5. Alice and Bob compare in the classical channel a small subset of their results. If, considering also the possibility of errors due to the channel

noise, their results agree, then noone has tried to eavesdrop. On the contrary they must discard all data and the process must be repeated.

Note that neither Alice nor Bob decide which key to use: the key is grown by the conjunction of their random choices. So, what we are talking about is not a communication process, where Alice creates a key and sends it to Bob, but a **Quantum Key Distribution (QKD)** process, where the same key is created automatically in the process at both Alice's and Bob's sides.

In Table 1.1 one can see an example of BB84 protocol usage.

basis Alice	qubit sent	received?	basis Bob	poss. outcomes	result	final
2	$\|- >$	yes	1	0/1	0	—
1	$\|1 >$	yes	1	1	1	1
1	$\|1 >$	yes	2	0/1	0	—
2	$\|+ >$	no	2	-	-	—
1	$\|0 >$	yes	1	0	0	0
2	$\|+ >$	yes	2	1	1	1
2	$\|+ >$	yes	1	0/1	1	—
1	$\|0 >$	yes	2	0/1	1	—
2	$\|+ >$	yes	2	1	1	1
1	$\|0 >$	no	1	-	-	—
1	$\|1 >$	yes	1	1	1	1
2	$\|- >$	yes	2	0	0	0

Table 5.1: Example of QKD using BB84 protocol

5.1.2 Entanglement-based QKD

Entanglement can be a useful resource to share a secret key between two parties, as proposed for the first time by Artur Ekert in 1991.
Consider an entangled singlet state:

$$|\psi >= \frac{1}{2}\left[|0_A 1_B > -|1_A 0_B >\right] \tag{5.5}$$

and suppose the two particles are shared between Alice and Bob, who perform measurements respectively along the directions described by the angles α and β. As we have seen in Chapter 1 there is perfect anticorrelation between the

results obtained by Alice and Bob if their analyzers have the same orientation. After the transmission has taken place, Alice and Bob can announce publicly the analyzer settings they have independently chosen for each measurement and separate one one for which they chose the same basis from the one for which the chosen basis was different. They can then reveal publicly the results for the measurements with different bases to calculate the value of S (defined in Eq. 1.9: quantum mechanics requires $S = 2\sqrt{2}$). If the value of S is the correct one then they can keep the values measured with the correct bases, knowing that they are perfectly anticorrelated. Otherwise the presence of an eavesdropper can be detected.

5.1.3 Quantum channels

A typical QKD experiment comprises a photon source (single photons or entangled pairs), a quantum channel, and a detection system. As the channel is concerned experiments are usually performed in fibers or free-space.

Fiber links

Fiber links have the advantage that communication does not depend on external conditions, like weather or the presence of obstruction. On the other hand the conservation of the photon polarization state in fibers is a quite delicate topic, due to problems regardin the geometric phase, birefringence, polarization mode dispersion and polarization-dependent losses.
The geometric phase is the problem of following a linear polarization state for example through a loop of the fiber in the three-dimensional space: the final state will differ from the initial state by an angle. This is not such a big problem, provided that the fiber does not move too fast in space: only an alignment of reference systems between Alice and Bob is needed.
Birefringence is the presence of two different phase velocities for orthogonal polarization states, caused by asimmetries in the fiber core, which applies a unitary transformation to the polarization-encoded qubit. If this transformation is stable enough (due to slow thermal and mechanical vibrations), it can be easily inverted.
Polarization mode dispersion is the presence of two different group velocities for two orthogonally polarized modes. It creates decoherence, which would be devasting for quantum communication. The remedy is to use as narrowband photons as possible.
Polarization-dependent loss is a differential attenuation between two orthogonal polarization modes, which is usually negligible in fibers but can be strong

in other optical components, like phase modulators.
Much research work has been put in order to create QKD fiber links, over longer and longer links, reaching the present record of 123 Km. However, the major problem is nowdays in the detectors, since telecom fiber work inthe zero-dispertion region around 1550 nm, where APD have very poor performance. A possible solution, currently under investigation by many research groups, is the use of superconducting single-photon detectors (SSPDs).

Free-space links

Free-space links have some advantages with respect to fiber links. Particularly the atmosphere has a high transmission window around 800 nm, where efficient single-photon detector exist and is weakly dispersive and essentially nonbirefringent. On the other hand free-space transmission provides higher losses due to diffraction, and is very sensitive to stray light and weather conditions. Numerous experiments have been performed [52, 53, 54, 55, 56], both with weak pulses and entangled photons, reaching 144 Km in a recent experiment using astronomical telescopes at the Canary islands **??**.

Space-based QKD

Terrestrial free-space links suffer from light loss due mostly to objects interposed in the line of sight, beam distortion induced by atmospheric turbulence, bad weather conditions and aerosols and they are thus limited to rather short distance. A solution to this problem can be the use of Space and satellite technology.
Space-based links have the potential to realize global-scale quantum networking since they allow, in principle, a much larger propagation distance of photonic qubits compared to present fiber links. This is mainly due to the fact that most of the communication path is in empty Space, where the photons can freely propagate, and only a short section of the path is in atmosphere. The atmosphere provides low absorption in the regime of 600 nm - 850 nm (i.e. where good single-photon detectors are available) and is almost nonbirefringent, which guarantees the preservation of photon polarization at a high degree.
However many technical problems must be overcome in order to realize a working quantum communication link between Earth and Space: the satellite is a fast-moving target, whose position must be known very precisely.

5.2 The QSpace experiment

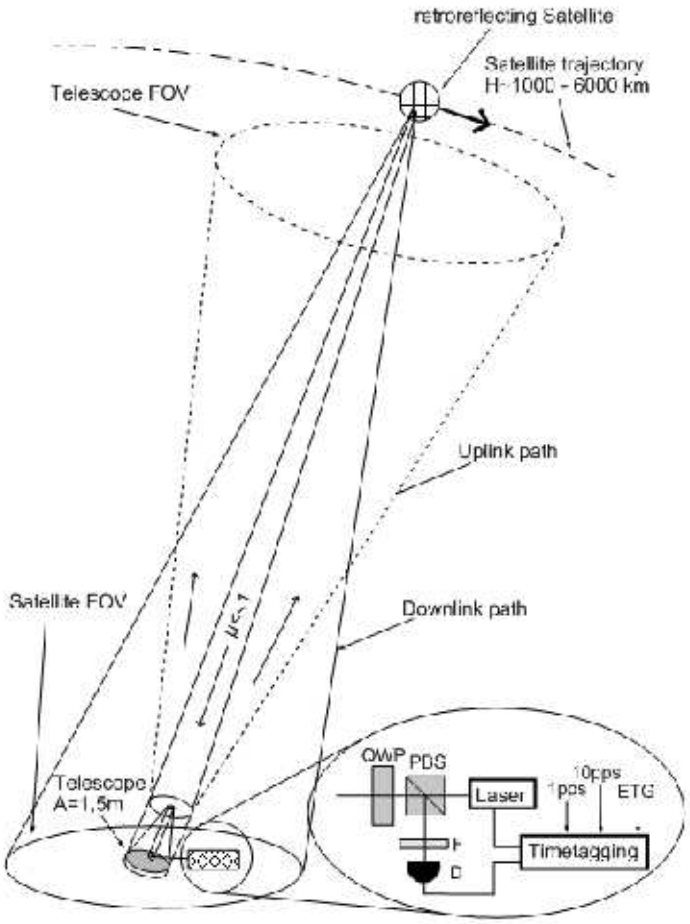

Figure 5.1:

A common feature to all quantum communication schemes, including quantum cryptography, is the need, at the receiver side, to correctly identify those signal photons that managed to travel across the communication link, given that the link may have a large attenuation and a large amount of background noise. Here we present the results for the experimental investigations of single photon exchange between a ground based receiver and a low Earth orbiting (LEO) transmitter based on a satellite-laser-ranging (SLR) satellite.
SLR satellites have been devised for geodynamical studies and are used to monitor the Earth's gravitational field by a series of measurements of the round-trip

time (range) of an optical pulses from a station on Earth and the retroreflectors onboard the satellites. We took advantage of the fact that their trajectories can be predicted in real time with good precision thanks to very accurate modeling based on their previous passes observed by the International Laser Ranging Service (ILRS) network.
The experimental idea was to send a laser pulse to a SLR satellite, which got then retroreflected back to the telescope, choosing the relevant parameters in order to have less than one photon in the channel from the satellite to Earth. This way a quantum source on a moving satellite could be simulated, with the aim to demonstrate to detect the signal photons against the strong background noise.
Our investigation differs with respect to the SLR techniques, also when the latter reaches the single-photon regime (as in the case of Moon laser-ranging or kHz SLR) in the sense that we are counting the returns in a series of predetermined time bins and not measuring the range time. Our observable is not the trip time but the detector count rate (DCR), as an initial step towards the measurement of the photon polarization state.

5.2.1 Experimental configuration

MLRO

The experiment was set up at the Matera Laser Ranging Observatory (MLRO) in Matera, Italy. MLRO is a state-of-the-art facility for satellite and lunar laser ranging, part of the International Laser Ranging Service network (ILRS).
MLRO is equipped with an astronomical quality telescope, consisting of a 1.5 meters prymary mirror and a long Coude configuration built with a small convex secondary and five plane mirrors (see Fig. 5.2). The Coude configuration exhibits no hole in the primary and delivers the light to a fixed focus point that does not move as the telescope is reoriented. While the primary has a wide-band aluminum coating, all the other mirrors are covered with a dielectric coating with a narrowband reflection window around 532 nm. The system is constructed to have a diffraction-limited beam divergence, continuously tunable from 1 to 20 arcseconds.

The telescope is mounted in alt-azimuth configuration having two perpendicular axes of motion, one vertical (altitude) and one horizontal (azimuth). It features a tracking velocity of 20 deg/sec in azimuth and 5 deg/sec in elevation, with a tracking accuracy of 1 arcsecond RMS.
MLRO is finally equipped with a Cesium beam frequency standard, which is used to sincronize all the operation and can time-tag the photons with 0.01

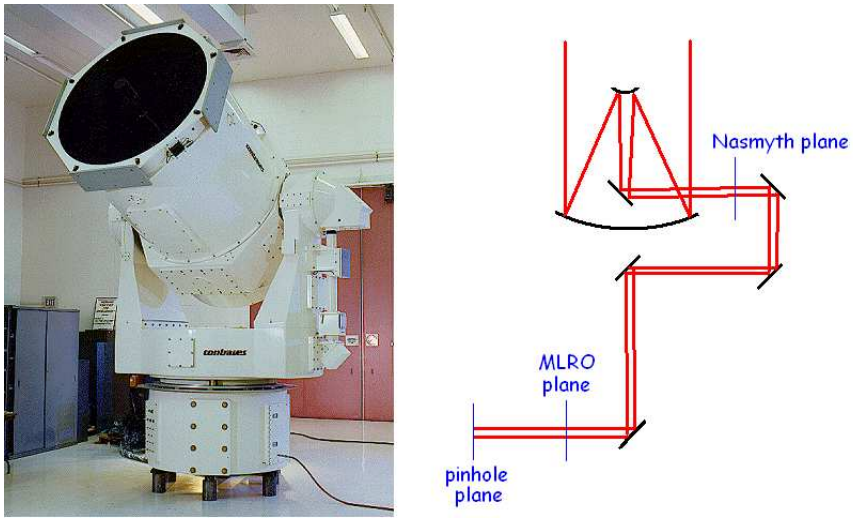

Figure 5.2: Scheme for the QSpace experiment. The aim is to simulate a single photon source on a satellite to demonstrate the feasibility of a single-photon link.

nanoseconds resolution.

Our setup

The experimental configuration is shown in Fig. 5.3. As a source we used a Q-switched Nd:YAG laser emitting pulses with energy 490 nJ at 532 nm and repetition rate 17 kHz. Since the upward and downward links share the same same optical path, we employed the polarization degree of freedom to separate the two: the pulses are originally vertically polarized and are transmitted through a Glan-Thompson polarizer. Then they travel trough a quarter-wave plate at 45 degrees, and are directed through the telescope to the satellite. After being reflected by the cornercubes they come back through the same path, travelling again through the same quarter-wave plate and becoming horizontally polarized. This way they are now reflected by the Glan-Thompson and directed to the detection apparatus.
The collimated light coming from the telescope was focused into a 0.5 mm pinhole by means of an off-axis parabola and then collimated again with a lens. This part of the setup was common to the upward and downward paths, and the pinhole was used the reference used to align the two paths so as to make them indistinguishable.
For the directional filtering, the design of the field-of-view has to mediate between different requirements: on one hand it is desirable to narrow the field

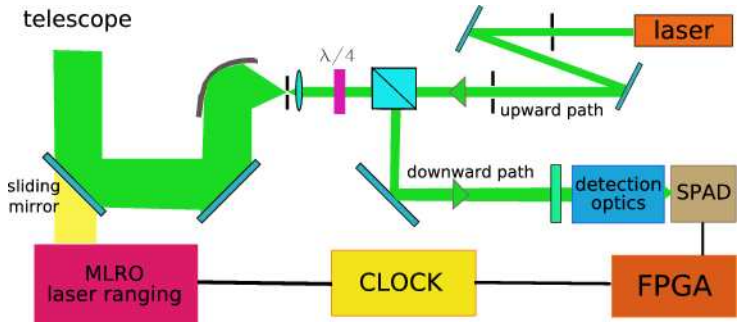

Figure 5.3: Experimental setup for the QSpace experiment. A Q-switched Nd:YAG laser emits vertically-polarized pulses (490 nJ, 17 KHz repetition rate) in the upward path, which are transmitted by a polarizing beamsplitter and sent to the telescope through a quarter-wave plate (QWP). The pulses are retroreflected by the satellite into the same path in the backward direction, pass again through the quarter-wave plate, becoming horizontally-polarized, and are therefore reflected by the PBS entering the detection section. Here they are spectrally filtered and focused into the detector. The detector output events are time-tagged and stored by an FPGA-based control board. The overall timing is guaranteed by the MLRO cesium frequency standard. A moving mirror is used to switch between the Qspace experiment and the MLRO satellite tracking modality.

in order to reduce the amount of background, which scales with the gathered solid angle. On the other hand, an appropriately large field-of-view is necessary to account for the varying arriving angle of the single photons with respect to the outgoing beam due to velocity aberration [57], and to the blur due to atmospheric fluctuations and the pointing noise of the telescope. We found that the optimal field-of-view value for our experimental conditions was 30 arc seconds.

The detection apparatus was a set of three lenses designed in order to set the correct value for the field of view that would be focused into the size of the detector. The detector was a Perkin Elmer silicon avalanche photodiode, passively quenched, with a sensitive area of diameter $500\mu m$.

To ensure the effective tracking of the telescope, the satellite was first acquired and tracked by the MLRO original laser ranging system. The range values were measured using its strong laser pulses (with a repetition rate of 10 Hz, wavelength 532 nm, pulse energy 0.1 J). After some minutes of successful SLR tracking, the telescope optical path was switched onto the quantum-channel system by moving a motorized mirror into the beam, while the telescope continued to follow in open loop the satellite along its trajectory. The quantum-channel system was kept active for an interval of about five minutes, and then the configuration was switched back to the MLRO system, in order to check the satellite tracking status and to perform further laser-ranging measurements.

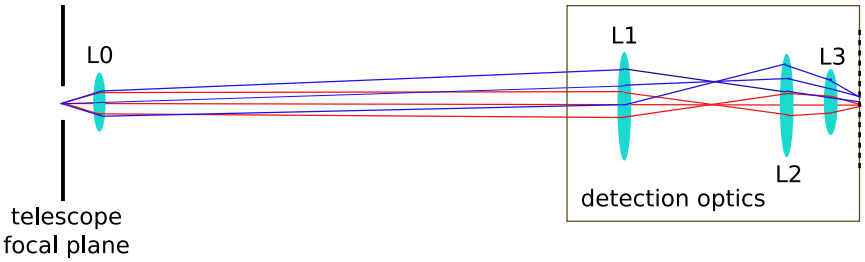

Figure 5.4: Detailed scheme for the downward path optics. A pinhole (diameter 500μm is placed on the telescope focal planem and the light is then collimated by means of the lens L0 (f = 8 mm), which is common to both the upward and backward paths. The actual detection setup consists of three lenses L1, L2 and L3, with $f_{L1} = 50mm$, $f_{L2} = 25mm$ and $f_{L3} = 8mm$. The distances between the lenses are: d_{01} = 200 mm, d_{12} = 80 mm, d_{23} = 10 mm. This system, coupled to the telescope by means of the off-axis parabola, can collect light with a field of view of 30 arcseconds, and focus it into the detector area (500 μm).

Usually, two or more transitions between the MLRO ranging system and our quantum channel were done during each pass of the satellite.
As regards the time of arrival, the round-trip duration was calculated for each laser shot, on the basis of the satellite distance (range, R_s) obtained using the predicted satellite position (ETC) distributed by ILRS. All time-sensitive operations (laser firings, detector tags, telescope tracking increments, etc.) were referred by our FPGA-based timetagging unit to the UTC provided by the atomic clock at the MLRO, thus insuring full compliance with the ILRS ephemerides. To further refine the a-posteriori analysis, the range values were improved by the NASA/GSFC analysis code Geodyn [58] which applies a very complete modeling of the forces acting on the satellite and uses all the observations by the worldwide ILRS network, including those we took with MLRO operating in its nominal mode. A very high timing accuracy (equal or better than 1 ns) was thus reached, ensuring that the estimate of the arrival time in the data analysis was derived by the best available information for the satellite passage. Accurate determination of time proved to be the most crucial part in the analysis of the results, so we give in the next Section some additional discussion.

Characterization of timing acuracy

There are many instrumental sources of temporal jitter: the laser for the outgoing pulse, the single-photon detector, the electronics, the optics. The influence of these factors was characterized by measuring the range value for ground targets around MLRO, and found to be about 1 ns. Additional sources of time jitter, each having approximately the same magnitude of the instrumental fac-

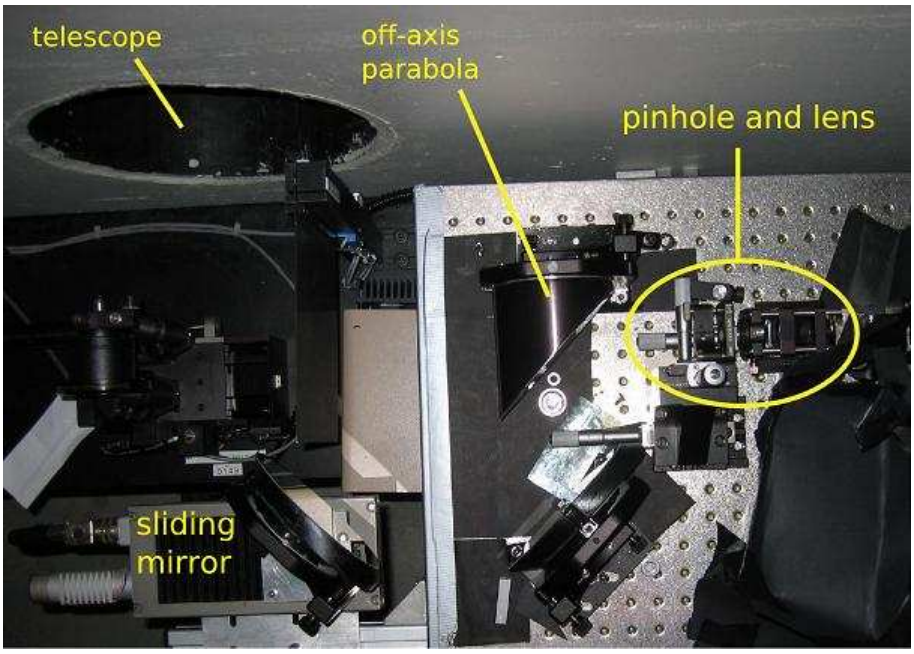

Figure 5.5: Photograph of the section between the telescope entrance and the $500\mu m$ *pinhole.*

tors, are the error in the synchronization with the timing signal of the station, and the precision in the orbital predictions. Regarding the influence of the satellite orbit on the arrival time: the instantaneous range R_s is of the order of $R_s \approx 10^6 - 10^7 m$. Since the satellite is moving, the duration of the photon travel from the source to the receiver, which is proportional to R_s, varies very rapidly, up to several μs/second. Each satellite pass lasts from several minutes to half an hour, according to the satellite orbit. During this interval, the satellite trajectory is far from smooth, being influenced by the Earth's gravity anomalies, which introduce temporal fluctuations that can be as high as 100 ns. Therefore, the time delay between emission and arrival times is a rapidly changing and difficult to model quantity, but its proper determination is of crucial importance for the realization of a quantum channel. Accordingly, we expected that the best signal to noise ratio could be achieved for bin sizes Δt from 1 to 20 ns, and this expectation was confirmed by the subsequent analysis.

Characterization of the detection optics

The detection optical system was mounted in the lab and characterized before being employed in the actual setup. The mounted system is shown in Fig. 5.7. The source is taken to be a 0.5-mm pinhole, where the off-axis parabola would

Figure 5.6: Photograph of the FPGA-based control electronics

focus the light gathered with a 30 arcsecond field-of-view.
To characterize the collection optics we used a point source, which we moved in the focal plane of the off-axis parabola (let's call it Π-plane), recording the detector counts. The point source was realized with a $50 - \mu m$ pinhole, illuminated by a lamp, which was imaged 1:1 into the Π-plane by means of a 2f imaging system.
The experimental data are shown in Fig. 5.8, clearly the light emitted in the 0.5-mm region, which correspond to the focus of the off-axis parabola, is properly collected by the system and focused into the detector.

5.2.2 Link Budget

In this section we will make an estimate of the link budget in order to understand how many photons we have in the receiving channel to validate the hypothesis to be in quantum regime ($\mu \ll 1$).
Our laser emits pulses with energy $E_P = 490nJ$ at 532 nm (energy per photon: $E_{ph} = h\nu = 3.586 \cdot 10^{-19}$) with repetition rate $R_{laser} = 17KHz$, giving a number of photons per second N_0 :

$$N_0 = \frac{E_P \cdot R_{laser}}{E_{ph}} = 2.32 \cdot 10^{16} \tag{5.6}$$

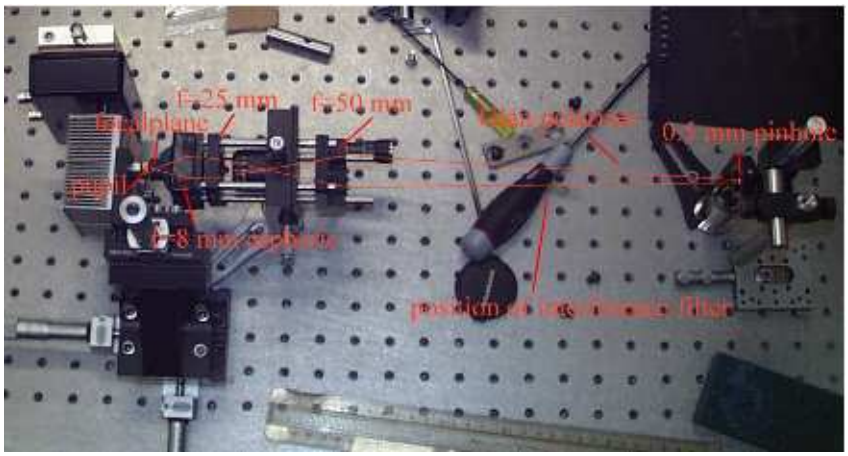

Figure 5.7: Detection optics setup mounted for characterization.

The effciency of the link can be calculated according to the formula:

$$\eta_{tot} = \eta_d \eta_T G_T \sigma_{SAT} \left(\frac{1}{4\pi R^2} \right)^2 A_T \eta_R T_A^2 T_C^2 \tag{5.7}$$

where:

- η_d is the detector quantum efficiency (in our case $\eta_d = 0.1$)
- η_T is the trasmitter optics efficiency. For our setup the transmitter optics consists of the upward section of the optical bench ($\eta = 0.1$), the Coudé path ($\eta = 0.1$) and the primary mirror ($\eta = 0.5$), giving a total $\eta_T = 5 \cdot 10^{-3}$.
- G_T is the transmitter gain ($G_T = 7 \cdot 10^9$)
- the satellite cross-section, for Ajisai, is $\sigma_T = 1.2 \cdot 10^7$
- A_T is the telescope area. For our 1.5-m diameter, $A_T = 1.77 \quad m^2$
- η_R is the receiver optics efficiency. For our setup the receiver optics consists of the downward section of the optical bench ($\eta = 0.08$), the Coudé path and the primary mirror, giving a total $\eta_T = 4 \cdot 10^{-3}$.
- T_A is the atmospheric transmission coefficient ($T_A = 0.9$)
- T_C is the cloud transmission coefficient ($T_C = 1$)

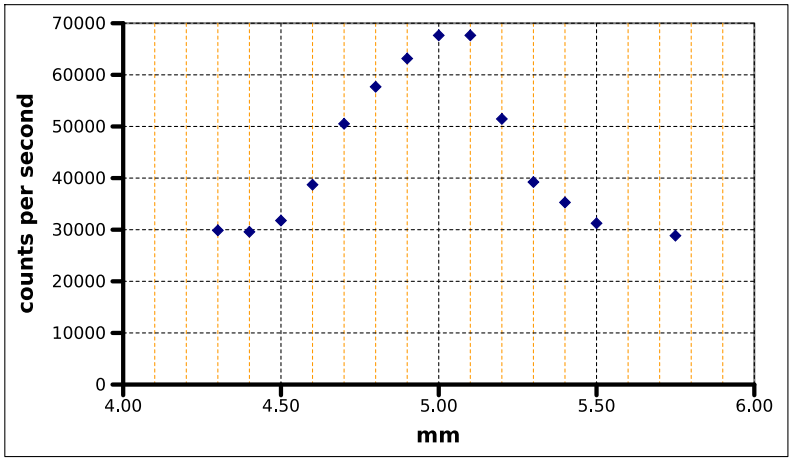

Figure 5.8: Characterization of the detection optics. The pinhole was illuminated with a lamp and the detector was moved on the detection plane to measure the focusing spot.

Using these values we get, for Ajisai:

$$\eta_{tot} = 2 \cdot 10^{-15}$$

The number of detected photons per second, i.e. the detector count rate (DCR) is:

$$N_{ph} = \eta_{tot} N_0 = 4.6 \quad s^{-1}$$

The total loss in the downlink is given by:

$$\eta_{DL} = \sigma_{sat} \eta_{rec} \eta_{QE} A_T \frac{1}{4\pi R^2} T_A T_C \tag{5.8}$$

and the number of photons in the receiving channel can be calculated as:

$$N_{DL} = \frac{DCR}{R_{laser} \eta_{rec} \eta_{QE} A_T T_A T_C} \tag{5.9}$$

For Ajisai the number of photons in the receiving channel results to be $N_{DL} = 0.4$.

Comparison between different satellites

In Table 5.2 one can see a comparison for the detector rates for four different satellites (Ajisai, Beacon C, Topex and Lageos). Clearly, a link is established if the number of good events per second is greater than the statistical fluctuations: from our data is clear that Ajisai will be the satellite that would give

	Ajisai	Beacon C	Topex	Lageos
detector rate	4.6	1.2	0.8	0.01
loss in downlink	$2.2 \cdot 10^{9}$	$6 \cdot 10^{10}$	$3.7 \cdot 10^{-10}$	$8.4 \cdot 10^{-11}$
phot from sat per pulse	$1.2 \cdot 10^{5}$	$1.12 \cdot 10^{5}$	$1.22 \cdot 10^{5}$	$7.8 \cdot 10^{4}$
phot in the channel per shot	0.38	0.097	0.064	0.0009
prob of det per laser shot	$2.7 \cdot 10^{-4}$	$6.9 \cdot 10^{-5}$	$4.5 \cdot 10^{-5}$	$6.6 \cdot 10^{-7}$

Table 5.2: Comparison between different satellites addressable from MLRO. Clearly Ajisai gives the higher detector rate, but for all satellites the number of photons in the channel per shot is below 1, as it must be to set the quantum regime.

more likely good results.
For all the chosen satellites the number of photons per shot in the channel is less than one, endorsing our claim to work in the quantum regime.

5.2.3 Data Analysis

First of all, we had to determine the time-scale offset between our setup and the MLRO one, due to different cable lengths, detector internal electronics, etc... To do so, we measured the distance of a ground target, 200 m apart, finding:

$$t_{offset} = -3999630 \quad ns$$

Durig the experimental sessions, the detector clicks were time-tagged and stored in a file. The recored data comprise:

- the detector click times $\{t_i^{(ret)}\}$
- the laser pulse emission times $\{t_j^{(L)}\}$
- the timing of the 10pps MLRO signal $\{t_k^{(10)}\}$
- the expected return times for the 10-pps signal photons $\{t_k^{(CFD)}\}$

So, the expected range for the 10 pps signal was calculated: $r_k = t_k^{(CFD)} - t_k^{(10)}$. Then using a linear fit, the expected range was calculated for all the 17-Khz fire instants between each two 10 pps pulses, giving the values $\{r_j\}$. Finally the expected return times for the photons where calculated:

$$t_j^{(exp)} = t_j^{(L)} + r_j + t_{offset}$$

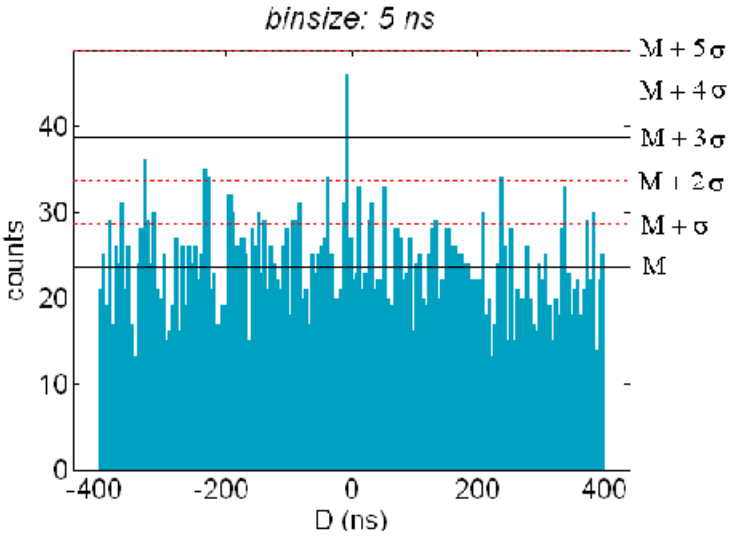

Figure 5.9: Histogram of D_{ij} for 5 seconds of the Ajisai passage of June 28, 2005 (time bin 5 ns). It is evident the clear peak at $D = 0$, 5σ above the mean, indicating the presence of return photons.

Subsequently the instants of all detection events were correlated with those of the transmitted laser pulses: for each detection event time $t^{(ret)_i}$, the deviation D from the expected return time $t_j^{(exp)}$, $D_{ij} = t_j^{(exp)} - t_i^{(ret)}$ was then computed. These D_{ij} values, grouped in several bins Δt of varying width (from 1 to 20 ns), were accumulated over short arcs of the total satellite pass. The duration of the short orbital arcs could not exceed 20 seconds, the maximum allowed by the open-loop tracking capability of MLRO, and their beginning was slid over the whole acquisition.
According to our criteria, the evidence of the single photon link would have been provided by a statistically significant peak, meaning a peak:

- centered at $D = 0$
- higher than 3 standard deviations σ of the D value distribution
- persist in the histograms by varying the values of Δt, to prove not be a random artefact of the histogram

A peak in the returns' histograms satisfying both conditions was identified for the Ajisai passage of June 28 2005, at about 1 a.m. UT, in the time interval 11-16 s after the start of acquisition. The peak is centered at D = 0, as required, and is nearly 5σ above the mean. Moreover, the peak remains well

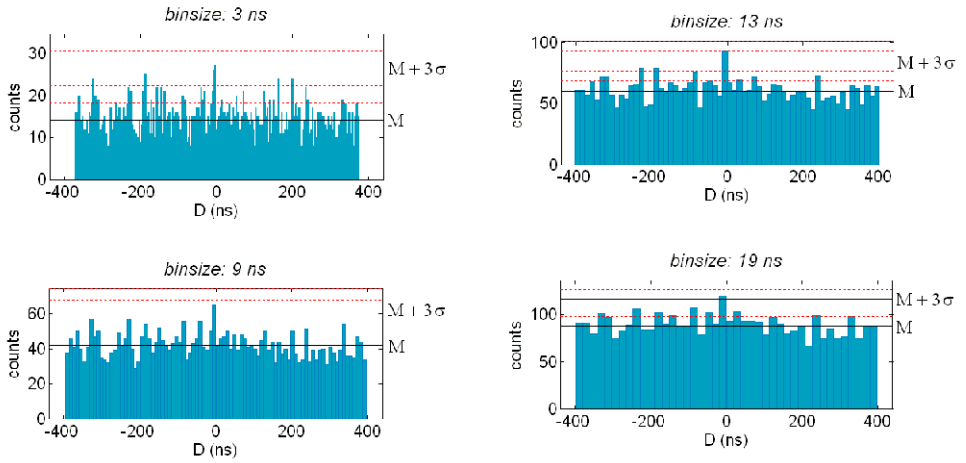

Figure 5.10: Histograms with different bin sizes for the same interval of the Ajisai passage. Note the persistency of the peak in $D = 0$, indicating that it is due to real signal and it os not just a statistical artifact in the data.

above the statistical limit of 3 standard deviations σ even when analyzing the data with various time bins Δt between 3 to 19 ns. Its statistical significance is at its highest value for $\Delta t = 5$ ns. This value nicely confirms our expectation: the lower side is set by the addition of the instrumental jitters, the higher side by lowering the SNR for accepting a higher spurious background at large bin sizes.
Therefore, the statistical significance of this peak is clearly established. The measured count rate in the peak is 5 counts per second, corresponding to a probability to detect a photon per emitted laser pulse of $3 \cdot 10^{-4}$. As already stated, taking into account the losses due to detection efficiency (-10dB) and the losses in the detection path (-11dB), the average photon number per pulse, μ, emitted by the satellite and acquired by our detector is approximately $4 \cdot 10^{-2}$, i.e. well within the single photon regime.

5.3 Polarization preservation in Space-based quantum channels

Polarization-encoding is currently one of the most widespread realizations of photonic qubits, which utilizes two orthogonal states of polarization to encode information onto the optical mode of a single photon. Since the atmosphere does not affect the polarization of photons, it is also the system of choice for free-space quantum communication schemes.

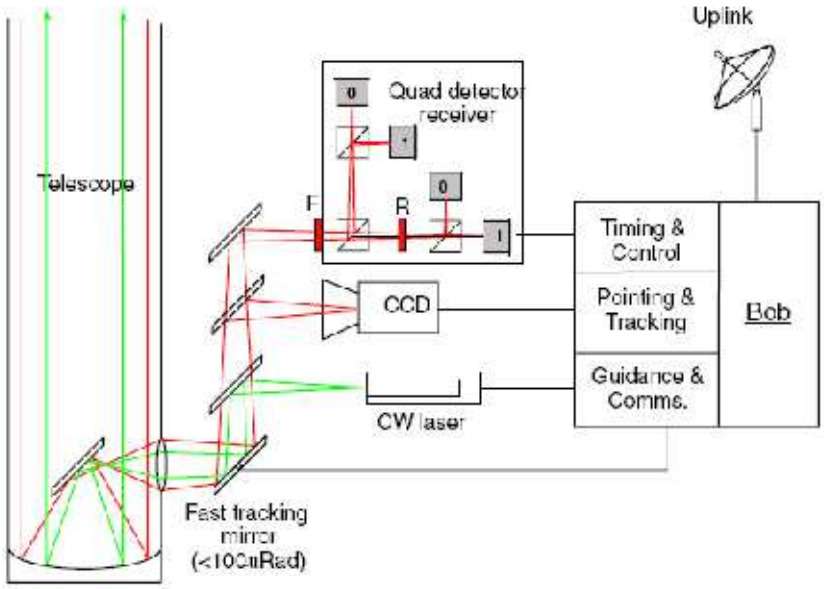

Figure 5.11: Example of a receiver system for satellite quantum communication. Satellite pointing and tracking is done by means of a moving plane mirror (from [59])

In order to establish a quantum communication protocol between two parties a system is needed to send the single photons emitted by the source on the satellite to the ground station, where the receiver is located. This is achieved by a pointing system made of a set of mirrors (see, for example, Fig. 5.11); in this paper we consider a simplified model with two plane ones: the first, on the satellite, sends the photons to the ground station whatever the position of the satellite on the sky is while the second one, in the ground station, receives the photons and, wherever they come from, sends them to the polarization analysis apparatus.
A working quantum communication protocol involving single-photons necessitates a shared reference frame between the communicating parties. For the interesting case of a moving satellite (e.g. LEO or MEO) the problem arises that any spatial reference frame between a Space-born transmitter and an Earth-based receiver will also be modified due to the movement of the involved pointing and tracking mirrors. In the following, we provide an analysis of this effect and discuss possible compensation schemes such as the use of a reference beam. It is important to state that, differently from classical laser communication, in polarization-encoded quantum communication all the polarization

states must be transmitted and received correctly, so that the compensation of polarization transformation induced by the channel is a crucial issue.
As long as polarization measurements involve only qubits, encoded in two orthogonal polarization states of a single photon, the classical theory of polarization and the quantum one coincide [60]; so, in the case under investigation, single photons emitted by a source on a satellite and detected by an Earth-based receiver, the classical Jones calculus will be used.

5.3.1 The model

To model this situation we chose a reference frame whose origin is the Earth center and the intersection between the Earth's equatorial plane and the satellite's orbital plane is y direction (see Fig. **??**). The z direction is orthogonal to the equatorial plane, while the x direction is chosen so as to have an orthonormal frame. Let ξ be the orbit inclination, that is the angle between the equatorial plane and the orbit plane.

To simplify the model we make the following approximations:

- the satellite orbit is supposed to be circular
- the model we propose takes into account only two pointing mirrors. A real system will be more complex than this and other optical devices could introduce their own perturbations to the polarization states of the transmitted photons. However, since fixed mirrors will provide only a constant offset to the polarization rotation, the time-dependent contribution will come only from the two pointing mirrors.
- the beam coming from the quantum communication source on the satellite is supposed to be tangent to the satellite's orbit: this is certainly arbitrary. Moreover, in a real situation, the satellite could also rotate around its axis, changing the direction of the incoming beam.
- simulations are performed for aluminum mirrors

The normal to the equatorial plane is: $\mathbf{N}_{equat} = (0, 0, 1)$ while the normal to the orbital plane can be obtained from this by a rotation of ξ along the y axis:

$$\mathbf{N}_{orb} = \begin{bmatrix} \cos\xi & 0 & \sin\xi \\ 0 & 1 & 0 \\ -\sin\xi & 0 & \cos\xi \end{bmatrix} \begin{bmatrix} 0 \\ 0 \\ 1 \end{bmatrix} = \begin{bmatrix} \sin\xi \\ 0 \\ \cos\xi \end{bmatrix} \tag{5.10}$$

The same procedure can be applied to find the equation of the satellite's orbit. A circular orbit on the equatorial plane would have been described by: $\mathbf{x} =$

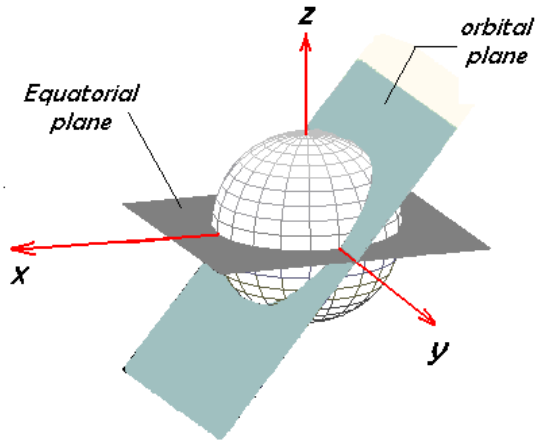

Figure 5.12: Fixed reference frame: the origin is set in the Earth center, the z direction is orthogonal to the equatorial plane and the y direction is on the intersection between the equatorial and the orbital planes

$R_o(\cos\omega t, \sin\omega t, 0)$ where R_o is the orbital radius. The actual orbit can be found from this performing a rotation of an angle ξ around the y-axis:

$$\mathbf{x} = R_o(\cos\xi\cos\omega t, \sin\omega t, -\sin\xi\cos\omega t) \tag{5.11}$$

The position of the ground station on Earth is a point on a spherical surface of radius R_e:

$$\mathbf{M} = R_e(\cos\beta\cos\alpha, \cos\beta\sin\alpha, \sin\beta) \tag{5.12}$$

Since the Earth rotates around the z axis this angle varies in time: $\alpha = \alpha_0 + \omega_T t$, where ω_T is the Earth's angular velocity. On the ground station a different reference frame is needed, the frame which is natural for an observer on the station. This is determined by the orthonormal vectors:

$$\alpha_1 = \frac{\partial\mathbf{M}}{\partial\alpha} = (-\sin\alpha, \cos\alpha, 0) \tag{5.13}$$

$$\alpha_2 = \frac{\partial\mathbf{M}}{\partial\beta} = (-\sin\beta\cos\alpha, -\sin\beta\sin\alpha, \cos\beta) \tag{5.14}$$

$$\alpha_3 = \frac{\mathbf{M}}{||\mathbf{M}||} = (\cos\beta\cos\alpha, \cos\beta\sin\alpha, \sin\beta) \tag{5.15}$$

Note that, since the position of the ground station varies in time also the three vectors α_i vary in time.

Visibility of the satellite

A satellite is visible from a specific point on Earth's surface only if the angle between the vector $\mathbf{v} = \mathbf{x} - \mathbf{M}$ and the normal to the Earth's surface is between 0 and 90 degrees (see Fig. 5.13). That is:

- $\mathbf{M} \cdot \mathbf{v} \geq 0 \Rightarrow$ visibile
- $\mathbf{M} \cdot \mathbf{v} < 0 \Rightarrow$ not visible

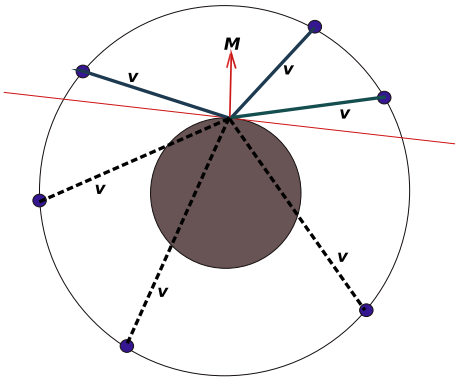

Figure 5.13: Satellite visibility: the satellite is visible from the ground station only if the angle ϕ between $\mathbf{v}$, vector pointing from the ground station to the satellite, and $\mathbf{M}$, normal to the Earth surface in the ground station position, is such that $0 < \phi < \pi/2$

Reflection on the first mirror

We consider a light beam emitted by a source on the satellite that is reflected by a mirror (on the satellite) towards the receiving ground station. We arbitrarily assume that the initial beam direction is tangent to the satellite's orbit, so, its propagation direction is:

$$\mathbf{L}_1 = (-\cos\xi \sin\omega t, \cos\omega t, \sin\xi \sin\omega t) \tag{5.16}$$

To completely describe this light beam we also need the direction of the s-polarization component; it is the normal to the orbital plane:

$$\mathbf{s}_0 = (\sin\xi, 0, \cos\xi) \tag{5.17}$$

This light beam hits the first mirror and, whatever the position $\mathbf{x}$ of the satellite is, it is reflected down the ground station (identified by the vector $\mathbf{M}$). So, the

reflected vector is:

$$\mathbf{L}_2 = \frac{\mathbf{M} - \mathbf{x}}{r} \tag{5.18}$$

where $r = ||\mathbf{M}-\mathbf{x}||$ is the distance between the satellite and the ground station. The angle of incidence of the light beam on the mirror is:

$$\theta_1 = \frac{1}{2}\arccos((-\mathbf{L}_1)\cdot\mathbf{L}_2) \tag{5.19}$$

The Jones matrix describing reflection on the mirror is:

$$\begin{bmatrix} r_p(\lambda,\theta_1) & 0 \\ 0 & r_s(\lambda,\theta_1) \end{bmatrix} \tag{5.20}$$

where $r_p(\lambda,\theta_1)$ and $r_s(\lambda,\theta_1)$ are the reflection coefficients of the mirror.
The reflected light has its on s-polarization direction, which is the normal to the incidence plane. It can be thus calculated by:

$$\mathbf{s}_1 = \frac{\mathbf{L}_1 \times \mathbf{L}_2}{||\mathbf{L}_1 \times \mathbf{L}_2||} \tag{5.21}$$

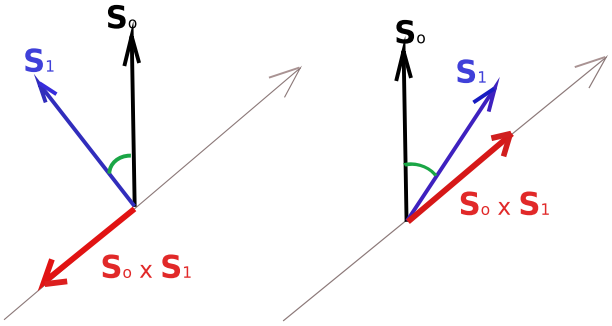

Figure 5.14: Procedure to determine whether the rotation of the s-polarization direction is clockwise or counterclockwise

The polarization of the light emitted by the source and of the light reflected by the first mirror are described in different reference frames, related to each other by a rotation of an angle $\beta_{01} = \arccos(\mathbf{s}_0 \cdot \mathbf{s}_1)$
This formula cannot tell us if the rotation is clockwise or counterclockwise, that is we cannot know from this if the angle β_{01} is positive or negative.
But from Fig. 5.14 we can see that the if $0 \leq \beta_{01} \leq \pi$ the vector $\mathbf{s}_0 \times \mathbf{s}_1$ is opposite to the direction of light propagation $\mathbf{d}$, while if $-\pi \leq \beta_{01} \leq 0$ then the directions of $\mathbf{s}_0 \times \mathbf{s}_1$ and $\mathbf{d}$ coincide. So we can define the quantity:

$$\sigma_{01} = -\frac{\mathbf{s}_0 \times \mathbf{s}_1 \cdot \mathbf{L}_1}{||\mathbf{s}_0 \times \mathbf{s}_1 \cdot \mathbf{L}_1||} \tag{5.22}$$

and we can calculate:

$$\beta_{01} = \sigma_{01} \arccos(\mathbf{s}_0 \cdot \mathbf{s}_1) \tag{5.23}$$

This rotation is then described by the matrix:

$$\begin{bmatrix} \cos\beta_{01} & \sin\beta_{01} \\ -\sin\beta_{01} & \cos\beta_{01} \end{bmatrix} \tag{5.24}$$

Reflection on the second mirror

Using a pointing mirror on the satellite the transmitted light is always sent towards the ground station, where it collected and sent to a polarization analyzer by means of a second pointing mirror.

The polarizer is taken to be horizontal with respect to ground, so its direction will be a linear combination of α_1 and α_2:

$$\mathbf{L}_3 = (\cos\chi)\alpha_1 + (\sin\chi)\alpha_2 \tag{5.25}$$

So the laser beam, coming from the satellite in direction $\mathbf{L}_2$, after reflection on the second mirror, goes in direction $\mathbf{L}_3$. The subsequent analysis is carried on in the same way we made for the first mirror; we calculate the angle of incidence on the mirror θ_2 and then the s-polarization direction as the normal to the second incidence plane:

$$\mathbf{s}_2 = \frac{\mathbf{L}_2 \times \mathbf{L}_3}{||\mathbf{L}_2 \times \mathbf{L}_3||} \tag{5.26}$$

Finally, proceeding as above above, we find the matrix:

$$\begin{bmatrix} \cos\beta_{12} & \sin\beta_{12} \\ -\sin\beta_{12} & \cos\beta_{12} \end{bmatrix} \qquad \beta_{12} = \sigma_{12} \arccos \mathbf{s}_1 \cdot \mathbf{s}_2 \tag{5.27}$$

Then the light must by analyzed by the polarizer, which has its own s-polarization direction, normal to the plane which describes the ground in the station; that is:

$$\mathbf{s}_3 = \frac{\alpha_1 \times \alpha_2}{||\alpha_1 \times \alpha_2||} \tag{5.28}$$

So we need a final rotation of an angle:

$$\beta_{23} = \sigma_{23} \arccos \mathbf{s}_2 \cdot \mathbf{s}_3 \tag{5.29}$$

performed by the matrix:

$$\begin{bmatrix} \cos\beta_{23} & \sin\beta_{23} \\ -\sin\beta_{23} & \cos\beta_{23} \end{bmatrix} \tag{5.30}$$

Total polarization state

The final polarization state is described by:

$$\begin{bmatrix} E'_p \\ E'_s \end{bmatrix} = \begin{bmatrix} \cos\beta_{23} & \sin\beta_{23} \\ -\sin\beta_{23} & \cos\beta_{23} \end{bmatrix} \begin{bmatrix} r_p(\lambda,\theta_2) & 0 \\ 0 & r_s(\lambda,\theta_2) \end{bmatrix} \begin{bmatrix} \cos\beta_{12} & \sin\beta_{12} \\ -\sin\beta_{12} & \cos\beta_{12} \end{bmatrix} \tag{5.31}$$

$$\begin{bmatrix} r_p(\lambda,\theta_1) & 0 \\ 0 & r_s(\lambda,\theta_1) \end{bmatrix} \begin{bmatrix} \cos\beta_{01} & \sin\beta_{01} \\ -\sin\beta_{01} & \cos\beta_{01} \end{bmatrix}$$

From the final polarization state we can find the normalized Jones vector:

$$\frac{1}{\sqrt{|E'_p|^2 + |E'_s|^2}} \begin{bmatrix} E'_p \\ E'_s \end{bmatrix} \tag{5.32}$$

5.3.2 Simulations

Using our model, described in equation (22), we performed simulations for the satellite LAGEOS 2, which has the following parameters:

- inclination = 52.68 degrees
- period = 222.6 minutes
- axes = 5616 Km * 5951 Km
- orbit eccentricity = 0.0135

We considered a latitude of 37 degrees for the ground station, which corresponds to a location in Southern Europe. In our simulations we used aluminum mirrors, whose refractive index, at several wavelengths of interest, is [61] :

- $n(\lambda_1) = 0.129{+}3.25i \quad (\lambda_1 = 532nm)$ $n(\lambda_2) = 0.144{+}5.3i \quad (\lambda_2 = 810nm)$
- $n(\lambda_3) = 0.23{+}7.1i \quad (\lambda_3 = 1064nm)$ $n(\lambda_4) = 0.45{+}9i \quad (\lambda_4 = 1500nm)$

In the case of a mirror made by a simple metallic surface the reflection coefficients are the Fresnel coefficients:

$$r_s(\lambda,\theta_i) = \frac{n_o(\lambda)\cos\theta_i - n(\lambda)\cos\theta_t}{n_o(\lambda)\cos\theta_i + n(\lambda)\cos\theta_t} \qquad r_p(\lambda,\theta_i) = \frac{n_o(\lambda)\cos\theta_t - n(\lambda)\cos\theta_i}{n_o(\lambda)\cos\theta_t + n(\lambda)\cos\theta_i} \tag{5.33}$$

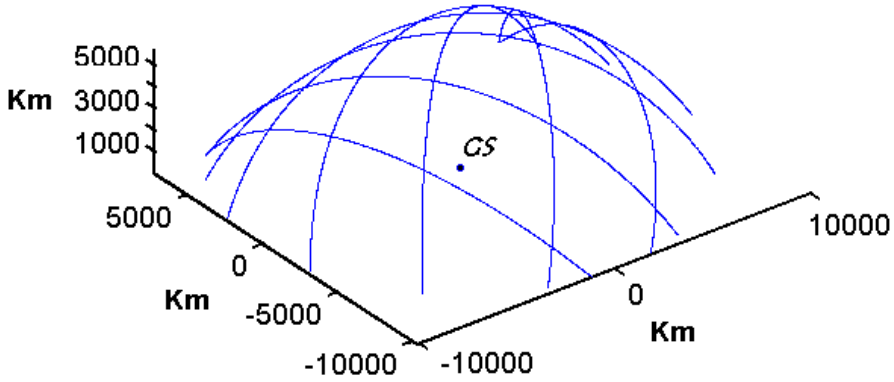

Figure 5.15: Different passages of the satellite above the ground station (represented by the GS in the centre of the XY plane). The satellite comes along different trajectories and so the pointing mirrors must be tilted in order to send the photons to the ground station, whatever the position of the satellite is. This makes the reference frame of the satellite rotate in respect to the reference frame on the ground station, and changes the angle of incidence on the mirrors, resulting on a modification of the polarization states of the emitted photons.

where $n_o(\lambda)$ is the refractive index of air, $n(\lambda)$ is the refractive index of the metal surface of the mirror, θ_i is the incidence angle on the mirror and θ_t is such that: $n_o(\lambda)\sin\theta_i = n(\lambda)\sin\theta_t$.

In Fig. 5.15 the satellite trajectories in the ground station reference frame are presented, it is evident how the satellite comes and goes along different path, with mirrors' angles changing according to the parameters of each single passage. In Fig. 5.16 the Poincaré spheres for two different satellite passages are plotted: the polarization change is evident. Moreover different wavelengths behave in different ways and it is not possible to find a wavelength which minimizes the perturbations. Finally we calculated the Stokes parameters for 300z0 satellite passages at $\lambda = 810$ nm and we plotted them in Fig. 5.17 to have a statistical understanding of polarization changes: we can see that the polarization state can be located almost anywhere on the Poincaré sphere with a higher probability on a strip around the equatorial plane.

Temporal dynamics

It is also interesting to study the temporal dynamics of this effect in order to estimate how fast a possible compensation system should be. As an example in Fig. 5.18 one can see the evolution of the Stokes parameters S_1, S_2 and S_3 during a single satellite passage. Clearly the orbit period for a low-Earth orbit (LEO) satellite, orbiting up to 2000 Km above the ground, will be shorter than

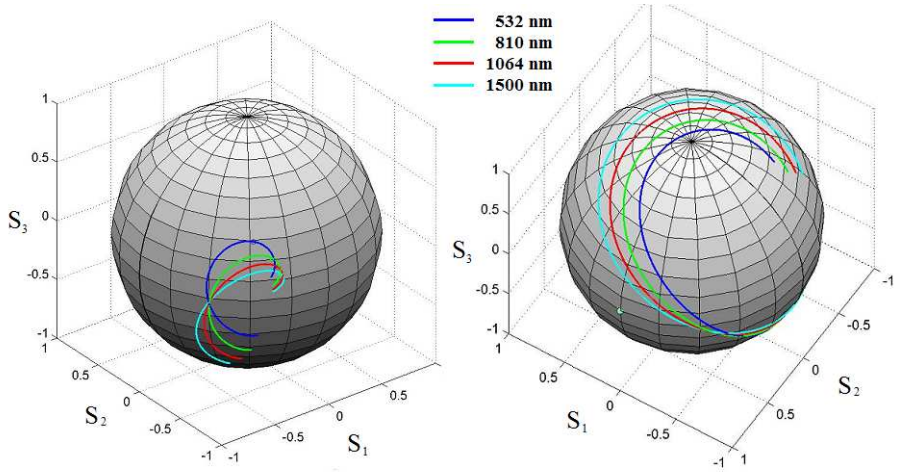

Figure 5.16: Poincaré spheres showing the received polarization states for two different satellite passages on the sky and four different photon wavelengths. The source on the satellite emits a horizontally-polarized photon, whose polarization state, due to rotation of the reference frames determined by the satellite motion and to reflection on mirrors, is in general different from the emitted one and changes in time. Moreover, the polarization states of photons of different wavelengths change in different ways, because of the different responses of mirrors. Elliptical polarization states can be due to complex refractive indices of the mirrors. In particular this result also indicates that it is difficult to use a reference laser at a different wavelength for polarization compensation.

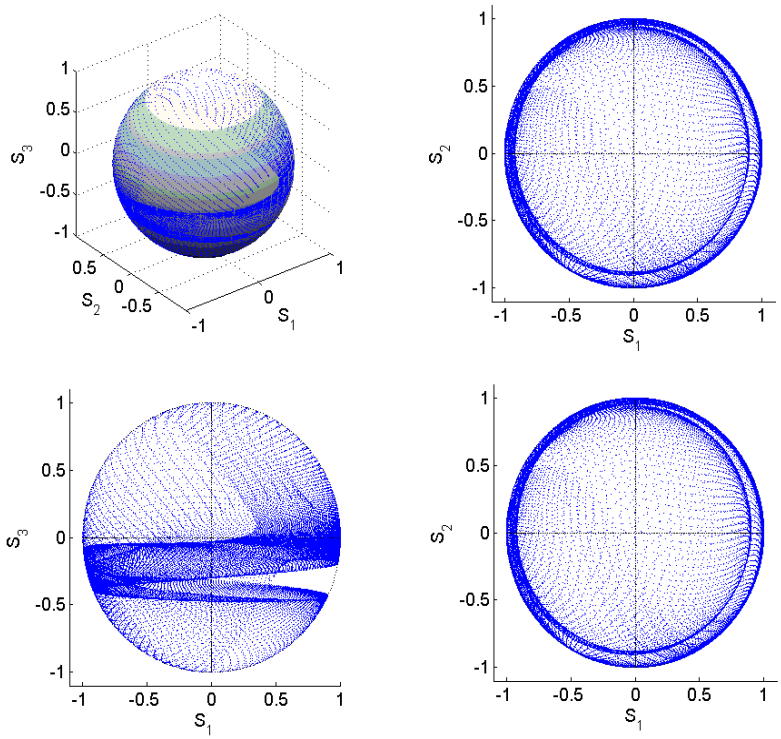

Figure 5.17: Poincaré sphere and its projections on the (S_1, S_2), (S_2, S_3) and (S_1, S_3) planes for 3000 satellite passages on the sky, starting from a horizontally polarized photon emitted by the source on the satellite. Strinkingly, the detected polarization state can be anywhere on the Poicaré sphere, with a higher probability to be on a strip near the equatorial plane.

the one for a medium-Earth orbit (MEO), which travels from 2000 to 35000 Km above ground, due to Kepler laws. Therefore the temporal evolution of the Stokes parameters will be much faster.

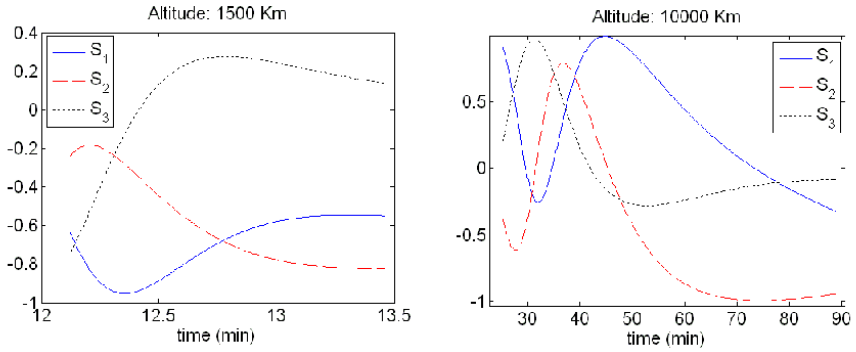

Figure 5.18: Temporal evolution of the Stokes parameters at the Earth-based receiver, for a verticaly-polarized state emitted by the source on the satellite. The dynamics is faster for a LEO satellite (1500 Km) passage than it is for a MEO one (10000 Km).

To have a better statistical understanding of the effect we considered the time derivative of the Stokes parameter S_1 for 100 satellite passages. From Fig. 5.19 we can see that:

$$|\frac{dS}{dt}| < 0.03 \quad (d = 500Km) \qquad |\frac{dS}{dt}| < 0.002 \quad (d = 10000Km)$$

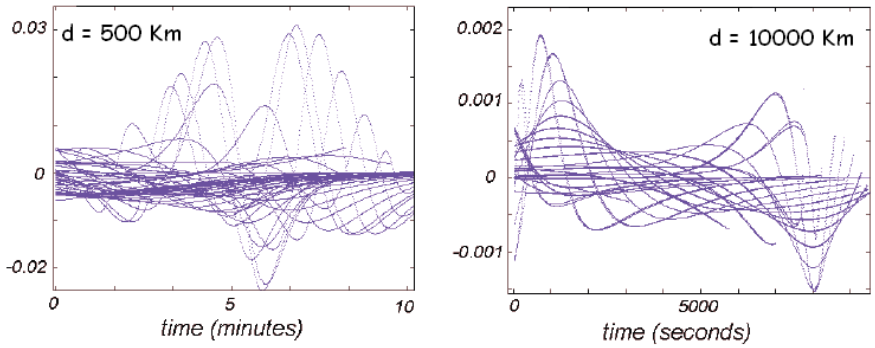

Figure 5.19: Temporal dynamics of the Stokes parameter S_1 for vertically-polarized photons emitted by a LEO (500 Km) and MEO (10000 Km) satellite. The maximum value for dS_1/dt is 0.03 for the LEO case and 0.002 for the MEO case, showing that the more distant the satellite is the slower polarization transformations are.

Clearly LEO satellites provide lower channel losses, making it easier to establish a single photon link, but on the other hand move faster in the sky,

imposing the availability of a good tracking and pointing system and exhibit faster temporal variations of the photon polarization states to compensate for.

5.3.3 Other effects

Even though realistic optical systems for satellite quantum communication could be more complex than our simple two-mirror model, most proposed schemes are based on a fixed telescope and a movable steering mirror for fine pointing at each communication side. Since the effect of fixed mirrors is just to provide a constant offset, they will just introduce time-independent modifications which can be compensated by proper calibration.
Besides instrumental contributions, also the atmosphere could introduce perturbations on the polarization of an electromagnetic wave, due to turbulence, scattering processes or Faraday effect. According to theoretical models and experimental data [62, 63], turbulence could give a rotation of the order of 10^{-11} rad/Km, while scattering could contribute with a rotation of about 10^{-4} rad/Km; both are much smaller than the what we have found in our simulations for the tracking system. A simple calculation shows that also Faraday effect is neglectable. Assuming for the magnetic field B its maximum value at the Earth surface ($B = 60\mu T$), for the atmosphere depth a value of $d = 10$ Km and for the Verdet constant of air the value [64] $V = 6.83 * 10^{-6} min/(Gcm) = 1.9 * 10^{-3} rad/(T * m)$ we find that the plane of polarization undergoes a rotation of an angle:

$$\chi = VBd = 0.001 rad \tag{5.34}$$

This value, which can be considered as a higher bound since we assumed the geomagnetic field constant at its value at the Earth's surface (while it decreases with r^{-3} moving away into the atmosphere) is clearly unimportant.

5.3.4 Compensation schemes

From our analysis, it is evident that the moving mirrors of the satellite's and ground station's pointing system are the most important source of perturbation in a quantum communication link between Space and Earth, introducing a significant time-dependent rotation of the polarization states of the signal photons. This result shows that it is necessary to use an active compensation system, since for quantum communication all the polarization states must be transmitted and received correctly.

Deterministic open-loop control

A first approach is to deterministically calculate the actual polarization rotation in real time, given the satellite trajectory and the pointing angles are known, and accordingly vary the polarization compensation rotation at the ground station as the satellite passes by. However, this approach requires that all the relevant parameters of all the mirrors to be precisely known, stable against physical influences such as temperature fluctuations, and with a long-term stability.

Geostationary satellites

A second solution would be the use of geostationary satellite, which would remain fixed in the sky with respect to the ground station. Therefore there would be no need for the pointing and tracking system, and there would be no time-dependent polarization transformation imposed on the photons. But, on the other hand geostationary orbit is more than 35000 Km apart, making the establishment of a single photon link extremely unpractical.

Reference beam at a different wavelength

A possible implementation of a compensation system could be by means of a probe laser beam whose wavelength (λ_P) is different from the one of the signal photons (λ_s). The dispersive channel would act on the photon with the transformation $U(\lambda)$. In the ground station one could perform a polarization analysis of the reference beam and retrieve the transformation $U(\lambda_P)$ that has been performed on it, and then he could apply the inverse transformation on the received signal photons' polarization states, which have undergone the transformation $U(\lambda_s)$. The problem is that, in general the channel is dispersive meaning that $U(\lambda_s) \neq U(\lambda_P)$ making the compensation imperfect. In Table 1 one can see the results of the simulations for a MEO satellite with signal photons at 800 nm and probe beam at 825 nm: the result is not bad, even though an error of about 1% still remains in S_3.

Time-multiplexing of signal and compensation beams

Another possible approach could be to use the same wavelength for signal and reference photons, but alternating the times in which they are emitted, so as to implement a time-multiplexing configuration. This scheme, provided that the transmission and analysis of the reference beam is repeated at a sufficiently high rate required to keep up with the temporal variations of the polarization properties, will allow near compensation at every chosen degree.

Particularly, supposing that the interval Δt between two successive compensation pulses is short, the maximum error in the Stokes parameters can be expressed as:

$$\Delta S_{max} \simeq \left(\frac{dS}{dt}\right)_{max} \Delta t \tag{5.35}$$

Supposing to know the maximum temporal variation of the Stokes parameters, setting the chosen maximum error rate ΔS_{max} one can find the maximum . From this the minimum repetion rate of the probe pulses can be calculated:

$$f_{rep} = \frac{1}{\Delta t} = \frac{1}{\Delta S_{max}} \left(\frac{\partial S}{\partial t}\right) \tag{5.36}$$

In the case of a LEO satellite we have predicted the maximum temporal variation of the Stokes parameters to be around $0.03 s^{-1}$: this gives $f_{rep} = 3KHz$ to achieve $\Delta S_{max} < 10^{-5}$.

5.4 Conclusions

In this Chapter we addressed the problem of the distribution of polarization-encoded single and entangled photons in Space-to-Earth optical links. This issue is important in order to realize global-scale quantum key distribution, and it is a necessary prerequisite for any quantum physics experiment in Space.
In particular, we demonstrated experimentally the feasibility of single photon exchange between a LEO satellite and an optical ground station. Our experiment is particularly significant since it shows that the signals photons can be identified against a strong background noise despite the technical difficulties associated with the fast satellite motion. The next step would be to establish a real quantum link, implementing quantum communication protocols. However this cannot be done with our configuration, since:

- the signal-to-noise ratio in our experiment $(2:1)$is not sufficient to violate Bell inequalities. A $6:1$ ratio would be needed (see [65]), but it cannot be reached in our simualted configuration sice the losses are too strong, mainly due to the small size of the cornercubes.

- our channel is not polarization-preserving, preventing the possibility of implementing quantum information protocols with polarization-encoded qubits

Only a dedicated hardware, optimizing the transmission efficiency and guaranteeing the preservation of polarization states in the channel would enable the successful implementation of a quantum channel between Space and the

Earth.
Moreover we studied quantitatively the transmission of polarization states in a Satellite-to-Earth channel, identifying the satellite pointing and tracking system as the major problem. We suggested and discussed different compensation schemes for the problem.

The contribution of the PhD candidate to the topics presented in this Chapter is the following:

- construction and characterization of the receiver optics
- partecipation to the experimental sessions at MLRO. The author collaborated to the construction of the optical setup and to data collection
- data analysis
- modelling and simulation of the polarization properties of a Satellite-to-Earth quantum channel

Chapter 6

Conclusions and perspectives

This thesis presents the research work conducted by the PhD candidate from January 2005 to December 2007 in the Department of Information Engineering of Padova University and in the Quantum Imaging Lab (Boston University) under the supervision of Prof. Paolo Villoresi (cosupervisor Prof. Alexander Sergienko, Boston University). The work was financed by the Fondazione Cassa di Risparmio di Padova e Rovigo via the scholarship *Ottica per la Comunicazione Quantistica*.
The main research theme was the generation, manipulation and application of multiparameter entangled states, particularly: the manipulation of multiparameter entangled states by means of adaptive optics, the characterization and application of frequency-anticorrelated states to dispersion and spectral polarization measurement, and satellite quantum communication.

Manipulation of multiparameter entangled states with adaptive optics

In the field of quantum optics, the most important technique to generate entangled photons is spontaneous parametric downconversion, a second-order nonlinear optical process where a pump photon is split in two other photons. Energy and momentum conservation induce correlations between the two photons, making them cuncurrently entangled in wave-vector, frequency and polarization.
In our work we engineered the spatial component by means of an optical setup comprising an adaptive mirror, to study the effects on spectral and polarization quantum interference. The results of our theoretical and experimental activities were:

- a quantitative model for multiparameter entanglement in type-II down-

conversion

- in type-II quantum interferometry, incresing the collection angular acceptance (to increase intensity and bandwidth) the interference pattern visibility decreases due to spatial walk-off. We demonstrated the possibility to restore high visibility even with large detection apertures.

- a spatial counterpart of spectral dispersion cancellation was suggested and described with numerical simulations.

The results are presented in Chapter 2 of the present document.

Research on this topic has been conducted at Quantum Imaging Laboratory, Boston University (prof. A. V. Sergienko). All the work (experiment design, analytical and numerical modelling, construction of the experimental setup and data analysis) was performed by the PhD candidate. A theoretical paper is being prepared, aimed for submission to *Physical Review A*.

Future work along this research line will regard the experimental demonstration of spatial even-order phase cancellation and its application in the field of quantum optical coherence tomography.

Characterization and application of frequency-anticorrelated states to dispersion and spectral polarization measurement

White-light interferometry is one of the most widespread techniques to measure chromatic dispersion: by means of a Michelson interferometer feeded with broadband light one can retrieve the spectral phase acquired propagating through the material. The larger the optical bandwidth, the higher the measurement accuracy; on the other hand dispersion, the very same effect we want to characterize, in the case of broad bandwidth broadens the interference pattern reducing the signal-to-noise ratio.
By means of numerical simulations we showed that if the signal to noise ratio is reduced beyond a certain level, the phase-retrieval algorithm starts to lose accuracy, giving measurement errors. Using the spectral dispersion cancellation effect we can reduce the interference pattern broadening, keeping the signal-to-noise ratio higher. This allows to extend the optical bandwidth, gaining more and more accuracy in the measurement of the odd-order dispersion coefficients. The price to pay is, however, that only the odd-order coefficents can be retrieved.

Besides chromatic dispersion, the same approach can be used to measure spectral porization. To do this, we developed a generalized approach providing tools for a detailed characterization of a quantum-optical state that is entangled both in spectrum and in polarization. We accomplished this by generalizing the classical definition of the spectral coherence matrix in order to introduce the two-photon coherence matrix for a broadband two-photon entangled state. We then outlined the experimental procedure for the measurement of its elements and illustrated how it can be used to quantify properties of frequency-polarization entangled states. Moreover, we discussed that such a technique can be used to characterize properties of devices and materials through which such a two-photon entangled state has propagated. We believe that the increased system dimensionality in the quantum case will find applications for optical measurement techniques, particularly in the field of quantum ellipsometry.

Research in this topics has been conducted at Quantum Imaging Laboratory, Boston University (prof. A. V. Sergienko) and is described in Chapters 3 and 4. All the theoretical and numerical analysis was performed by the PhD candidate.

A manuscript about the spectral two-photon coherence matrix is in press:

C. Bonato, P. Villoresi and A. V. Sergienko, "Two-photon spectral coherence matrix and characterization of multiparameter entangled states", *Physics Letters A* (2008), 10.1016/j.physleta.2008.01.016

A manuscript about dispersion measurements using broadband frequency-anticorrelated light is being prepared, aimed for submission to *Optics Express*. The same material has been presented at the following conferences:

- **C. Bonato**, A. V. Sergienko, B. E. A. Saleh, M. C. Teich, "Two-photon spectral coherence matrix and multiparameter optical entanglement", poster presentation, CLEO/QELS 2007, Baltimore, USA (May 2007)

- **C. Bonato**, A. V. Sergienko, B. E. A. Saleh, M. C. Teich, "Two-photon spectral coherence matrix and multiparameter optical entanglement", poster presentaion, CLEO Europe 2007, Munich (June 2007)

- **C. Bonato**, A. V. Sergienko, P. Villoresi, "Dispersion measuremnt using

frequency-anticorrelated light", oral presentation, CLEO Europe 2007, Munich (June 2007)

Satellite quantum communication

Entanglement is a valuable resource for quantum information processing, for example in quantum cryptography. Optical quantum cryptography links have been successfully implemented, which allow to share secure keys between parties distant more than 100 Km. However, only using space technology one could realize global-scale quantum key distribution.
The experimental acivities carried on in this thesis brought, for the first time, to the experimental verification of single-photon exchange between a LEO satellite and a ground station. The retroreflection of a weak laser pulse from a geodetic satellite was exploited to simulate a single-photon source onboard a satellite. The emitted photons were detected by the 1.5 m telescope set in Matera Laser Ranging Observatory and distinguished from the strong noise background by means of careful temporal, psatial and spectral filtering. Data analysis showed the detection of signal photon with a 5 cps rate.

Finally we studied numerically the polarization properties of a space-to-Earth quantum channel showing that a time-dependent polarization transformation is induced on qubits due to the relative motion between the satellite and the ground station. Compensation techniques for this effect were suggested and discussed.

Research on this topic, presented in Chapter 5, has been conducted in collaboration with the group of prof. A. Zeilinger, Institut fur Experimentalphysik, Vienna. The PhD candidate's contribution to the topics presented in this Chapter is the following:

- construction and characterization of the receiver optics
- partecipation to the experimental sessions at MLRO, in particular as regards the construction of the optical setup and data collection
- data analysis
- modelling and simulation of the polarization properties of a Satellite-to-Earth quantum channel

A manuscript has been prepared about the QSpace experiment and submitted to *New Journal of Physics*. The pre-print is available on the ArXiv:

P. Villoresi, T. Jennewein, F. Tamburini, M. Aspelemyer, **C. Bonato**, R. Ursin, C. Pernechele, V. Luceri, G. Bianco, A. Zeilinger, C. Barbieri, "Experimental verification of the feasibility of a quantum channel between Space and Earth"

The material about the polarization transformations induced by reflective optical devices has been published in the following papers:

- **C. Bonato**, M. Aspelmeyer, T. Jennewein, C. Pernechele, P. Villoresi, A. Zeilinger, "Influence of satellite motion on polarization qubits in a Space-Earth quantum communication link", *Optics Express*, **14**, 10050-10059 (2006)
- **C. Bonato**, C. Pernechele, P. Villoresi, "Influence of all-reflective optical systems in the transmission of polarization-encoded qubits", *Journal of Optics A: Pure and Applied Optics*, **9**, 899-906 (2007)

Bibliography

[1] A. Einstein, B. Podolsky, and N. Rosen. Can quantum-mechanical description of physical reality be considered complete? *Phys. Rev.*, 47:777–780, 1935.

[2] J. S. Bell. On einstein-podolski-rosen paradox. *Physics*, 1:195–200, 1964.

[3] J. F. Clauser, M. A. Horne, A. Shimony, and R. A. Holt. Proposed experiment to test local hidden-variable theories. *Phys. Rev. Lett.*, 23:880–884, 1969.

[4] A. Aspect, P. Grangier, and G. Roger. Experimental realization of einstein-podolsky-rosen-bohm gedankenexperiment: A new violation of bell's inequalities. *Phys. Rev. Lett.*, 49:91–94, 1982.

[5] D. N. Klyshko. *JETP Letters*, 6:23, 1967.

[6] S. E. Harris, M. K. Osham, and R. L. Byer. Observation of tunable optical parametric fluorescence. *Phys. Rev. Lett.*, 18:732–734, 1967.

[7] D. Magde and H. Mahr. Study in ammonium dihydrogenum phospate of spontaneous parametric interactions tunable from 400 to 16000 a. *Phys. Rev. Lett.*, 18:905, 1967.

[8] D. A. Kleinmann. Theory of optical parametric noise. *Phys. Rev.*, 174:1027–1041, 1968.

[9] T. G. Giallorenzi and C. L. Tang. Quantum theory of spontaneous parametric scattering of intense light. *Phys. Rev.*, 166:225–233, 1968.

[10] D. C. Burnham and D. L. Weinberg. Observation of simultaneity in parametric production of optical photon pairs. *Phys. Rev. Lett.*, 25:84, 1970.

[11] C. K. Hong and L. Mandel. Theory of parametric frequency downconversion of light. *Phys. Rev. A*, 31:2409, 1985.

[12] C. K. Hong, Z. Y. Ou, and L. Mandel. Measurement of subpicosecond time interval between two photons by interference. *Phys. Rev. Lett.*, 59:2044, 1987.

[13] Morton H. Rubin. Transverse correlations in optical spontaneous parametric down-conversion. *Phys. Rev. A*, 54:5349, 1996.

[14] J. D. Franson. Nonlocal cancellation of dispersion. *Phys. Rev. A*, 45:3126–3132, 1995.

[15] A. M. Steinberg, P. G. Kwiat, and R. Y. Chiao. Dispersion cancellation and high-resolution time measurements in a fourth-order optical interferometer. *Phys. Rev. A*, 45:6659, 1992.

[16] M. Atature, G. Di Giuseppe, M. Shaw, A. V. Sergienko, B. E. A. Saleh, and M. C. Teich. Multiparameter entanglement in quantum interferometry. *Phys. Rev. A*, 66:023822, 2002.

[17] D. James, P. G. Kwiat, W. J. Munro, and A. G. White. Measurement of qubits. *PRA*, 64:052312, 2001.

[18] A. Abouraddy, A. V. Sergienko, B. E. A. Saleh, and M. C. Teich. Quantum entanglement and the two-photon stokes parameters. *OC*, 201:93–98, 2002.

[19] A. Abouraddy, K. Toussaint, A. V. Sergienko, B. E. A. Saleh, and M. C. Teich. Ellipsometric measurements by use of photon pairs generated by spontaneous parametric down conversion. *Optics Letters*, 26:1717–1719, 2001.

[20] A. Abouraddy, K. Toussaint, A. V. Sergienko, B. E. A. Saleh, and M. C. Teich. Quantum ellipsometry. *J. Opt. Soc. Am. B*, 19:652–656, 2002.

[21] K. Toussaint, G. di Giuseppe, K. J. Bycenski, A. V. Sergienko, B. E. A. Saleh, and M. C. Teich. Quantum ellipsometry using correlated-photon beams. *PRA*, 70:023801, 2004.

[22] D. J. L. Graham, A. S. Parkins, and L. R. Watkins. Ellipsometry with polarisation-entangled photons. *Opt. Express*, 14:7037–7045, 2006.

[23] R. Barakat. Theory of the coherency matrix for light of arbitrary spectral bandwidth. *JOSA*, 53(3):317, 1963.

[24] Leonard Mandel and Emil Wolf. *Optical Coherence and Quantum Optics*. Cambridge University Press, September 1995.

[25] Jan Perina. *Coherence of Light*. Van Nostrand Reinhold Company, 1971.

[26] N. Wiener. *J. Franklin Inst.*, 57:218, 1925.

[27] N. Wiener. *Acta Math.*, 55:117, 1930.

[28] E. Wigner. *Phys. Rev.*, 40:749, 1932.

[29] M. H. Tai and M. Harvit. Fourier and hadamard transform spectrometers: a limited comparison. *AO*, 15:2664, 1976.

[30] W. Wasilewski, P. Wasylczyk, P. Kolenderski, K. Banaszek, and C. Radzewicz. Joint spectrum of photon pairs measured by coincidence fourier spectroscopy. *OL*, 31:1130–1132, 2006.

[31] T. Brixner, G. Krampert, T. Pfeifer, R. Selle, G. Gerber, M. Wollenhaupt, O. Graefe, C. Horn, D. Liese, and T. Baumert. Qauntum control by ultrafast polarization shaping. *Phys. Rev. Lett.*, 92:208301, 2004.

[32] Y. Silberberg. Quantum control with a twist. *Nature*, 430:20, 2004.

[33] L. Polacheck, D. Oron, and Y. Silberberg. Full control of the spectral polarization of ultrashort pulses. *Opt. Lett.*, 631:31, 2006.

[34] B. Dayan, A. Peer, A. Friesem, and Y. Silberberg. Two-photon absorption and coherent control with broadband downconverted light. *PRL*, 93:023005, 2004.

[35] A. G. Van Engen, S. A. Diddams, and T. S. Clement. Dispersion measurements of water with white-light interferometry. *Appl. Opt.*, 37:5679–5686, 1999.

[36] I. Thomann, L. Hollberg, S. A. Diddams, and R. Equallk. Chromium-doped forsterite: Dispersion measurement with white-light interferometry. *Appl. Opt.*, 42:1661–1666, 2003.

[37] M. Galli, D. Bajoni, F. Marabelli, L. C. Andreani, L. Pavesi, and G. Pucker. Photonic bands and group-velocity dispersion in Si/SiO_2 photonic crystlas from white-light interferometry. *Phys. Rev. B*, 69:115107, 2004.

[38] W. H. Knox. Dispersion measurements for femtosecond-pulse generation and applications. *Appl. Phys. B*, 58:225–235, 2005.

[39] L. G. Cohen. Comparison of single-mode fiber dispersion measurement techniques. *J. Lightwave Technol.*, 3:958–966, 1985.

[40] J. Y. Lee and D. Y. Kim. Versatile chromatic dispersion measurement of a single mode fiber using spectral white light interferometry. *Opt. Express*, 14:11608–11615, 2006.

[41] K. Naganuma, K. Mogi, and H. Yamada. Group-delay measurement using the fourier transform of an interferometric cross correlation generated by white light. *Opt. Lett.*, 15:393–395, 1990.

[42] M. Beck and I. Walmsley. Measurement of group delay with high temporal and spectral resolution. *Opt. Lett.*, 15:492–494, 1990.

[43] S. Diddams and J. C. Diels. Dispersion measurements with white-light interferometry. *J. Opt. Soc. Am.*, 13:1120–1129, 1996.

[44] C. Dorrer and F. Salin. Characterization of spectral phase modulation by classical and polarization spectral interferometry. *J. Opt. Soc. Am.*, 15:2331–2337, 1998.

[45] A. Gostev, M. Heiml, R. Paschotta, and U. Keller. Noise-related resolution of dispersion measurements with white-light interferometers. *J. Opt. Soc. Am. B*, 22:1868–1874, 2005.

[46] A. M. Steinberg, P. G. Kwiat, and R. Y. Chiao. Dispersion cancellation in a measurement of the single-photon propagation velocity in glass. *Phys. Rev. Lett.*, 68:2421, 1992.

[47] A. Abouraddy, M. B. Nasr, B. E. A. Saleh, A. V. Sergienko, and M. C. Teich. Quantum optical coherence tomography with dispersion cancellation. *Phys. Rev. A*, 65:053817, 2002.

[48] M. B. Nasr, B. E. A. Saleh, A. V. Sergienko, and M. C. Teich. Demonstration of dispersion-cancelled quantum optical coherence tomography. *Phys. Rev. Lett.*, 91:083601, 2003.

[49] K. J. Resch, P. Puvanathasan, J. S. Lunden, M. W. Mitchell, and K. Bizheva. Classical dispersion-cancellation interferometry. *Opt. Expr.*, 15:8797–8804, 2007.

[50] K. Schmid, H. Becker, W. Dultz, W. Martienssen, M. Kempe, and H. Schmitzer. Interferometric optical path measurement of a glass wedge with single photons and biphotons. *Opt. Lett.*, 3:2257–2259, 2007.

[51] W. K. Wooters nd W. H. Zurek. A single quantum cannot be cloned. *Nature*, 299:802–803, 1982.

[52] W. T. Buttler, R. J. Hughes, P. G. Kwiat, S. K. Lamoreaux, C. G. Peterson, and C. M. Simmons. Practical free-space quantum key distribution over 1 km. *Phys. Rev. Lett.*, 81:3283–3286, 1998.

[53] R. J. Hughes, J. E. Nordholt, D. Derkacs, and J. C. Peterson. Practical free-space quantum key distribution over 10 km in day-light and at night. *New J. Phys.*, 4:43.1–43.14, 2002.

[54] C. Kurtsiefer, P. Zarda, M. Holder, H. Weinfurter, P. Gormar, P. R. Tapster, and J. G. Rarity. A step towards global quantum key distribution. *Nature*, 419:450, 2002.

[55] M. Aspelmeyer et al. Long distance free-space distribution of quantum entanglement. *Science*, 301:621, 2003.

[56] Cheng-Zhi Peng, Tao Yang, Xiao-Hui Bao, Jun-Zhang, Xian-Min Jin, Fa-Jong Feng, Bin Yang, Jian Yang, Juan Yin, Qian Zhang, Nan Li, Bao-Li Tian, and Jian-Wei Pan. Experimental free-space distribution of entangled photon pairs over 13 km: towards satellite-based global quantum communication. *Phys. Rev. Lett.*, 94:150501, 2005.

[57] L. J. Nugent and R. J. Condon. Velocity aberration and atmospheric refraction in satellite laser communication. *Appl. Opt.*, 5:1832, 1966.

[58] W. F. Eddy, J. J. McCarthy, D. E. Pavlis, J. A. Marshall, S. B. Luthce, and L. S. Tsaoussi, editors. *GEODYN II System Operations Manual, vol. 1-5.* ST System Corp., Lanham MD, USA, 1990.

[59] J. G. Rarity, P.R. Tapster, P. M. Gorman, and P. Knight. Ground to satellite secure key exchange using quantum cryptography. *New J. Phys.*, 4:82, 2002.

[60] A. Sehatet al. Quantum polarization properties of two-mode energy eigenstates. *Phys. Rev. A*, 71:033818, 2004.

[61] E. D. Palik, editor. *Handbook of optical constants of solids.* San Diego: academic Press, 1998.

[62] D. H. Hoehn. Depolarization of a laser beam at 6328 a due to atmospheric transmission. *Appl. Opt.*, 8:367, 1968.

[63] S. Jorna. Atmospheric depolarization and stimulated brillouin scattering. *Appl. Opt.*, 10:2661, 1971.

[64] W. E. Forsythe, editor. *Smithsonian Physical Tables.* Knovel, 1998.

[65] M. Aspelmeyer, T. Jennewein, M. Pfennigbauer, W. R. Leeb, and A. Zeilinger. Long distance quantum communication with entangled photons using satellites. *IEEE J. Sel. Top. Quantum Electron.*, 9:1541, 2003.